

University of Southampton Research Repository ePrints Soton

Copyright © and Moral Rights for this thesis are retained by the author and/or other copyright owners. A copy can be downloaded for personal non-commercial research or study, without prior permission or charge. This thesis cannot be reproduced or quoted extensively from without first obtaining permission in writing from the copyright holder/s. The content must not be changed in any way or sold commercially in any format or medium without the formal permission of the copyright holders.

When referring to this work, full bibliographic details including the author, title, awarding institution and date of the thesis must be given e.g.

AUTHOR (year of submission) "Full thesis title", University of Southampton, name of the University School or Department, PhD Thesis, pagination

UNIVERSITY OF SOUTHAMPTON

FACULTY OF NATURAL AND ENVIRONMENTAL SCIENCES

School of Chemistry

Metal nitrides as negative electrode materials for sodium-ion batteries

by

Xianji Li

Thesis for the degree of Doctor of Philosophy

February 2015

UNIVERSITY OF SOUTHANPTON

ABSTRACT

FACULTY OF NATURAL AND ENVIRONMENTAL SCIENCES

DEPARTMENT OF CHEMISTRY

Doctor of Philosophy

METAL NITRIDES AS NEGATIVE ELECTRODE MATERIALS FOR
SODIUM-ION BATTERIES

By Xianji Li

Sodium-ion batteries undergone a rapid development in recent years and have great potential to be a strong alternative to lithium-ion batteries for renewable energy storage. Taking inspiration from lithium-ion batteries, the electrode materials selection and charge storage mechanism in sodium-ion cells are developed. Metal nitrides have been reported to be suitable as negative electrode materials for lithium-ion batteries based on the conversion reaction mechanism.

In this work, the suitability of several metal nitrides, e.g. Ni_3N , Cu_3N or Sn_3N_4 as negative electrode materials for sodium-ion batteries was investigated. Metal nitrides were synthesized from ammonolysis of specific precursors at targeted temperatures. As-synthesized metal nitrides were characterized by several techniques, such as PXD,

TEM, or IR. Their electrochemical performance was evaluated in sodium half-cells and lithium half-cells via cyclic voltammetry or galvanostatic tests.

In sodium-ion half-cells, Ni₃N was firstly studied as the negative electrode material and it exhibited a capacity of around 460 mA h g⁻¹ at 0.5 C in the first reduction cycle and a reversible capacity of 134 mA h g⁻¹ after 20 cycles, which was competitive to the most carbon based materials by then.

Cu₃N showed 89 mA h g⁻¹ observed in the 50th cycle at 0.1 C, which exhibited a better cycling stability than that of Ni₃N in sodium-ion half-cells. *Ex situ* XRD showed the formation of metallic copper in the first cycle but the reflections of metallic copper did not vanish after re-oxidizing to 3 V, which indicates that the conversion reaction from Cu₃N to Cu is not a completely reversible process.

Bulk tin nitride was synthesized from ammonolysis of polymeric amide-derived precursor which derived from the reaction of Sn(NEt₂)₄ with ammonia. After washing with 3M HCl, pure phase Sn₃N₄ was obtained. Samples obtained at 350 °C were observed to exhibit small particle size with the highest specific surface area among all samples.

The cell with alginate binder had a capacity of 175 mA h g⁻¹ in the 2nd cycle and 155 mA h g⁻¹ in the 50th cycle (89% capacity retention) at 200 mA g⁻¹ while the one with CMC binder showed a capacity of 144 mA h g⁻¹ in the 2nd cycle and 113 mA h g⁻¹ in the 50th cycle (79% capacity retention) at the same current rate. The effect of FEC additives was also investigated in this work. With the help of FEC additives, Sn₃N₄ cells with alginate binder showed a capacity of 680 mA h g⁻¹ in the first cycle at 50 mA g⁻¹ in the sodium-ion cells with the FEC additive and approximately 47% of which (320 mA h g⁻¹) was retained in the second cycle and the stable cycle performance around 85% capacity (compared

with the second cycle) retention over 50 cycles. A significant capacity rise ($\sim 35\%$) against the cell without FEC additives was observed. The electrochemical behaviour of Sn_3N_4 is the best electrochemical performance of transition metal nitrides as negative electrode materials in Na-ion cells and it can be comparable with other negative electrode materials in sodium cells. Bulk tin nitride was firstly investigated as negative electrode materials in Li-ion batteries, with the aid of FEC additives, it showed a capacity of 370 mA h g^{-1} capacity over 50 cycles at 200 mA h g^{-1} . The *ex situ* XRD measurements showed a hybrid charge mechanism combining conversion reaction with alloy/de-alloy process. Screening the electrochemistry of other transition metal nitrides, e.g. chromium nitride, molybdenum nitride, or manganese nitride in battery applications was conducted. It is noted that molybdenum nitride and manganese nitride showed decent specific capacity and cycle stability in sodium cells. Manganese nitride showed a high specific capacity of 127 mA h g^{-1} at 50 mA g^{-1} over 50 cycles, which is comparable to other transition metal nitrides, e.g. nickel nitride and copper nitride. In lithium half-cells, it exhibited a 600 mA h g^{-1} reversible capacity at 200 mA g^{-1} and retained 340 mA h g^{-1} capacity in the 50th cycle.

DECLARATION OF AUTHORSHIP

I,XIANJI LI....., [please print name] declare that the thesis entitled ‘Metal nitrides as negative electrode materials in sodium-ion batteries’ and the work presented in the thesis are both my own, and have been generated by me as the result of my own original research. I confirm that:

- this work was done wholly or mainly while in candidature for a research degree at this University;
- where any part of this thesis has previously been submitted for a degree or any other qualification at this University or any other institution, this has been clearly stated;
- where I have consulted the published work of others, this is always clearly attributed;
- where I have quoted from the work of others, the source is always given. With the exception of such quotations, this thesis is entirely my own work;
- I have acknowledged all main sources of help;
- where the thesis is based on work done by myself jointly with others, I have made clear exactly what was done by others and what I have contributed myself;
- parts of this work have been published as:

1. Performance of nanocrystalline Ni₃N as a negative electrode for sodium-ion batteries.

Xianji Li, Mahboba M. Hasan, Andrew L. Hector and John R. Owen. *J. Mater. Chem. A*, 2013, 1, 6441-6444. DOI: 10.1039/C3TA00184A

2. Evaluation of Cu₃N and CuO as negative electrode materials for sodium batteries.

Xianji Li, Andrew L. Hector, and John R. Owen. *Journal of Physical Chemistry C*, 2014, 118 (51), 29568–29573 (DOI: 10.1021/jp509385w)

3. Solvothermal synthesis and electrochemical charge storage assessment of Mn₃N₂.

S. Imran U. Shah, Andrew L. Hector, Xianji Li and John R. Owen. *Journal of Materials Chemistry A*, 2015,3, 3612 (DOI: 10.1039/C4TA05316H) .

Signed:

Date:.....

ACKNOWLEDGEMENTS

Firstly, I would like to thank my supervisor Dr Andrew L. Hector for his great support, advice and patience throughout my PhD study. I also would like to thank my co-supervisor Prof John R. Owen for his helpful discussions in my project. And thanks to other members of the group, Imran for his help and useful discussions about synthesis and characterizations, Mahboba, Wafa, Calum, Ben, Jack and Kripa. I would like to thank people from Owen group, Mike and Jake for the discussions about electrochemistry.

I would like to thank the financial help from the University of Southampton to support my living expenditures and the use of EPRC funded National Chemical Database Service hosted by the Royal Society of Chemistry.

I would like to specially thank my parents. Without their limitless supports, mentally and financially, I cannot make it today. Even far away from them, their loves make me never feel lonely and helpless. I would like to thank my new family member, my fiancée, Xing Mu, for her love and supports during my PhD thesis writing.

I would like to thank all my friends in the world, old and new. It is you that make my life colourful.

ABBREVIATIONS

BC	Butylene carbonate
BET	Brunauer-Emmett-Teller
BPOE	Bipolar porous organic electrode
CCD	Charge-coupled device
CNTs	Carbon nanotubes
CMC	Sodium carboxymethyl cellulose
CV	Cyclic voltammetry
DEC	Diethyl carbonate
DMC	Dimethyl carbonate
EC	Ethylene carbonate
EDA	Ethylenediamine
EDLC	Electrochemical double-layer capacitors
EVA	Diffract Evaluation program
FEC	Fluorinated ethylene carbonate
GSAS	General Structure Analysis Suite
HCNW	Hollow carbon nanowires
IR	Infrared spectroscopy
LEDs	light-emitting diodes
NASICON	NAtrium Super Ion CONductor
PB	Parallel beam
PC	Propylene carbonate
PFA	Perfluoroalkoxy
PTFE	Poly(tetrafluoroethylene)
PVdF	Polyvinylidene difluoride
PXD	Powder X-ray diffraction
RGO	Reduced graphene oxide
SEI	Solid electrolyte interface
SEM	Scanning electron microscopy
SSM	Solid-state metathesis
TM	Transition metals
TEM	Transmission electron microscopy
TGA	Thermogravimetric analysis
XRD	X-ray diffraction

Contents

CHAPTER 1. INTRODUCTION	1
1.1 Development of rechargeable battery technologies	1
1.2 Sodium-ion batteries	5
1.2.1 Positive electrode materials for Na-ion batteries.....	8
1.2.2 Negative electrode materials for Na-ion batteries	13
1.2.3 Electrolytes for Na-ion batteries.....	17
1.3 Applications of transition metal nitrides	18
1.3.1 Hard coatings.....	19
1.3.2 Catalysis	19
1.3.3 Photocatalysis.....	20
1.3.4 Supercapacitors	21
1.3.5 Lithium-ion battery electrodes	21
1.4 Aims and Objectives	24
1.5 Reference.....	25
CHAPTER 2. EXPERIMENTAL TECHNIQUES	33
2.1 Powder X-Ray Diffraction (PXRD)	33

2.2 <i>Ex situ</i> X-ray Diffraction.....	36
2.3 Rietveld Refinement	37
2.4 Thermogravimetric Analysis	39
2.5 Infrared spectroscopy.....	40
2.6 Microanalysis	41
2.7 Brunauer-Emmett-Teller (BET) method	42
2.8 Transmission Electron Microscopy.....	43
2.9 The electrochemical techniques	44
2.9.1 Cyclic voltammetry.....	44
2.9.2 Galvanostatic method	45
2.9.3 Electrode preparation and cell construction.....	47
2.10 Reference	48

CHAPTER 3. NICKEL NITRIDE AS THE NEGATIVE ELECTRODE MATERIAL FOR SODIUM-ION BATTERIES.....51

3.1 Introduction.....	51
3.2 Synthesis and characterization of nickel nitride	52
3.2.1 Nickel nitride derived from ammonolysis of nickel hexamine nitrate.....	52
3.2.2 Nickel nitride derived from ammonolysis of nickel <i>tris</i> (ethylenediamine) nitrate....	55

3.3 Electrochemical performance of nickel nitride in battery applications	59
3.3.1 Nickel nitride as the negative electrode material for Li-ion batteries	60
3.3.2 Nickel nitride as the negative electrode material for Na-ion batteries	64
3.3.3 Effects of electrolytes on the performance of Ni ₃ N in sodium-ion batteries.....	72
3.4 Conclusions	73
3.5 Reference.....	74

CHAPTER 4. COPPER NITRIDE AS THE NEGATIVE ELECTRODE MATERIAL FOR SODIUM-ION BATTERIES 77

4.1 Introduction	77
4.2 Synthesis and characterization of copper nitride	78
4.2.1 Copper nitride derived from ammonolysis of anhydrous copper fluoride	78
4.2.2 Copper nitride derived from ammonolysis of copper pivalate	81
4.3 Electrochemical performance of copper nitride	85
4.3.1 Copper nitride as the negative electrode material for Na-ion batteries	85
4.3.2 Copper nitride as the negative electrode material for Li-ion batteries	91
4.3.3 CuO as the negative electrode material for Na-ion batteries.....	94
4.4 Conclusions	98
4.5 Reference.....	99

CHAPTER 5. TIN NITRIDE AS THE NEGATIVE ELECTRODE MATERIAL FOR SODIUM-ION AND BATTERIES 101

5.1 Introduction 101

5.2 Synthesis and characterization of tin nitride 103

5.2.1 Synthesis of Sn(NEt₂)₄ 103

5.2.2 Solution phase ammonolysis of Sn(NEt₂)₄ 104

5.2.3 Ammonolysis of polymeric tin amide precursor 105

5.3 Electrochemical performance of tin nitride in Na-ion batteries 108

5.4 Electrochemical performance of tin nitride in Li-ion batteries 119

5.5 Conclusions 125

5.6 Reference 126

CHAPTER 6. SCREENING OF OTHER METAL NITRIDES FOR SODIUM-ION BATTERIES 131

6.1 Chromium nitride 132

6.1.1 Synthesis and characterization of chromium nitride 133

6.1.2 Chromium nitride as the negative electrode material for Li-ion batteries 136

6.1.3 Chromium nitride as the negative electrode material for Na-ion batteries 140

6.2 Vanadium nitride 143

6.3 Molybdenum nitride.....	146
6.4 Manganese nitride	150
6.4.1 Manganese nitride as the negative electrode material for Li-ion cells	151
6.4.2 Manganese nitride as the negative electrode material for Na-ion cells	154
6.5 Zinc nickel nitride	156
6.6 Nickel phosphide.....	159
6.6.1 Synthesis and characterization of nickel phosphide.....	160
6.6.2 Nickel phosphide as the negative electrode material for Li-ion batteries	161
6.6.3 Nickel phosphide as the negative electrode material for Na-ion batteries	164
6.7 Capacity due to the acetylene black conductivity additive	167
6.8 Conclusions.....	170
6.9 Reference.....	172
CHAPTER 7. CONCLUSIONS AND FUTURE WORK.....	175
7.1 Conclusions.....	175
7.2 Future work	180
7.3 Reference.....	181

Chapter 1. Introduction

1.1 Development of rechargeable battery technologies

In 1859, the first-ever rechargeable battery, the lead-acid battery, was invented by Gaston Planté.¹ Although it is rather heavy and bulky, it did initiate the development of rechargeable batteries and is still used extensively. Thereafter, first alkaline battery was invented by a Swedish scientist named Waldemar Jungner by the end of 19th century. His rechargeable battery, the nickel-cadmium battery, consisted of nickel and cadmium electrodes in a potassium hydroxide solution. It was commercialized in Sweden in 1910.² With the advent of the 20th century, batteries had a wider application in many areas, which promoted the development of modern rechargeable batteries. A smaller and longer cycle life battery was developed in response to the market demands, and nickel–metal hydride batteries (NiMH) for smaller applications appeared on the market in 1989 as a variation of the 1970s nickel hydrogen battery.³ NiMH batteries tend to have longer lifespans than NiCd batteries. In the meantime, lithium batteries also had a rapid growth in the 1970s.

The first rechargeable lithium battery was proposed by Exxon Co., based on the work at Stanford University.⁴ They found that TiS_2 was favoured for the positive electrode material due to its high capacity, high chemical stability and excellent reversibility. Eventually, they designed a battery with a TiS_2 positive electrode, a lithium metal negative electrode and $\text{LiClO}_4/\text{dioxolane}$ electrolyte.⁴ But the safety issue arising from lithium dendrites irregularly deposited in the negative electrode was fatal to this type battery. During cycling tests, these derived dendrites could pierce the separator and

short-circuit occurred. These short circuits would lead to a sudden high discharge current accompanied by heat generation and eventually the organic electrolyte would be ignited. Moreover, during the discharge the lithium negative electrode is dissolved, with possible dendrite cutting and formation of isolated lithium from the negative electrode surface.⁵ This “dead lithium” is electrochemically inactive but chemically active, and they can accumulate on the negative electrode or float in the electrolyte, increasing the cell resistance. Even though Exxon did not commercialize their secondary lithium metal battery system, it did push lithium battery development, as the lithium metal safety issue triggered significant further research on lithium ion batteries.

In order to overcome this lithium dendrites issue, two approaches have been developed. One was to utilise a polymer electrolyte instead of non-aqueous electrolyte to prevent irregular lithium dendrites forming. In 1978, Armand firstly presented the use of a solvent-free polymer electrolyte derived from a complex between a lithium salt and a coordinating polymer (e.g., lithium triflate and poly(ethylene oxide), PEO) and demonstrated its efficient use in a rechargeable lithium polymer battery.⁶ Despite the feasibility of lithium polymer batteries from the Armand group and others, this type of battery has not entered the stage of large-scale commercialization, mainly because the concern about the risks of lithium metal electrodes cannot be totally eliminated.⁷

The other approach employed a negative intercalation electrode which operates as a “lithium sink” while the positive electrode acts as “lithium source”. Lithium ions can be transferred between these two electrodes and the process can be reversibly repeated. This system is called a lithium rocking chair battery. A schematic comparison between lithium and lithium-ion batteries is shown in Figure 1.1.⁸

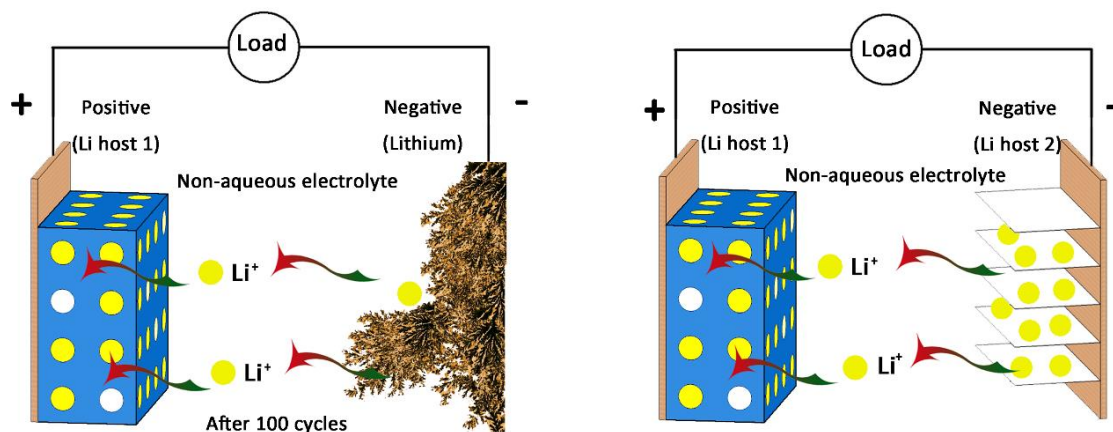
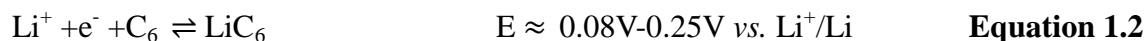


Figure 1.1 Schematic comparison between rechargeable Li-metal battery (left) and rechargeable Li-ion battery (right).⁸

Nevertheless, scientists realised no matter what material was used to replace lithium metal, the negative electrode potential would increase. As a result, the voltage of the positive electrode material must be as high as possible. In 1979, John Goodenough and Koichi Mizushima demonstrated a rechargeable battery with around 4 V range using lithium cobalt oxide.⁹ This electrode material is still commonly used in lithium ion batteries.



The key part to solve the potential safety issue of lithium ion batteries is to find an optimal alternative intercalation negative electrode material which has a low enough potential against lithium and safe performance. In 1977, Samar Basu demonstrated electrochemical intercalation of lithium ions into graphite at the University of Pennsylvania.^{10, 11} This is the basis of development of a feasible lithium intercalated graphite electrode at Bell Labs (LiC_6)¹² to offer a suitable negative electrode for lithium ion batteries.



Although these two components were practically demonstrated in the early 1980s, it took more than 10 years to convert the concept into a practical LiCoO_2 -graphite battery introduced by the Japanese Sony Company in June 1991. Their first worldwide lithium ion battery employs lithium cobalt oxide (LiCoO_2) as the positive electrode and graphite (C_6) as the negative electrode.¹³ Since then, lithium ion batteries with its high gravimetric and volumetric energy densities have been widely used in every area of our daily life.

Figure 1.2 compares these two parameters for different common rechargeable batteries.

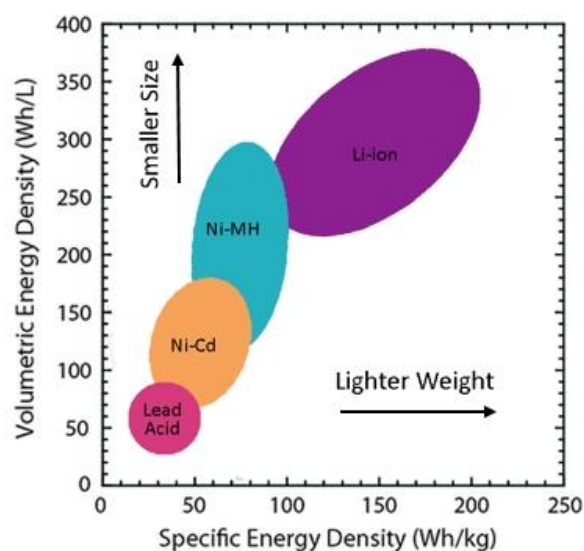


Figure 1.2 Comparisons between different common rechargeable battery technologies as a function of volumetric and gravimetric energy densities.^{7, 14}

Due to its high volumetric and gravimetric energy densities, lithium ion battery technology has wide range applications in daily life, such as portable devices (cell phones, cameras, laptops, etc.), implantable medical devices, professional power tools, robots, light electric vehicles and various military applications. Lithium ion batteries are

currently most successful battery chemistry, with a worldwide 10 billion dollars per year market. However, the successful commercialization of the lithium ion battery did not mark an end of its story. Scientists realised many aspects of lithium ion battery technology needed to be improved and significant efforts have been made to explore cheaper, greener, safer, and higher energy density lithium-ion battery systems.

Nanomaterials generally entered the energy storage field as they could effectively enlarge the electrode surface area, thereby shortening the diffusion path for ions and electrons.¹⁵

The advent of nanomaterials provided lithium ion batteries with a possibility of a jump in energy density and sustainability. In order to reduce the cost, there was a drive to substitute LiCoO_2 by less expensive and greener materials, such as LiFePO_4 ¹⁴ and spinel LiMn_2O_4 .¹⁶

Apart from focusing on lithium ion battery system, scientists also endeavoured to explore other alternative systems, such as lithium-air system, Li-S system or sodium-ion system.

1.2 Sodium-ion batteries

With the increase in the price of refined traditional fossil fuels, limitations on greenhouse gas emission and the increasing energy demands of modern society, renewable energy technologies have seen rapid growth in recent years. However, the prosperity of renewable energy technologies, such as wind power and solar power, also brings other concerns, in terms of energy storage and grid integration. Thus, to eliminate these concerns, a large-scale energy storage system is urgently needed. Against other large-scale energy technologies, such as pumped hydro, compressed air and fly-wheels, batteries can be a strong candidate technology in the future, as batteries have advantages

of flexibility, high energy conversion efficiency, and easy maintenance.¹⁷ Among current battery technologies, lithium ion batteries, the most common type rechargeable batteries in our daily life, can be a potential solution to these large-scale energy storage requirements, as lithium cells are now a mature technology, with high voltage (Li potential, -3.04 V versus standard hydrogen electrode) and high energy density (as shown in Figure 1.2). However, the fatal drawback of lithium ion batteries used for large-scale energy storage is the cost. The total global Li consumption in 2008 was around 21,280 tons and hence mineable lithium resources from the present could be sustained for approximately 65 years at most, considering an average growth of about 5% per year.¹⁸ Hence, it is reasonable to find an alternative to replace the lithium-ion battery system for large-scale energy storage.

Sodium, which is from the same group of the periodic table as lithium, has similar physical and chemical properties. But sodium resource is much more abundant and cheaper than lithium, as shown in Table 1.1.

Sodium batteries are not a new technology. They were initially researched alongside Li batteries in the late 1970s and through the 1980s.^{19, 20} However, the study of Na-ion batteries was significantly reduced after the success of the commercial application of Li-ion batteries in the 1990s. The first commercialised sodium battery was the sodium sulphur battery in the USA.²¹ It consists of molten sodium as the negative electrode housed within a sodium β'' -alumina tube which is surrounded by molten sulphur. It operates at near 300 °C where sodium and sulphur are molten, thereby removing concerns over internal short circuits due to dendrite formation. The good ionic conductivity of the sodium β'' -alumina membrane at the elevated temperatures further

benefits to lower the cell impedance. However, at this temperature, molten sulphur, sodium and the polysulfide compounds are highly corrosive. Although the strict conditions have to be applied, this type battery has been widely used for load-levelling and emergency power applications in 174 locations in six countries around the world, storing 305,000 kW of electricity in the late 1990s. Till September 2003, there was a battery fire erupted at the Tsukaba Plant in Japan.²⁰

Table 1.1 Comparisons between Li and Na elements^{22, 23}

	Li	Na
Natural abundance in Earth's crust	20 mg/kg	23600 mg/kg
Distribution	70% in South America	Everywhere
Cost (for carbonate)	\$5000/ton	\$5000/ton
Atomic weight	6.9	23 g/mol
Theoretical capacity (metal)	3829 mA h/g	1165 mA h/g
Normal electrode potential vs. SHE	-3.04 V	-2.7 V

Another commercialised molten sodium battery is called ZEBRA (Zero-Emission Battery Research Activities) cell which is based on Na/NiCl₂.²⁴



The advantage of this ZEBRA cell is that they can be assembled in the discharged state with NaCl, Al and nickel powders. Moreover, the positive electrode is made mostly of

solid materials which diminishes its corrosive impacts and makes the cell intrinsically safer than the Na–S cells.

Sodium-ion batteries are still at the research stage, a schematic diagram of how sodium-ion batteries might operate is shown in Figure 1.3.

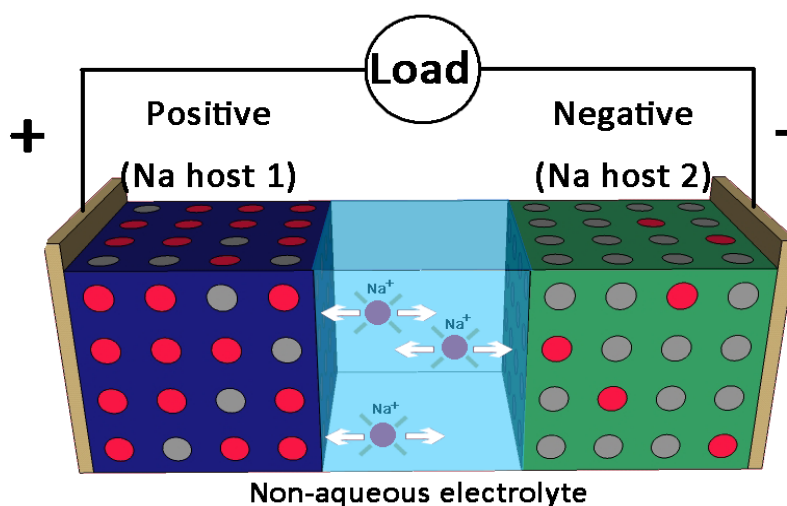


Figure 1.3 Typical schematic diagram of a sodium-ion battery.

Taking inspiration from lithium-ion batteries, most reports on sodium-ion batteries have used similar metal intercalating materials in the positive electrodes such as layered transition metal oxides^{25, 26} and olivine²⁷ materials. However, the negative electrode is one of the most troublesome components of sodium-ion cells, since typical graphitic carbons widely employed in Li-ion cells cannot be used.²⁸ Details related to sodium-ion batteries in terms of positive electrode materials, negative electrode materials and electrolyte will be discussed as follows.

1.2.1 Positive electrode materials for Na-ion batteries

As sodium-ion batteries have a similar intercalation or conversion mechanism as used in

lithium-ion batteries, the choice of positive electrode materials often takes inspiration from Li-ion batteries.

Transition metal (TM) oxides

Delmas and co-workers first classified A_xMO_2 compounds by describing the stacking arrangements of alkali ions between layers,²⁹ and applying this to different layered transition metal oxides. In Figure 1.4, O or P represents octahedral or trigonal prismatic coordination environment of alkali ions; the number 3 or 2 describes the number of TM layers in a repeated stacking unit, and O`3 and P`2 represent the monoclinic distortion of O3 and P2 phase packing. Inspired by $LiCoO_2$, the insertion of Na in Na_xCoO_2 was initially investigated by Delmas *et al.*³⁰ The reversible phase transition of O3- $NaCoO_2$ was $O3 \rightarrow O`3 \rightarrow P`3$, within a Na content range of $0.5 \leq x \leq 1$. Thereafter, other phase $NaCoO_2$ compounds were extensively studied as positive electrode materials for sodium-ion batteries.^{31,32} Likewise, Na_xMnO_2 is another candidate that was investigated early on. Several phases have been studied in sodium cells and it can deliver a reasonably good reversible capacity, *ca.* 140 mA h g⁻¹ for P2- $Na_{0.6}MnO_2$ ³³ and 185 mA h g⁻¹ for monoclinic α - $Na_{0.6}MnO_2$.³⁴ However, the instability of the structure leads to a rapid capacity decay in the first cycles. Employing another TM element or an alkali ion to replace a quantity of Mn^{3+} may stabilize the structure of Na_xMnO_2 and improve its cycle stability as in the case of Li-ion batteries.^{35,36} $Na_{1.0}Li_{0.2}Ni_{0.25}Mn_{0.75}O_y$, proposed by Johnson`s group, showed a reversible capacity of 100 mA h g⁻¹ with good cycle life and rate capability.³⁷

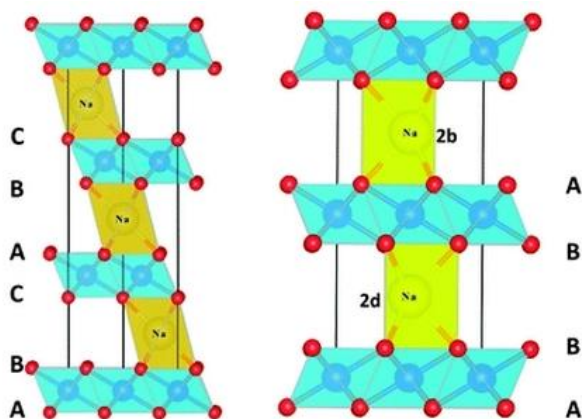


Figure 1.4 The stacking types of O3 (left) and P2 (right) phases in A_xMO_{2+y} . In the P2-structure, Na ions occupy the 2d site sharing the edges with the MO_6 octahedra or occupy the 2b site sharing two faces with the MO_6 octahedra. (reproduced with permission²²)

Apart from the Mn^{4+}/Mn^{3+} redox couple, the Fe^{4+}/Fe^{3+} redox couple has also drawn much attention due to the inexpensive and low toxic characteristics of iron compounds. $NaFeO_2$ exhibited a reversible Na storage at 3.3 V with a small voltage polarization.³⁸ In contrast, its Li analogue $LiFeO_2$ is almost electrochemically inactive on the basis of Fe^{4+}/Fe^{3+} conversion.³⁹ Similarly, $NaCrO_2$ has same structure as $LiCrO_2$, $NaCrO_2$ can deliver a reversible capacity of around 120 mA h g^{-1} with satisfactory capacity retention during cycling,⁴⁰ while $LiCrO_2$ is electrochemically inactive.

$Na_{0.44}MnO_2$, firstly prepared via a solid-state route by Sauvage *et al.*, has a structure comprised of wide tunnels which attracted attention as a possible positive electrode material for intercalation.⁴¹ Insertion/deinsertion of sodium revealed capacities as high as 140 mA h g^{-1} over the course of multiple voltage steps (six biphasic transitions) within a potential range of 2–3.8 V. Cao *et al.* reported a capacity of 128 mA h g^{-1} in $Na_4Mn_9O_{18}$ nanowires at a current rate of 0.1 C ($0.1 \times$ theoretical capacity per hour) and 77% capacity retention after 1000 cycles at a rate of 0.5 C.⁴²

Phosphates

Compounds based on the 3-D structure of NASICON (NAtrium Super Ion CONductor) have been extensively studied for their structural stability and fast ion conduction.

Sodium intercalation in $\text{Na}_3\text{V}_2(\text{PO}_4)_3$ was studied in 2002 by Yamaki *et al.*⁴³ The capacity of this compound was found to be 50 mA h g^{-1} at 1.6 V versus Na, when initially reduced.

After the material was oxidised to the original stoichiometry, the material could be further oxidised at 3.4 V versus Na and the reduction capacity at this step was 90 mA h g^{-1} .

However, the cycling stability of this material was poor. Recently, a carbon coated

$\text{Na}_3\text{V}_2(\text{PO}_4)_3$ with 1M NaFSI/PC electrolyte was proposed by Hu *et al.*⁴⁴ The

electrochemical performance was largely improved to 107 mA h g^{-1} with 98.7% initial

Coulombic efficiency and 99.8% in subsequent cycles (Figure 1.5). From the *in situ*

XRD measurement, a two-phase conversion between $\text{Na}_3\text{V}_2(\text{PO}_4)_3$ and $\text{NaV}_2(\text{PO}_4)_3$ was observed.

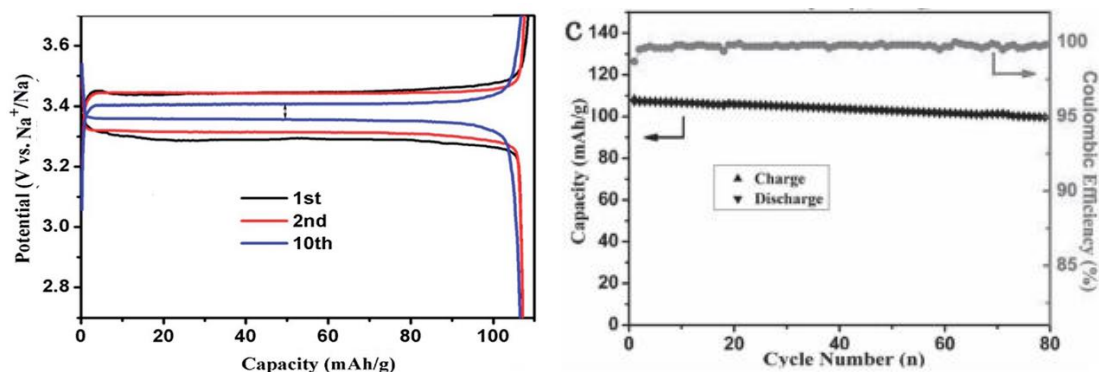


Figure 1.5 Voltage profile (left) Coulombic efficiency and specific reversible capacity versus cycle number (right) of $\text{Na}_3\text{V}_2(\text{PO}_4)_3/\text{C}$ -sodium half cells in NaFSI/PC electrolyte at a current rate of C/10 in a voltage range of 2.7–3.7 V vs. Na^+/Na (Reproduced with permission⁴⁴).

Inspired by the success of LiFePO_4 in Li-ion batteries, olivine NaFePO_4 obtained via

electrochemical Na insertion into heterosite FePO_4 , was studied by Morea *et al.*²⁷ In contrast to LiFePO_4 for lithium-ion batteries, NaFePO_4 exhibited an intermediate phase of $\text{Na}_{0.7}\text{FePO}_4$ at 2.95 V during oxidation process. And it can offer a stable capacity of 125 mA h g^{-1} over 50 cycles with the working plateau at 2.7 V.⁴⁵

Sauvage *et al.* produced $\text{Na}_3(\text{VO})_2(\text{PO}_4)_2\text{F}$ which exhibited a reversible capacity of 87 mA h g^{-1} over the course of two different voltage plateaus at 3.6 V and 4.0 V versus Na.⁴⁶

This material was employed for a unique hybrid Na/Li-ion cell with graphite as the negative electrode and a lithium salt electrolyte.⁴⁷ Cycling data collected at current rates of C/2 and 2 C exhibited an initial reversible capacity of $115\text{--}120 \text{ mA h g}^{-1}$, and the cells cycled with little capacity fade behaviour after 400 cycles. Recently, this material was also studied for sodium ion batteries by Kang's group, and it showed a 120 mA h g^{-1} capacity with two similar plateaus at 3.7 V and 4.2 V.⁴⁸

Hexacyanoferrates and Fluorides

Goodenough and co-workers recently reported a prussian blue framework structure, $(\text{KFe}_2(\text{CN})_6)$, with a reversible capacity of around 100 mA h g^{-1} with conversion of $\text{Fe}(\text{CN})_6^{3-}/\text{Fe}(\text{CN})_6^{4-}$ and no capacity fade in 30 cycles.⁴⁹ Although this material showed low toxicity, good electrochemical performance as well as low cost advantages, the environmental impacts and safety issues related to the water and river are not clear.

Perovskite transition metal fluorides MF_3 and NaMF_3 (M= Ni, Fe, Mn) were studied as positive electrode materials for Na-ion cells. Ball-milled FeF_3/C composite delivers an initial reduction capacity of 150 mA h g^{-1} via the $\text{Fe}^{3+}/\text{Fe}^{2+}$ conversion.⁵⁰ NaFeF_3 showed an initial high reversible capacity of 197 mA h g^{-1} in a voltage range of 1.5–4 V with the

large voltage polarization.⁵¹

Organic compounds

Organic electrode materials are deemed to be promising options to replace current electrode materials for rechargeable batteries, because of their green synthesis, low cost and easy recyclability.⁸ However, it is not easy to successfully use organic electrode materials either in Li- or Na-ion batteries, due to their high solubility in organic electrolytes, low thermal stability, sluggish kinetics, and particularly poor electronic conductivity.⁵² In 2012, aniline–nitroaniline copolymer was reported by Yang's group, which can offer a reversible capacity of 180 mA h g⁻¹ at an average voltage of around 3.2 V with good capacity retention.⁵³ After that, Kaskel *et al.* presented a bipolar porous organic electrode (BPOE) consisting of aromatic rings in a porous-honeycomb structure showing 3.3 V and 2.3 V plateau with p-type and n-type doping process.⁵⁴

1.2.2 Negative electrode materials for Na-ion batteries

Graphite is widely employed as the negative electrode material for lithium-ion batteries as it can intercalate large amounts of lithium (up to one per C₆ unit) and retain a low potential even with small lithium loadings. Sodium ions do not intercalate into graphite and so graphite cannot be used for sodium-ion batteries,²⁸ hence the negative electrode is a key challenge for the development of viable sodium-ion batteries.

Carbon based materials

Carbon-based materials dominated the negative electrode literature for sodium-ion batteries.⁵⁵⁻⁶⁰ The first useful carbon material, from decomposition of a glucose precursor,

was published by Stevens *et al.*⁵⁵ They concluded that the sloping and low-voltage region could be due to the insertion of Na metal into random stack layers. This result has been confirmed by NMR study for the electrochemical insertion of Na into hard carbon.⁶¹ Alcántara *et al.* reported that carbon black can offer a reversible capacity close to 200 mA h g⁻¹ at a low cycling rate (C/75, the current required to insert sodium into carbon electrode to form NaC₆ in 75 hours).⁵⁶ More recently, Wenzel *et al.* used porous silica templates to prepare templated carbon which can provide a 180 mA h g⁻¹ capacity in the first reduction cycle at 0.5 C, though this decreased to around 120 mA h g⁻¹ after 40 cycles.⁵⁷ This is still a good cycling performance compared with most published carbon materials. Very recently, Cao *et al.*⁵⁸ reported hollow carbon nanowires (HCNW) prepared from pyrolysis of hollow polyaniline nanowires that can deliver an initial capacity of 251 mA h g⁻¹ and retain 206.3 mA h g⁻¹ after 400 cycles at 0.2 C (Figure 1.6), a better cycle stability than any other carbon-based materials.

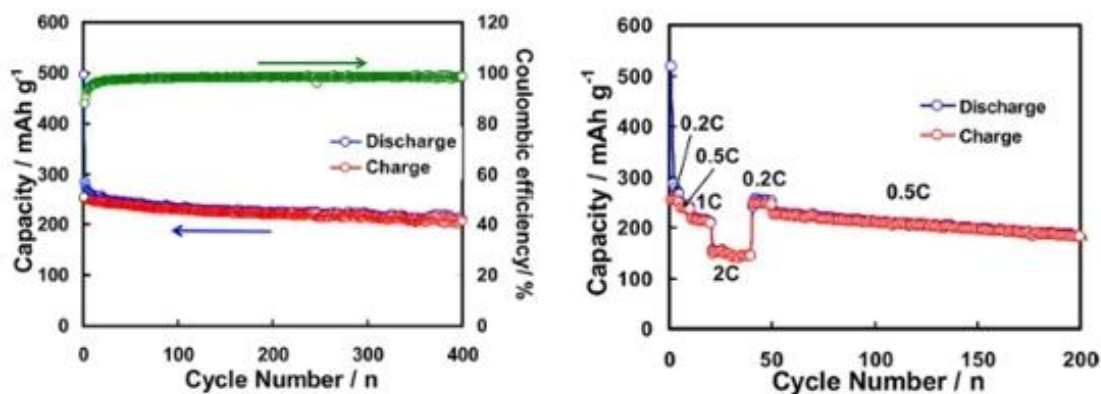


Figure 1.6 Cycling performance (left) of the HCNW electrode in sodium half-cell at 50 mA g⁻¹ for 400 cycles and rate capability of the HCNW electrode at different current rates of 50 (0.2 C), 125 (0.5 C), 250 (1 C) and 500 (2 C) mA g⁻¹ (reproduced with permission⁵⁸)

Alloy materials

Inspired by Li system, alloys have attracted extensive interests in Na-ion batteries.⁶²⁻⁶⁸ Komaba *et al.* reported that Sn electrodes can deliver a capacity of 500 mA h g⁻¹ in a stoichiometric form of Na₁₅Sn₄ in a voltage range of 0–0.8 V.⁶⁹ Nano composite of Sb/C can exhibit a 610 mA h g⁻¹ capacity with good rate capability.⁶³ And SnSb/C nanocomposites can provide over 400 mA h g⁻¹ capacity after 50 cycles at 100 mA g⁻¹.⁶⁴ However, the poor solid-electrolyte interphase (SEI) stability resulted from the large volume changes after Na insertion into these alloys is similar to that in Li-ion batteries, which could be detrimental to the cycle stability.⁷⁰ Recently, amorphous phosphorus/C composites were investigated to offer the highest capacity of around 1800 mA h g⁻¹ with a potential of 0.4 V vs. Na⁺/Na and stable cycling performance.⁶⁸

Oxides, sulphides and phosphides

Na₂Ti₃O₇ was studied by the Palacin group,⁷¹ which can hold 2 Na ions at a rather low voltage of 0.3 V vs. Na⁺/Na, but the Coulombic efficiency and cycle performance of this material is not good. Hu *et al.* demonstrated Li₄Ti₅O₁₂ to exhibit a reversible capacity of 150 mA h g⁻¹ with an average storage voltage of 0.91 V.⁷² A new reversible three-phase reaction of $2\text{Li}_4\text{Ti}_5\text{O}_{12} + 6\text{Na} \leftrightarrow \text{Li}_7\text{Ti}_5\text{O}_{12} + \text{Na}_6\text{LiTi}_5\text{O}_{12}$ was proposed, which implied a Na storage mechanism that differs from that of the Li system where a typical two-phase reaction is expected. Recently, the layered Na_{0.66}[Li_{0.22}Ti_{0.78}]O₂ system was investigated, which has only ~0.77% volume change during sodium insertion/extraction and good stability, although its specific capacity of 118 mA h g⁻¹ at 0.1 C is relatively low.⁷³

Based on a conversion mechanism (converting metal oxides into metal and sodium oxides), spinel NiCo₂O₄ can offer a reversible capacity of 200 mA h g⁻¹ with low initial Coulombic efficiency (35%). Several phases of iron oxide nanoparticles have been

investigated showing a reversible capacity of 160-189 mA h g⁻¹ with moderate cycling performance and low cost.^{74, 75} Very recently, Fe₂O₃ nanocrystals anchored onto graphene nanosheets were investigated and showed to exhibit a 400 mA h g⁻¹ capacity with stable cycle performance at 100 mA g⁻¹.⁷⁶

MoS₂/graphene composite paper was proposed by researchers at Kansas State University as self-standing flexible electrodes in sodium-ion batteries.⁷⁷ They can provide a stable specific capacity of approximately 230 mA h g⁻¹ with respect to total weight of the electrode. Antimony sulphide on graphene shows a high capacity of 730 mA h g⁻¹ at 50 mA g⁻¹ with a good rate capability of 6 C and moderate capacity retention. Similarly, a layered SnS₂-reduced graphene oxide (SnS₂-RGO) composite was evaluated in Na-ion cells, based on the conversion and alloy process. It exhibited a high specific capacity of 500 mA h g⁻¹ at 1 A g⁻¹ for 400 cycles and good rate capability.⁷⁸

Phosphides have attracted researchers' interests in recent years. NiP₃ was reported by Monconduit group in 2013. They compared the electrochemical performance of NiP₃ in Li- and Na-ion batteries.⁷⁹ In sodium ion batteries, it can offer a high reversible capacity of 900 mA h g⁻¹ after 15 cycles. In 2014, Sn₄P₃/C composite was proposed to be a promising negative electrode material in sodium ion batteries.⁸⁰ It can deliver a reversible capacity of 850 mA h g⁻¹ and can also be cycled with 86% capacity retention after 150 cycles. A synergetic sodium storage mechanism also proposed, where the Sn nanoparticles can act as electronic channels to enable electrochemical activation of the P component, while the sodiated product Na₃P serves as a host matrix to alleviate the cell expansion of the Sn particles during Na insertion reaction.

Organic compounds

Similar to positive electrode materials, organic compounds can be good candidates for the next generation electrode materials in Na-ion batteries due to their low cost and facile synthesis. Hu *et al.* investigated disodium terephthalate, $\text{Na}_2\text{C}_8\text{H}_4\text{O}_4$, which delivered a reversible capacity of 250 mA h g^{-1} , based on the reaction of Na ions with C=O bonds.⁸¹ It showed a two-electron transfer at an average voltage of 0.45 V and an appropriate cycle performance. However, due to the low conductivity of most organic compounds, a large amount of carbon black is needed, which results in low initial Coulombic efficiency. Bulk $\text{Na}_2\text{C}_6\text{O}_6/\text{C}$ composite was studied by Chihara and co-workers, and it can offer a high reversible capacity of 270 mA h g^{-1} , though the Coulombic efficiency and cycling stability of this material needed to be improved.⁸²

1.2.3 Electrolytes for Na-ion batteries

NaClO_4 is the most commonly used electrolyte salt for sodium-ion batteries, but Vidal-Abarca *et al.*⁸³ reported that compared to the strong oxidant characteristic of NaClO_4 , NaPF_6 salt is safer as the electrolyte salt. Ethylene carbonate (EC), propylene carbonate (PC), butylene carbonate (BC), and dimethyl carbonate (DMC) have all been used as the solvent in sodium-ion batteries. Komaba *et al.* compared a range of organic solvents and found that using PC: DMC can provide a better cell performance than with other types of organic solvents.² In contrast, when using $\text{Na}_2\text{FePO}_4\text{F}$ as the positive electrode material, Vidal-Abarca *et al.* concluded that cells using EC:DEC as solvent and NaPF_6 as the salt exhibited higher reduction capacity and capacity retention than those using PC as the solvent.⁸³ In 2012, Ponrouch *et al.*⁸⁴ have studied various

electrolytes containing diverse solvent mixtures (cyclic, acyclic carbonates, glymes) and Na-based salts having either F-based or perchlorate anions and measured viscosity, ionic conductivity, and thermal and electrochemical stability for sodium-ion batteries. They found that the binary EC:PC solvent mixture has emerged as the best solvent formulation no matter what kinds of salts were used. Moreover, when EC:PC solvent was selected, both NaClO₄ and NaPF₆ can offer a similar performance in hard carbon based sodium half cells. Hence, considering safety issues, NaPF₆ is an optimal electrolyte salt for Na-ion cells. Apart from the intrinsic parameters of the electrolyte, the additive is essential. Fluorethylene carbonate (FEC) has been widely demonstrated in Na-ion cells, in terms of hard carbon electrodes⁸⁵, alloy electrodes⁶⁹ and conversion based electrodes.⁸⁶ It can effectively stabilize the solid electrolyte interphase (SEI) and enhance the reversibility of electrochemical Na insertion.⁸⁵

1.3 Applications of transition metal nitrides

Transition metal nitrides form a class of materials with unique physical properties which provide them varied applications, as high temperature ceramics, magnetic materials, superconductors or catalysts.⁸⁷ There are plenty of reviews focused on the chemistry of nitride materials in terms of catalysis,⁸⁸ structure,^{89,90} phosphors⁹¹ and silicon nitride ceramics.⁹² For example, GaN and InN thin films are widely used in blue-UV optoelectronic and microelectronic devices.⁹³⁻⁹⁵ Moreover, due to the luminescence properties of silicon-based oxynitride and nitride phosphors, they have attracted much attention for their potential use of white light-emitting diodes (LEDs).⁹¹ These systems are activated by doping with rare-earth ions (e.g. Eu²⁺ and Ce³⁺) to yield high performance white LEDs. There is increasing interest in the crystallite shape and size

dependent properties of transition metal nitrides to develop their new applications, such as GaN for semiconductors,⁹⁵ $\text{Co}_3\text{Mo}_3\text{N}$ for catalysts⁹⁶ and TiN for hard materials.⁹⁷

1.3.1 Hard coatings

Hard protective coatings have been used for machine tools, suspension components, drilling, cutting, and milling. Ideal materials for such applications must be hard, resistant against oxidation and have low coefficient of friction.⁹⁸ Although different materials possess a high hardness the choice of good candidates is often difficult. For example amorphous carbide has a high hardness but its use is limited because of the easy oxidation at low temperature while polycrystalline diamond films forms alloys at high temperature with materials like steel or iron. The increasing requirements in superhard coatings have led to development of composite nanocrystalline/amorphous materials. Metal nitrides of group 4 (TiN, ZrN and HfN) and 5 (VN, NbN and TaN) have been used as hard protective coatings for cutting tools^{99, 100} and UHV system components.

1.3.2 Catalysis

Due to their excellent catalytic activity, transition metal nitrides of groups 4-6 have received massive attention in catalysis. Early transition metals are electron deficient in their elemental state, and present high reactivity towards hydrocarbons¹⁰¹. For example, in ammonia synthesis, the replacement of ruthenium with Mo_2N resulted in higher activity¹⁰². Ammonia synthesis has also been effective with W_2N , VN and vanadium oxynitride¹⁰³⁻¹⁰⁵. Moreover, Mo_2N was used in dehydrogenation, hydrogenolysis and isomerisation of butane¹⁰⁶ and Mo_2N can also be employed as a base catalyst in the

conversion from acetone to isophorone and mesityl oxide¹⁰⁷. Nanocrystalline TiN has been used to accelerate hydrogen transfer in the reaction of diphenylethyne (DPE) with NaAlH₄.¹⁰⁸ The uncatalyzed reduction of DPE was slow at 328 K and produced two isomers (E- and Z-stilbene) in ratio 70:30. The activation of the reaction with TiN was faster and highly stereoselectivity towards the formation of Z-stilbene (~90%). An almost complete conversion (~ 99%) in isomers E-(10%) and Z-stilbene (90%) was produced after 5 h. In the hydrogenation of DPE, TiN decomposes the alanate (NaAlH₄) into NaH and AlH₃, then AlH₃ is responsible for the reduction and the selectivity of Z-stilbene¹⁰⁸. Nitrides used in catalysis have been usually prepared from oxide precursors and a lot of interests are addressed toward the production of nitride phases by other routes that can produce high surface area structures.

1.3.3 Photocatalysis

Transition metal nitrides have also been used for photocatalysis. For example, Ta₃N₅ has a band gap of 2.08 eV¹⁰⁹ and is an active photocatalyst which absorbs in the visible region. TiO₂ has a wide band gap ranging from 3 eV for rutile to 3.2 eV for anatase and this represents a limitation in its use because the most intense region in the solar spectrum is around 2.6 eV.¹¹⁰ Various works have attempted to improve the photocatalytic properties of TiO₂ with the aim to extend its absorption into the visible region. The photocatalytic activity of Ta₃N₅ and nanocrystalline TiO_{2-x}N_x were investigated in mesitylene blue degradation.¹¹¹ In that work Ta₃N₅ showed higher activity than TiO_{2-x}N_x of the same size. The use of carbon nanotube composite (CNTs/Ta₃N₅) photocatalysts presented higher photocatalytic activity than pure Ta₃N₅ in the degradation of mesitylene blue.¹¹² Hf₃N₄ has also been proposed for use as a

photocatalyst.¹¹³

1.3.4 Supercapacitors

The high specific power, fast charging and long cycle life of electrochemical capacitors have drawn great interest for a wide range of potential applications including hybrid and electric vehicles and portable electronics.¹¹⁴ There two types of supercapacitors, the electrochemical double-layer capacitors (EDLC) and pseudocapacitors.¹¹⁵ High surface activated carbon materials and several metal oxides such as RuO_2 ¹¹⁶, MnO_2 ¹¹⁷, TiO_2 ¹¹⁸ have been employed as electrode materials for supercapacitors. Specifically, crystalline RuO_2 ¹¹⁹ and amorphous $\text{RuO}_2 \cdot n\text{H}_2\text{O}$ ^{116, 120} exhibited high capacitance of 350 and 720 F g^{-1} , respectively. In recent years, transition metal nitrides like VN ¹²¹, TiN ¹²² and MoN_x ¹²³ have been found to be alternatives for RuO_2 as electrode materials for supercapacitors due to their high conductivity, low cost and high chemical stability. Take VN as an example,¹²¹ rock-salt VN with particle size of about 6 nm was obtained at 400 °C with a specific area of $38.8 \text{ m}^2 \text{ g}^{-1}$, while crystallites of 58 nm were prepared at 1000 °C with a specific area of $2.4 \text{ m}^2 \text{ g}^{-1}$. The specific capacitance measured from VN prepared at 400 °C was 1340 F g^{-1} at a scan rate of 2 mV s^{-1} , 554 F g^{-1} at 1000 mV s^{-1} and 190 F g^{-1} at a scan rate of 2 V s^{-1} .¹²¹

1.3.5 Lithium-ion battery electrodes

The advent of the 21st century brought interests onto a new reactivity concept with the reversible electrochemical reaction of lithium with transition metal oxides,¹²⁴ according to what is conventionally referred to as “conversion reaction,” generalized as follows:

**Equation 1.4**

where M = transition metal, X = anion, and n = formal oxidation state of X. The typical voltage versus electrode composite graph of an electrode using conversion reaction based material is shown in Figure 1.7.

Transition metal nitrides have been reported to be suitable for this conversion reaction when prepared as crystallized (e.g., CrN, VN, CoN, Co₃N, Fe₃N, Mn₄N) or amorphous (e.g. Ni₃N) thin films.¹²⁵⁻¹²⁹ For the nitride phases with N/M < 1, specific capacities of around 400–500 mA h g⁻¹ were typically achieved in the first reduction cycle, close to the theoretical values for the conversion reaction. Although un-reacted Li₃N and metal can often be observed after the first charge, capacities of approximately 350–400 mA h g⁻¹ are mostly retained upon cycling with minor fluctuations.¹³⁰ In contrast, for nitrides with N/M = 1, much higher capacities, in excess of 1000 mA h g⁻¹ in some cases, were found, which is attributed to the larger amount of nitrogen present in the structure. For example. CrN and VN exhibited very high capacities during the first reduction (1800 mA h g⁻¹ and 1500 mA h g⁻¹, respectively, slightly higher than the theoretical value, *ca.* 1200 mA h g⁻¹). Although part of the capacity loss can be attributed to the residual reduced metal found after the oxidation, 1200 mA h g⁻¹ capacity is obtained after the second reduction, and the value remains relatively stable upon cycling in the case of CrN.^{128, 129} CoN thin films exhibited first reduction capacities of 950 mA h g⁻¹ that were again only partially reversible, but 650 mA h g⁻¹ were still observed after 50 cycles at very high rates.

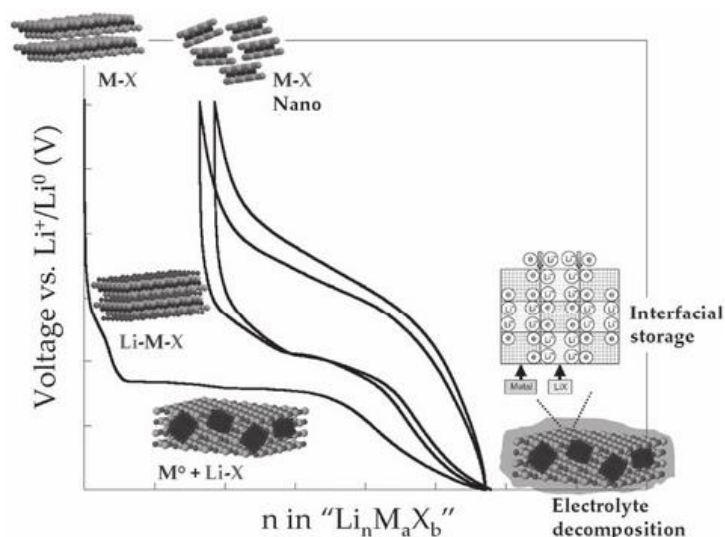


Figure 1.7 Typical voltage versus composition profile of the first two and half cycles for an electrode containing a material that reacts through a conversion reaction, measured against a Li counter-electrode (reproduced with permission¹³⁰).

In some cases, cyclic voltammetry experiments on lithium-metal nitride cells showed the presence of diverse peaks that have been associated with the possible formation of ternary Li-M-N phases,^{125, 131, 132} but no definitive experimental evidence has been provided so far. For example, Cu_3N powder, which undergoes a conversion reaction with formation of Li_3N and Cu, showing an initial change of the lattice parameters consistent with intercalation before the phase change.¹³² High capacity (675 mA h g^{-1}) and good capacity retention are observed at moderately high rates in this system. However, upon prolonged cycling additional redox features were also observed, presumably due to the formation of copper oxides, claimed to be associated with the electrolyte degradation. This observation highlighted the complexity of the reactions taking place in transition metal nitride electrodes in lithium-ion cells.

In very recent papers, a hybrid charge storage mechanism has been proposed using

transition metal nitrides, such as SiN_x ^{133, 134} and Sn_3N_4 ¹³⁵ in lithium-ion cells. This hybrid mechanism combines conversion reactions and alloying processes where metal nitrides are reduced to metal and Li_3N due to conversion reaction and then the reduced metal (Si or Sn) is alloyed with lithium to accommodate more lithium ions. With more lithium ions transferred during the reduction, the capacity is high, e.g. $\text{SiN}_{0.92}$, it can provide more than 1300 mA h g^{-1} capacity over 100 cycles with a low voltage plateau near to 0.5 V.

1.4 Aims and Objectives

Sodium-ion batteries undergone a rapid development in recent years and have great potential to be a strong alternative to lithium-ion batteries for renewable energy storage. Taking inspiration from lithium-ion batteries, the electrode materials selection and charge storage mechanism in sodium-ion cells are developed. However, for the negative electrodes in lithium-ion batteries, the widely used graphite cannot be intercalated by sodium ions which brings a challenge for the development of negative electrode materials in sodium-ion batteries.²⁹ In lithium-ion batteries, the conversion reaction mechanism has been examined to offer a higher gravimetric specific capacity than traditional intercalation reaction,¹³⁰ and metal nitrides have been reported to be suitable for this conversion reaction.¹²⁵⁻¹²⁹

In this project, the main aim is to investigate the suitability of metal nitrides as negative electrode materials in sodium-ion batteries.

Specifically, metal nitrides, such as Ni_3N , Cu_3N and Sn_3N_4 , have been prepared from different routes with the aim of obtaining nanocrystalline samples, and characterized by

several techniques, e.g. powder XRD, TEM, and IR. Thereafter, their electrochemical performance was explored in sodium- and lithium-ion batteries and evidence for the charge storage mechanism was collected. In addition, other metal nitrides which have shown a good performance in other areas such as supercapacitors or have a promising morphology, will be examined as negative electrode materials in sodium- and lithium-ion batteries.

1.5 Reference

1. R. M. Dell and D. A. J. Rand, *Understanding Batteries*, Royal Society of Chemistry, 2001.
2. C. D. S. Tuck, *Modern Battery Technology*, London: Ellis Harwood, 1991.
3. N. Furukawa, *J. Power Sources*, 1994, 51, 45.
4. A. H. Thompson, *Phys. Rev. Lett.*, 1978, 40, 489.
5. W. S. Kim and W. Y. Yoon, *Electrochim. Acta*, 2004, 50, 541.
6. M. Armand, *Solid State Ionics*, 1983, 9–10, Part 2, 745.
7. B. J. Landi, M. J. Ganter, C. D. Cress, R. A. DiLeo and R. P. Raffaele, *Energy Environ. Sci.*, 2009, 2, 638.
8. J. M. Tarascon and M. Armand, *Nature*, 2001, 414, 359.
9. K. Mizushima, P. C. Jones, P. J. Wiseman and J. B. Goodenough, *Mater. Res. Bull.*, 1980, 15, 783.
10. M. Zanini, S. Basu and J. E. Fischer, *Carbon*, 1978, 16, 211.
11. S. Basu, C. Zeller, P. J. Flanders, C. D. Fuerst, W. D. Johnson and J. E. Fischer, *Mater. Sci. Eng.*, 1979, 38, 275.
12. S. Basu, Google Patents, 1981.
13. T. Nagaura and K. Tozawa, *Prog. Batteries Solar Cells*, 1990, 9, 209.

14. A. K. Padhi, K. S. Nanjundaswamy and J. B. Goodenough, *J. Electrochem. Soc.*, 1997, 144, 1188.
15. A. S. Arico, P. Bruce, B. Scrosati, J.-M. Tarascon and W. van Schalkwijk, *Nat. Mater.*, 2005, 4, 366.
16. M. M. Thackery, *J. Electrochem. Soc.*, 1995, 142, 2568.
17. B. Dunn, H. Kamath and J. M. Tarascon, *Science*, 2011, 334, 928.
18. C.-X. Zu and H. Li, *Energy Environ. Sci.*, 2011, 4, 2614.
19. A. van Zyl, *Solid State Ionics*, 1996, 86–88, Part 2, 883.
20. B. L. Ellis and L. F. Nazar, *Curr. Opin. Solid State Mater. Sci.*, 2012, 16, 168.
21. N. W. J.T. Kummer, *US Patent*, 1968, US 3413150.
22. H. Pan, Y.-S. Hu and L. Chen, *Energy Environ. Sci.*, 2013, 6, 2338.
23. M. D. Slater, D. Kim, E. Lee and C. S. Johnson, *Adv. Funct. Mater.*, 2013, 23, 947.
24. J. L. Sudworth, *J. Power Sources*, 2001, 100, 149.
25. A. Mendiboure, C. Delmas and P. Hagenmuller, *J. Solid State Chem.*, 1985, 57, 323.
26. A. Bhide and K. Hariharan, *Solid State Ionics*, 2011, 192, 360.
27. P. Moreau, D. Guyomard, J. Gaubicher and F. Boucher, *Chem. Mater.*, 2010, 22, 4126.
28. P. Ge and M. Fouletier, *Solid State Ionics*, 1988, 28–30, Part 2, 1172.
29. C. Delmas, C. Fouassier and P. Hagenmuller, *Phys. B+C*, 1980, 99, 81.
30. C. Delmas, J.-J. Braconnier, C. Fouassier and P. Hagenmuller, *Solid State Ionics*, 1981, 3–4, 165.
31. L. W. Shacklette, T. R. Jow and L. Townsend, *J. Electrochem. Soc.*, 1988, 135, 2669.
32. R. Berthelot, D. Carlier and C. Delmas, *Nat. Mater.*, 2011, 11, U74.
33. A. Caballero, L. Hernan, J. Morales, L. Sanchez, J. Santos Pena and M. A. G.

- Aranda, *J. Mater. Chem.*, 2002, 12, 1142.
34. X. Ma, H. Chen and G. Ceder, *J. Electrochem. Soc.*, 2011, 158, A1307.
35. M. Dollé, S. Patoux and M. M. Doeff, *Chem. Mater.*, 2005, 17, 1036.
36. S. Patoux, M. Dollé and M. M. Doeff, *Chem. Mater.*, 2005, 17, 1044.
37. D. Kim, S.-H. Kang, M. Slater, S. Rood, J. T. Vaughey, N. Karan, M. Balasubramanian and C. S. Johnson, *Adv. Energy Mater.*, 2011, 1, 333.
38. J. Zhao, L. Zhao, N. Dimov, S. Okada and T. Nishida, *J. Electrochem. Soc.*, 2013, 160, A3077.
39. S.-T. Myung, S. Komaba, N. Hirosaki, N. Kumagai, K. Arai, R. Kodama and I. Nakai, *J. Electrochem. Soc.*, 2003, 150, A1560.
40. S. Komaba, T. Nakayama, A. Ogata, T. Shimizu, C. Takei, S. Takada, A. Hokura and I. Nakai, *ECS Trans.*, 2009, 16, 43.
41. F. Sauvage, L. Laffont, J. M. Tarascon and E. Baudrin, *Inorg. Chem.*, 2007, 32, 3298.
42. Y. Cao, L. Xiao, W. Wang, D. Choi, Z. Nie, J. Yu, L. V. Saraf, Z. Yang and J. Liu, *Adv. Mater.*, 2011, 23, 3155.
43. Uebou.Y, Kiyabu.T, Okada.S and Yamaki.J-I, *Rep. Inst. Adv. Mater. Study*, 2002, 16, 1.
44. Z. Jian, W. Han, X. Lu, H. Yang, Y.-S. Hu, J. Zhou, Z. Zhou, J. Li, W. Chen, D. Chen and L. Chen, *Adv. Energy Mater.*, 2013, 3, 156.
45. S.-M. Oh, S.-T. Myung, J. Hassoun, B. Scrosati and Y.-K. Sun, *Electrochem. Commun.*, 2012, 22, 149.
46. F. Sauvage, E. Quarez, J. M. Tarascon and E. Baudrin, *ChemInform.*, 2007, 38, no.
47. Barker.J, Gover.RKB, Burns.P and Bryan.A, *Electrochem. Solid-State Lett.*, 2006, 9, A190.
48. R. A. Shakoor, D.-H. Seo, H. Kim, Y.-U. Park, J. Kim, S.-W. Kim, H. Gwon, S. Lee and K. Kang, *J. Mater. Chem.*, 2012, 22, 20535.
49. Y. Lu, L. Wang, J. Cheng and J. B. Goodenough, *Chem. Commun.*, 2012, 48,

- 6544.
50. M. Nishijima, I. D. Gocheva, S. Okada, T. Doi, J.-i. Yamaki and T. Nishida, *J. Power Sources*, 2009, 190, 558.
 51. Y. Yamada, T. Doi, I. Tanaka, S. Okada and J.-i. Yamaki, *J. Power Sources*, 2011, 196, 4837.
 52. B. Genorio, K. Pirnat, R. Cerc-Korosec, R. Dominko and M. Gaberscek, *Angew. Chem. Int. Ed.*, 2010, 49, 7222.
 53. R. Zhao, L. Zhu, Y. Cao, X. Ai and H. X. Yang, *Electrochem. Commun.*, 2012, 21, 36.
 54. K. Sakaushi, E. Hosono, G. Nickerl, T. Gemming, H. Zhou, S. Kaskel and J. Eckert, *Nat. Commun.*, 2013, 4, 1485.
 55. D. A. Stevens and J. R. Dahn, *J. Electrochem. Soc.*, 2000, 147, 1271.
 56. R. Alcántara, J. M. Jiménez-Mateos, P. Lavela and J. L. Tirado, *Electrochem. Commun.*, 2001, 3, 639.
 57. S. Wenzel, T. Hara, J. Janek and P. Adelhelm, *Energy Environ. Sci.*, 2011, 4, 3342.
 58. Y. Cao, L. Xiao, M. L. Sushko, W. Wang, B. Schwenzer, J. Xiao, Z. Nie, L. V. Saraf, Z. Yang and J. Liu, *Nano Lett.*, 2012.
 59. S. Komaba, W. Murata, T. Ishikawa, N. Yabuuchi, T. Ozeki, T. Nakayama, A. Ogata, K. Gotoh and K. Fujiwara, *Adv. Funct. Mater.*, 2011, 21, 3859.
 60. S. I. Park, I. Gocheva, S. Okada and J.-i. Yamaki, *J. Electrochem. Soc.*, 2011, 158, A1067.
 61. K. Gotoh, T. Ishikawa, S. Shimadzu, N. Yabuuchi, S. Komaba, K. Takeda, A. Goto, K. Deguchi, S. Ohki, K. Hashi, T. Shimizu and H. Ishida, *J. Power Sources*, 2013, 225, 137.
 62. L. Wu, F. Pei, R. Mao, F. Wu, Y. Wu, J. Qian, Y. Cao, X. Ai and H. Yang, *Electrochim. Acta*, 2013, 87, 41.
 63. J. Qian, Y. Chen, L. Wu, Y. Cao, X. Ai and H. Yang, *Chem. Commun.*, 2012, 48, 7070.

-
64. L. Xiao, Y. Cao, J. Xiao, W. Wang, L. Kovarik, Z. Nie and J. Liu, *Chem. Commun.*, 2012, 48, 3321.
65. M. K. Datta, R. Epur, P. Saha, K. Kadakia, S. K. Park and P. N. Kumta, *J. Power Sources*, 2013, 225, 316.
66. H. Zhu, Z. Jia, Y. Chen, N. Weadock, J. Wan, O. Vaaland, X. Han, T. Li and L. Hu, *Nano Lett.*, 2013, 13, 3093.
67. L. Baggetto, J. K. Keum, J. F. Browning and G. M. Veith, *Electrochem. Commun.*, 2013, 34, 41.
68. J. Qian, X. Wu, Y. Cao, X. Ai and H. Yang, *Angew. Chem. Int. Ed.*, 2013, 52, 4633.
69. S. Komaba, Y. Matsuura, T. Ishikawa, N. Yabuuchi, W. Murata and S. Kuze, *Electrochem. Commun.*, 2012, 21, 65.
70. V. L. Chevrier and G. Ceder, *J. Chem. Soc.*, 2011, 158, A1011.
71. P. Senguttuvan, G. Rousse, V. Seznec, J.-M. Tarascon and M. R. Palacín, *Chem. Mater.*, 2011, 23, 4109.
72. L. Zhao, H.-L. Pan, Y.-S. Hu, H. Li and L.-Q. Chen, *Ch. Phys. B*, 2012, 21, 028201.
73. Y. Wang, X. Yu, S. Xu, J. Bai, R. Xiao, Y.-S. Hu, H. Li, X.-Q. Yang, L. Chen and X. Huang, *Nat. Commun.*, 2013, 4, 2365.
74. B. Koo, S. Chattopadhyay, T. Shibata, V. B. Prakapenka, C. S. Johnson, T. Rajh and E. V. Shevchenko, *Chem. Mater.*, 2012, 25, 245.
75. S. Komaba, T. Mikumo and A. Ogata, *Electrochem. Commun.*, 2008, 10, 1276.
76. Z. Jian, B. Zhao, P. Liu, F. Li, M. Zheng, M. Chen, Y. Shi and H. Zhou, *Chem. Commun.*, 2014, 50, 1215.
77. L. David, R. Bhandavat and G. Singh, *ACS Nano*, 2014, 8, 1759.
78. B. Qu, C. Ma, G. Ji, C. Xu, J. Xu, Y. S. Meng, T. Wang and J. Y. Lee, *Adv. Mater.*, 2014, 3854.
79. J. Fullenwarth, A. Darwiche, A. Soares, B. Donnadiou and L. Monconduit, *J.*

-
- Mater. Chem. A*, 2014, 2, 2050.
80. J. Qian, Y. Xiong, Y. Cao, X. Ai and H. Yang, *Nano Lett.*, 2014, 14, 1865.
 81. L. Zhao, J. Zhao, Y.-S. Hu, H. Li, Z. Zhou, M. Armand and L. Chen, *Adv. Energy Mater.*, 2012, 2, 962.
 82. K. Chihara, N. Chujo, A. Kitajou and S. Okada, *Electrochim. Acta*, 2013, 110, 240.
 83. C. Vidal-Abarca, P. Lavela, J. L. Tirado, A. V. Chadwick, M. Alfredsson and E. Kelder, *J. Power Sources*, 2012, 197, 314.
 84. A. Ponrouch, E. Marchante, M. Courty, J.-M. Tarascon and M. R. Palacin, *Energy Environ. Sci.*, 2012, 5, 8572.
 85. S. Komaba, T. Ishikawa, N. Yabuuchi, W. Murata, A. Ito and Y. Ohsawa, *ACS Appl. Mater. Interf.*, 2011, 3, 4165.
 86. Y. Kim, Y. Kim, A. Choi, S. Woo, D. Mok, N.-S. Choi, Y. S. Jung, J. H. Ryu, S. M. Oh and K. T. Lee, *Adv. Mater.*, 2014, 4139.
 87. R. Marchand, F. Tessier and F. J. DiSalvo, *J. Mater. Chem.*, 1999, 9, 297.
 88. J. S. J. Hargreaves and D. Mckay, *Catal.*, 2006, 19, 84.
 89. D. H. Gregory, *J. Chem. Soc., Dalton Trans.*, 1999, 259.
 90. R. Niewa and F. J. Di Salvo, *Chem. Mater.*, 1998, 10, 2733.
 91. R. J. Xie and N. Hirosaki, *Sci. Technol. Adv. Mater.*, 2007, 8, 588.
 92. R. L. Riley, *J. Am. Ceram. Soc.*, 2000, 83, 245.
 93. A. J. Steckl and R. Birkhahn, *Appl. Phys. Lett.*, 1998, 73, 1700.
 94. A. A. Andreev, *Phys. Solid State*, 2003, 45, 419.
 95. K. P. O. Donnell and B. Hourahine, *Eur. Phys. J. Apply. Phys.*, 2006, 36, 91.
 96. R. Kojima and K.-i. Aika, *appl. Catal. A: Gen.*, 2001, 219, 157.
 97. B. Mazumder and A. Hector, *Top. Catal.*, 2009, 52, 1472.
 98. S. Vepřek and S. Reiprich, *Thin Solid Films*, 1995, 268, 64.

-
99. R. Buhl, H. K. Pulker and E. Moll, *Thin Solid Films*, 1981, 80, 265.
 100. J. E. Sundgren, *Thin Solid Films*, 1985, 128, 21.
 101. S. T. Oyama, *Catal. Today*, 1992, 15, 179.
 102. M. Boudart, S. T. Oyama and L. Leclecq, *Proc. 7th Int. Cong. Catal., Tokyo 1980, T. Seiyama and K. Tanabe (Eds.), Vol. 1, p. 587, Kodansha, 1980.*
 103. S. T. Oyama, *J. Catal.*, 1992, 133, 358.
 104. M. R. Hillis, C. Kemball and M. W. Roberts, *Trans. Faraday Soc.*, 1966, 62, 3570.
 105. R. Komija and K. I. Aika, *appl. Catal. A: Gen.*, 2001, 215, 149.
 106. M. K. Neylon, S. Choi, H. Kwon, K. E. Curry and L. T. Thompson, *appl. Catal. A: Gen.*, 1999, 183, 253.
 107. S. K. Bej and L. T. Thompson, *appl. Catal. A: Gen.*, 2004, 264, 141.
 108. S. Kaskel, K. Schlichte and T. Kratzke, *J. Mol. Catal. A: Chem.*, 2004, 208, 291.
 109. C. M. Fang, E. Orhan, G. A. de-Wijs, H. T. Hintzen, R. A. de-Groot, R. Marchand, J.-Y. Saillard and G. de-With, *J. Mater. Chem.*, 2001, 11, 1248.
 110. C. G. Granqvist, *Adv. Mater.*, 2003, 15, 1789.
 111. Q. Zhang and L. Gao, *Langmuir*, 2004, 20, 9821.
 112. B. Fu, L. Gao and S. Yang, *J. Am. Ceram. Soc.*, 2007, 90, 1309.
 113. J. Li, D. Dzinvenko, A. Zerr, C. Fasel, Y. Zhou and R. Riedel, *Z. Anorg. Allg. Chem.*, 2005, 631, 1449.
 114. C. M. Ghimbeu, E. Raymundo-Pinero, P. Fioux, F. Beguin and C. Vix-Guterl, *J. Mater. Chem.*, 2011, 21, 13268.
 115. Y. T. Kim, K. Tadai and T. Mitani, *J. Mater. Chem.*, 2005, 15, 4914.
 116. J. P. Zheng and T. R. Jow, *J. Electrochem. Soc.*, 1995, 142, L6.
 117. Y. U. Jeong and A. Manthiram, *J. Electrochem. Soc.*, 2002, 149, A1419.
 118. H. Liang, F. Chen, R. Li, L. Wang and Z. Deng, *Electrochim. Acta*, 2004, 49, 3463.

-
119. C.-C. Hu, W.-C. Chen and K.-H. Chang, *J. Electrochem. Soc.*, 2004, 151, A281.
 120. J. P. Zheng, *Electrochem. Solid State*, 1999, 2, 359.
 121. D. Choi, G. E. Blomgren and P. N. Kumta, *Adv. Mater.*, 2006, 18, 1178.
 122. D. Choi and P. N. Kumta, *J. Electrochem. Soc.*, 2006, 153, A2298.
 123. C. Chen, D. Zhao, D. Xu and X. Wang, *Mater. Chem. Phys.*, 2006, 95, 84.
 124. P. Poizot, S. Laruelle, S. Grugeon, L. Dupont and J. M. Tarascon, *Nature*, 2000, 407, 496.
 125. B. Das, M. V. Reddy, P. Malar, T. Osipowicz, G. V. Subba Rao and B. V. R. Chowdari, *Solid State Ionics*, 2009, 180, 1061.
 126. Y. Wang, W. Y. Liu and Z. W. Fu, *Acta. Phys. Chim. Sin.*, 2006, 22, 65.
 127. Y. Wang, Z.-W. Fu, X.-L. Yue and Q.-Z. Qin, *J. Electrochem. Soc.*, 2004, 151, E162.
 128. Q. Sun and Z.-W. Fu, *Electrochim. Acta*, 2008, 54, 403.
 129. Q. Sun and Z.-W. Fu, *Electrochem. Solid-State Lett.*, 2007, 10, A189.
 130. J. Cabana, L. Monconduit, D. Larcher and M. R. Palacín, *Adv. Mater.*, 2010, 22, E170.
 131. J. Ma, L. Yu and Z.-W. Fu, *Electrochim. Acta*, 2006, 51, 4802.
 132. N. Pereira, L. Dupont, J. M. Tarascon, L. C. Klein and G. G. Amatucci, *J. Electrochem. Soc.*, 2003, 150, A1273.
 133. N. Suzuki, R. B. Cervera, T. Ohnishi and K. Takada, *J. Power Sources*, 2013, 231, 186.
 134. R. C. de Guzman, J. Yang, M. Ming-Cheng Cheng, S. O. Salley and K. Y. S. Ng, *J. Mater. Chem. A*, 2014, 2, 14577.
 135. L. Baggetto, N. A. M. Verhaegh, R. A. H. Niessen, F. Roozeboom, J.-C. Jumas and P. H. L. Notten, *J. Electrochem. Soc.*, 2010, 157, A340.

Chapter 2. Experimental techniques

2.1 Powder X-Ray Diffraction (PXD)

The phenomenon of X-ray diffraction by crystals was discovered in 1912, and in the same year, the first collection of X-ray diffraction patterns of a copper sulphate penta-hydrate crystal was accomplished by Friedrich and Knipping.¹ From then on, this technique was widely used in identification of chemical composition and crystallographic structure of natural and manufactured materials.

X-rays are generated when high-speed electrons are incident with the orbital electrons of a metal target. Therefore any X-ray tube must contain a source of electrons (cathode), a high accelerating voltage and a metal target (anode). Specifically, the electrons are generated from a tungsten filament (cathode) and accelerated towards to the pure metal target (anode), then knocking an electron in the metal atom out of its orbital, thus leaving a hole. This hole can then be filled by another electron in the atom, giving off X-ray radiation in the transition to conserve energy. The theoretical diagram is shown in Figure 2.1.

A crystal monochromator is used to provide a single X-ray wavelength for diffraction experiments, and is placed in series between the radiation source and the sample. This crystal monochromator is mounted in the correct orientation to diffract only X-ray photons of the desired wavelength. The monochromated beam is collimated by aperture slits before striking the sample.

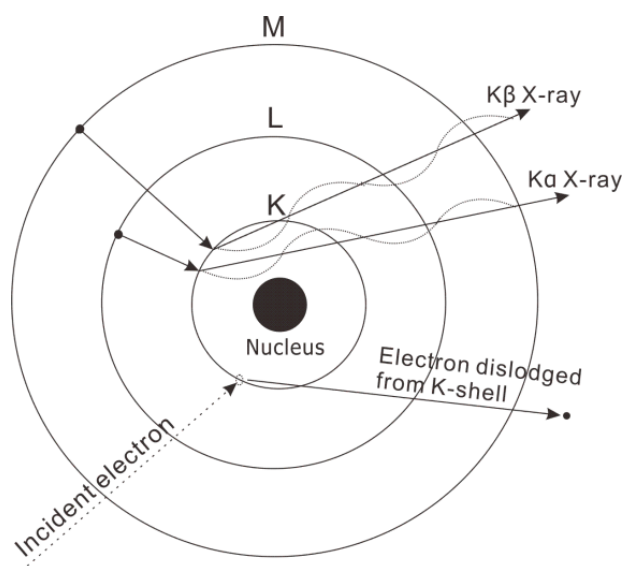


Figure 2.1 Theoretical diagram of the generation of X-rays

The diffraction can be seen as the scattering of the X-rays by the ordered environment in a crystal.² The periodic lattice found in the crystalline structures act as diffraction grating for X-rays, due to their similar order of magnitude between d-spacing and wavelength (10^{-10} m/ 1 Å). Diffraction occurs when X-rays pass through a crystal with incident of parallel planes in accordance with the Bragg's Law, which is:

$$n\lambda = 2d\sin\theta \quad \text{Equation 2.1}$$

where n is an integer (1, 2, 3, ..); λ is the X-ray wavelength; θ is the angle of incidence (Bragg angle); d is the inter-planar separation in the crystalline material.

If X-ray photons strike the crystal with an incidence angle of θ and are scattered by atoms lying on the planes separated by a distance d , the extra distance travelled by the X-ray photons scattered by the lower plane in Fig 2.2 is $2d\sin\theta$. The inter-planar separation distance d can be calculated via measuring the diffraction maxima when $2d\sin\theta$ equals $1\lambda, 2\lambda, 3\lambda \dots n\lambda$.

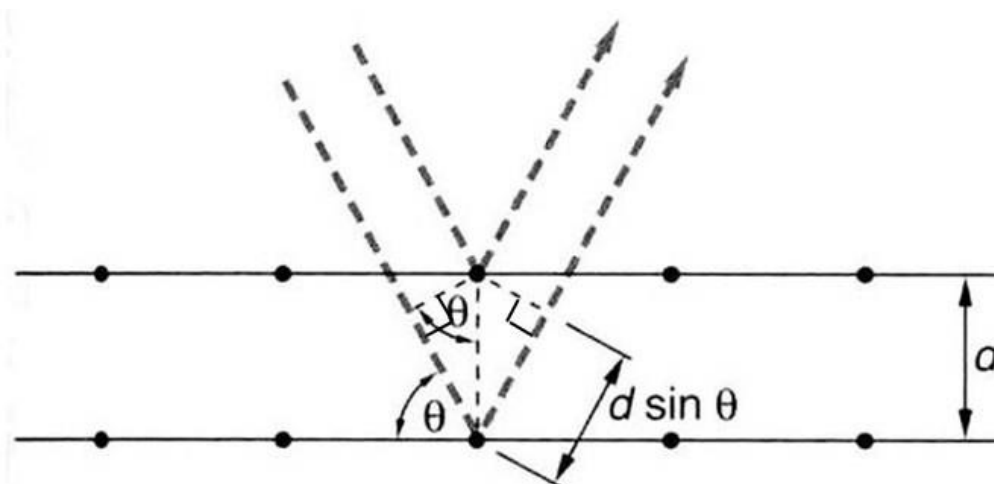


Figure 2.2 Schematic diagram of X-ray diffraction

The PXD data collection for this project was conducted with a Siemens D5000 diffractometer or a Bruker D2 Phaser. Both instruments have similar set up. Take Siemens D5000 as an example, the X-rays for diffraction experiments were generated by bombarding a copper target with a beam of electrons emitted from a heated filament with a wavelength of 1.5406 \AA , $\text{Cu K}_{\alpha 1}$ (1.5418 \AA , Cu K_{α} , D2 Phaser). The PXD sample was grounded to a fine powder to provide an enormous number of small, randomly orientated crystallites. X-ray beams are diffracted by thousands of crystallites resulting in the diffraction signal being observed as cones, which are collected by a scintillation detector (one dimensional detector, D2 Phaser) scanning through different positions. Figure 2.3 shows the schematic diagram of a typical diffractometer. The collected data were analysed by using the Bruker Diffract Evaluation program (Eva).

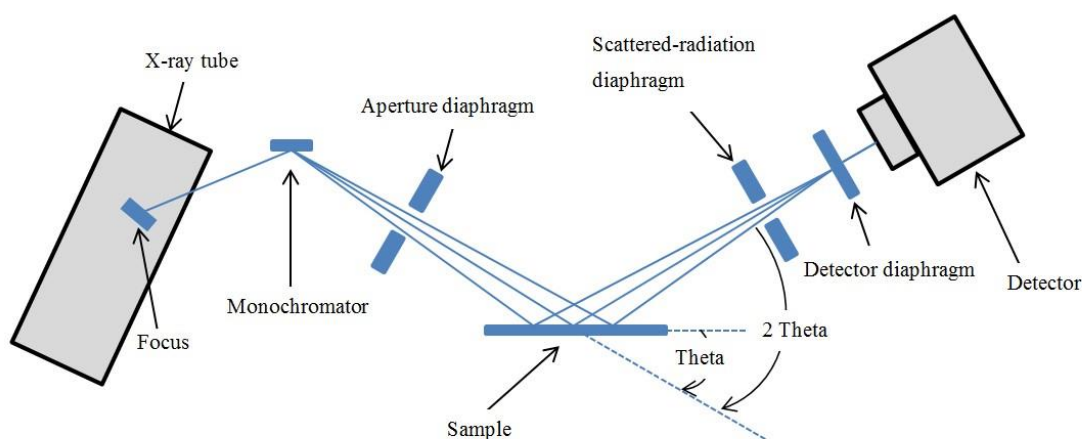


Figure 2.3 The schematic diagram of X-ray diffractometers

2.2 *Ex situ* X-ray Diffraction

To understand the mechanism of charge storage, *ex situ* XRD was employed. As the electrode reactions were assembled as a thin layer at composite on a metal foil, the samples were treated as thin films. Powder X-ray diffraction technique, which is a symmetric measurement, is less suitable for this *ex situ* XRD requirement since the X-ray path lengths are quite short in this geometry. Hence, a grazing incidence geometry, which is widely used for characterising thin film, was adopted. In this measurement, the incident X-ray beam is kept at a small angle (usually several degrees or less) with respect to the electrode surface. In the meantime, the detector is scanned across a range of 2θ angles to record diffraction intensities. The specific diffraction geometry is shown in Figure 2.4. The travelling path of the X-ray photo through the film can be maximised in this situation, and the path length (L) is determined by the layer thickness (D) and incidence angle (θ), $L=D/\sin \theta$. A small incident angle can contribute to the total external reflection from the surface. And thus optimal grazing incidence X-ray diffraction measurements are performed around the critical angle, which is the incident angle below which total

external reflection occurs. This critical angle is determined by the X-ray wavelength and the density of the matter.³ Grazing incidence X-ray diffraction can improve the scattering contribution sensitivity from the film (layer) and reduce the observed substrate scattering.⁴ Hence, in *ex situ* XRD, any phase change in the active material can be clearly observed.

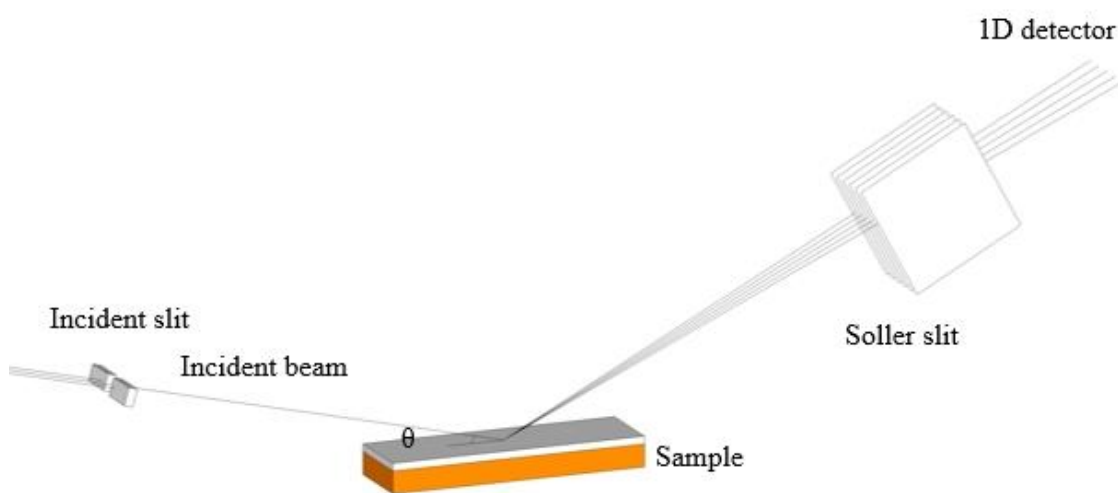


Figure 2.4 Schematic representation of grazing incidence X-ray diffraction measurement.

Most *ex situ* XRD results were collected with the thin film (Rigaku Smartlab) X-ray diffractometer specified for. The optical device used is medium resolution parallel beam (PB) with a 0.1 mm incident slit and a 5 mm line delivered to the sample surface. The optics used were 5° incident and receiving Soller slits, and the one-dimensional detector (1D). The typical incident angle was 1°, which can maximally get an external reflection. The patterns were collected in the 2θ range of 20-80°.

2.3 Rietveld Refinement

Structural analysis was mostly conducted using the General Structure Analysis Suite

(GSAS⁵). The Rietveld refinement method was proposed by Hugo M. Rietveld in 1967.⁶ This method is utilized to refine the structure of crystalline materials by powder diffraction. The drawback of PXD is the overlapping of diffraction peaks. In order to solve this problem, H.M. Rietveld realised that although many reflections did overlap and thus could be modelled as single entities, the total intensity and the peak shape of a cluster of reflections could be determined by using a simple peak shape parameter.^{6,7}

The aim of the refinement is to minimize the difference between the collected PXD data and the calculated data from the model by changing different parameters. Specifically, the scale factor was refined followed by the lattice parameters, zero point, background and Lorentzian peaks in profile. Note that Gaussian peaks were kept at values obtained by refining a silica standard to define an instrumental shape. Finally, atom positions and the thermal motions of atoms (isotropic temperature factors) were refined.

From the refined PXD pattern, the particle size can be estimated. Information on particle size can be extrapolated from the complex expressions derived to model the Gaussian and Lorentzian components of the peak shape.⁵ For PXD the particle size broadening can be obtained from the expression:

$$\frac{\Delta d}{d^2} = \frac{\Delta 2\theta \cot\theta}{d} = \text{constant} \quad \text{Equation 2.2}$$

Combining with Bragg's law, it becomes:

$$\frac{\Delta d}{d^2} = \frac{\Delta 2\theta \cot\theta \sin\theta}{\lambda} \quad \text{Equation 2.3}$$

The broadening is then,

$$\Delta 2\theta = \frac{\lambda \Delta d/d}{2 \cos\theta} \quad \text{Equation 2.4}$$

For PXD the Lorentzian coefficient, γ , of the peak shape is affected by two parameters, X and Y (denoted LX and LY in the GSAS program) in the expression⁷:

$$\gamma = \frac{X + X_s \cos\phi}{\cos\theta} + (Y + Y_s \cos\phi) \tan\theta \quad \text{Equation 2.5}$$

Where X_s and Y_s are anisotropic coefficients.

The first term in the expression for the Lorentzian broadening, X, can be expressed as:

$$X = \frac{\Delta d}{d^2} \quad \text{Equation 2.6}$$

Hence, the particle size, p, can be obtained by rearranging this expression and converting from degree to radians:

$$p = \frac{18000K\lambda}{\pi X} \quad \text{Equation 2.7}$$

where K is the Scherrer constant, λ is the X-ray wavelength (1.5406 Å) and X is the value of the L_x Lorentzian component which can be extracted from the GSAS refinement.

2.4 Thermogravimetric Analysis

Thermogravimetric analysis (TGA) is a thermal analysis technique used to test changes in the weight of a sample in relation to the temperature and/or time under controlled atmosphere, thereby measuring the thermal stability and the compositions of materials.

TGA was performed using a Mettler Toledo TGA/SDTA851 shown in Figure 2.5.

Pre-programmed heating regimes were selected for the TGA samples heated under a flow of argon gas. The sample (between 10–30 mg) was loaded in a dry alumina crucible (Vol: 150 μ L) and then placed onto the balance arm within the analyser. It was held at 25 °C for 10

minutes before gradually heating to 800 °C at a heating rate of 10 °C/min under a flow of gas (50 mL/min) for the whole procedure. At 800 °C the sample was then held for 20 or 60 minutes before allowing it to cool back to 25 °C. The balance assembly measured the initial sample mass and then continuously monitored any change in mass as a function of temperature and time throughout the procedure.

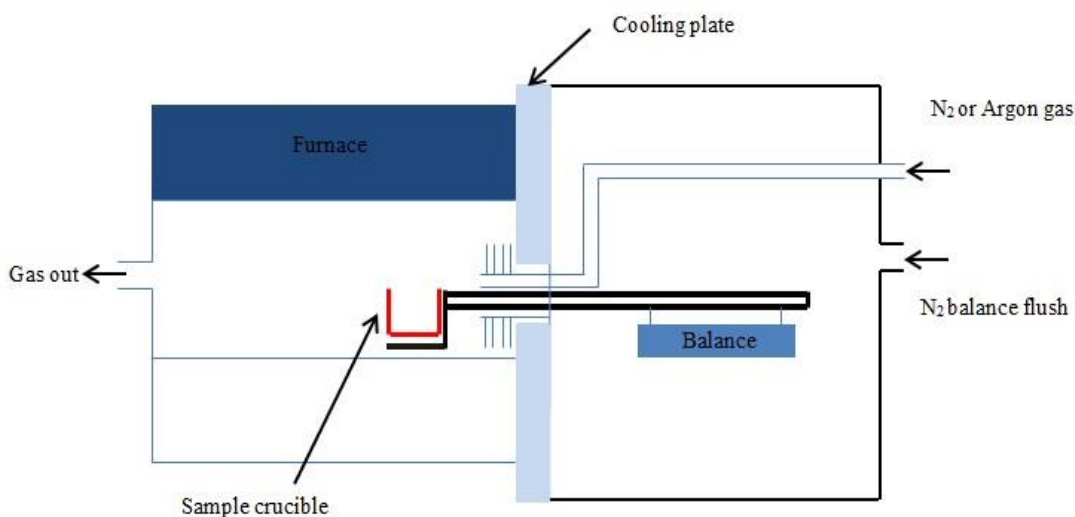


Figure 2.5 Schematic diagram of the Mettler Toledo TGA851.

2.5 Infrared spectroscopy

Infrared spectroscopy is a common technique to identify the chemical bonds (functional groups) within molecules. IR spectroscopy involves collecting absorption information and analysing it in the form of a spectrum. For a molecule to adsorb IR, the vibrations or rotations within a molecule must cause a net change in the dipole of the molecule. The absorption of IR radiation depends on increasing the energy of vibration or rotation associated with a covalent bond. This increase results in a change in the dipole moment of the molecule or solid.

IR experiments are typically based on passing IR radiation through a thin sample of compound and measuring which energies of the applied IR radiation are transmitted by the sample. IR spectra can be recorded for solids, liquids and gases using different sample arrangements. The absorption by a specific group occurs in a characteristic region of the spectrum. These absorptions appear as a series of peaks and are referenced by simply comparing them with tables of known compounds.⁸ Similar frequencies occur in different molecules, therefore a vibration is considered as reflecting the atoms involved and the strength of bond holding them together.

Solid samples were prepared by mixing them with a pressed pellet of potassium bromide for analysis. Due to the sensitivity of the precursor, the samples had to be prepared inside a nitrogen filled glove box. A weighed portion of sample, approximately 0.2 mg, was mixed with 20 mg, of highly purified KBr using a pestle and mortar. The sample and KBr were ground well to reduce the particle size; otherwise the large particles would scatter the infrared beam causing a sloping profile in the baseline of the spectrum. KBr does not absorb in the region studied so will not interfere with the spectrum. The mixture was placed in an evacuable die and subjected to a pressure of 10 MPa for two minutes. The infrared spectra were collected from 4000 cm^{-1} to 400 cm^{-1} using a PerkinElmer spectrum 100 FT-IR spectrometer in conjunction with PerkinElmer's analytical software v3.05.

2.6 Microanalysis

Combustion microanalysis was used to identify the quantities of carbon, hydrogen, nitrogen in samples. This information can be used as a guide to sample stoichiometry compared to calculated percentage composition based on ideal materials. Around 5–15

mg of sample was sent to MEDAC Ltd., Egham, Surrey, who handled samples in the glove box. The sample and its container was melted (flash combustion) in a temporary enriched oxygen atmosphere. Quantitative combustion was then achieved by passing the mixture of gases to the chromatographic column where the individual components were separated. Normally, the addition of WO_3 oxidant and the use of tin capsules were requested to obtain best results, as in previous work within the group the higher temperature and more strongly oxidising conditions were found to aid nitrogen recovery.

2.7 Brunauer-Emmett-Teller (BET) method

An inverse relation is found between the specific surface area and particle size of materials, as the particle size decreases, the specific surface area increases. BET (Brunauer, Emmet and Teller) gas adsorption theory was first described and used by Brunauer *at al.* in 1938.⁹ BET is a gas adsorption method based on the isotherms derived from adsorption of multilayers of gas atoms/molecules on the surface of the solid. The equation to determine the specific surface area is shown in equation 2.8.

$$\frac{p}{v(p_0 - p)} = \frac{1}{v_m c} + \frac{c - 1p}{v_m c p_0} \quad \text{Equation 2.8}$$

Where v is the volume adsorbed, p and p_0 are the sample pressure and saturation pressure respectively, v_m is the volume of the monolayer and c is a constant.

The BET surface area is determined by using the following equation,

$$S_{BET} = \frac{v_m \cdot N_A \cdot a_m}{m_V} \quad \text{Equation 2.9}$$

Where N_A is the Avogadro number, a_m is the molecular area of an adsorbed N_2 molecule (16.2 Å) and m_V is the molar volume (22.414 ml) of N_2 (l) at 77 K.

In this work, a Gemini 2375 Surface Area Analyser was employed to collect and analyse nitrogen absorption data.

2.8 Transmission Electron Microscopy

Transmission Electron Microscopy is a microscopy technique whereby a beam of electrons is transmitted through an ultra-thin specimen, interacting with the specimen as it passes through. An image is formed from the interaction of the electrons transmitted through the specimen; the image is magnified and focused onto an imaging device, such as a charge-coupled device (CCD) camera.

The main parts of a TEM are assembled into a vertical column. At the top of the instrument is the electron gun¹⁰. TEM usually uses thermionic guns capable of accelerating the electrons in the range 40-300 KV. The right electron energy depends upon the nature of the specimen and the information required. The use of higher electron energies represents an advantage in case of thick samples or high resolution requirements. The illumination provided by an electron gun is focussed onto the specimen by two condenser lenses (Figure 2.6). One of the most important parts of the microscope is the specimen chamber which is placed below the second condenser lens C2. The specimen rod enters the column through an airlock, and can usually be moved in the x, y and z directions to find the region of interest.

TEM was carried out using on Hitachi H7000 with accelerating voltage of 75 kV at the Biomedical Imaging Unit, Southampton General Hospital. Samples were prepared by ultrasound dispersal using dry methanol as the solvent and were deposited on carbon coated Cu grids. The technique was used to obtain images of the morphology of the nanostructured particles and approximate particle sizes.

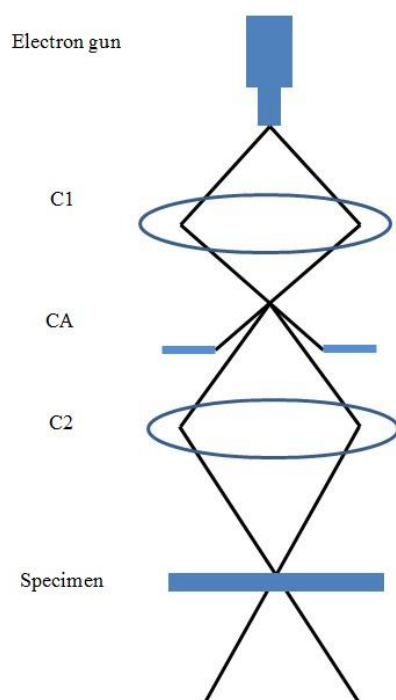


Figure 2.6 Main components of a transmission electron microscope. (C1 and C2 are the condenser lens while CA is the condenser aperture).

2.9 The electrochemical techniques

2.9.1 Cyclic voltammetry

Cyclic voltammetry (CV) is a type of potentiodynamic electrochemical measurement and has been widely used to investigate the electrochemical performance of lithium-ion

batteries.¹¹ Combining qualitative analysis of CV results, in terms of the number and shape of the peaks and their difference between first and subsequent cycles, with quantitative analysis of the current densities, can provide an important insight into reactions occurring in the cell and corresponding electrode processes. In a CV experiment, the working electrode potential is ramped linearly versus time. This ramping is known as the experiment's scan rate (mV s^{-1}). Potential can be scanned in a positive direction to study oxidation reactions, or alternatively, in a negative direction to study reduction processes. The collected data were plotted as current *vs.* potential. In this work, the lithium/ sodium foil was treated as counter as well as reference electrode.

2.9.2 Galvanostatic method

The galvanostatic method is a control and measuring device capable to keep constant the current flowing through an electrolytic cell in Coulometric titrations¹², regardless of changes in the load itself. In the simplest case, a galvanostat would consist of a high-voltage source generating a constant voltage V with a resistor R_x connected in series. In order to force the flow of an approximate constant current through a load, this resistor, R_x , should be much higher than the load resistor R_{load} . The current, I , flowing through the load is given by

$$I = V / (R_x + R_{\text{load}}) \quad \text{Equation 2.10}$$

Where the current I is approximately determined by R_x because

$$I = V / R_x \text{ if } R_x \gg R_{\text{load}} \quad \text{Equation 2.11}$$

The galvanostatic method is the main electrochemical method applied to determine performance of electrode materials in this project. Current was controlled and potential measured using Biologic SP150 or MPG potentiostat. A constant current can be applied to the cell at different ‘C rates’, with upper and lower potential limits. As a negative current is applied to the working electrode, lithium or sodium ions are inserted into the material and the cell potential decreases. When a positive current is applied to the working electrode, the opposite process, in which lithium or sodium ions are extracted from the materials, occurs.

The rate of reduction and oxidation is referred to as ‘C rate’ and corresponds to the applied current in the cell in relation to the theoretical specific capacity of the material being studied. A charge/discharge rate of 1 C corresponds to completely reducing and oxidising the working electrode material in one hour whereas at 2 C, the process would take 1/2 hour. To calculate the applied current, the following equation 2.11 was used to find the capacity of the active material in the electrode pellet.

$$Q_A = m_A \times Q_T \qquad \text{Equation 2.12}$$

Where:

Q_T = Theoretical capacity of the active material (mA h g^{-1})

m_A = Mass of the active material in the electrode (g)

Q_A = Capacity of the active material in the electrode (mA h)

2.9.3 Electrode preparation and cell construction

Deposition from an ink was mostly adopted as the electrode fabrication method in this project. The working electrode material consisted of 75% powdered active material, 20% acetylene black and 5% binder. In general, the binder was dissolved into a solvent (cyclopentanone or deionized water) with stirring. And then the active material and acetylene black well grinded mixture was added. The ink was constantly stirred to form a uniform mixture of active material, acetylene black and binder. The ink was then dropped onto a 50 μm thick foil disc substrate (Cu or Ti) with 10 mm in diameter. After drying *in vacuo* the amount of active material was determined by mass difference. The electrode fabrication varied in different cases, which was discussed with details in later chapters

The typical cell used for electrochemistry tests is Swagelok type cell in Figure 2.7.

Specifically, the active material pellet/ electrode (10) was attached to the current collect (1) on the right followed by two pieces of glass fibre separator (GF/F grade, *Whatman*) (9) soaked with 6-7 electrolyte drops. On the other side of the separator, lithium or sodium metal foil was attached as counter and reference electrode. Glass fibre filters were chosen for the separator, as they have excellent porosity, while increasing the safe gap between the working electrode (active materials) and counter electrode (lithium or sodium foil), reducing the risk of shortcut in the cell.

The sodium cells were assembled under inert conditions inside a nitrogen filled glovebox (*MBraun*), while the lithium cells were set up inside an argon filled glovebox, as lithium can react with nitrogen to form lithium nitride. In the Swagelok cell, the electrode stack is assembled in the hollow perfluoroalkoxy (PFA) connector (7), and

two stainless steel plungers (1) force the stack together. The piston and spring (5, 6) provide stack pressure, which improves the contact between the cell components and the current collector. Once the plungers are in place, the PFA nuts (2) are tightened using a spanner. This forces the ferrules (3, 4) to grip the plunger, and effectively seals the cell from the atmosphere.

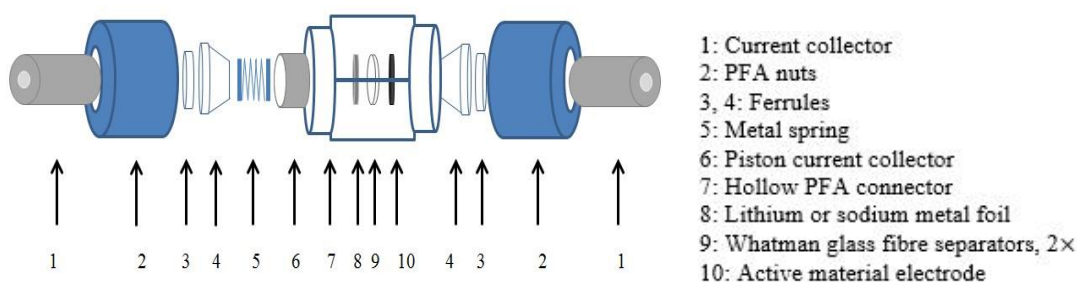


Figure 2.7 Schematic diagram of a Swagelok type cell.

2.10 Reference

1. B. D. Cullity, ed., *Elements Of X Ray Diffraction*, Addison-Wesley Publishing Company, Inc., 1956.
2. M. E. Malainey, ed., *A consumer's guide to archaeological science: analytical techniques*, Springer, 2010.
3. P. Dutta, *Curr. Sci.*, 2000, 78, 1478.
4. M. Birkholz, *Thin film analysis by X-ray scattering*, Wiley, Weinheim, 2006.
5. A. C. Larson and R. B. V. Dreele, GSAS manual, LANSCE MS-H805, Los Alamos National Laboratory, Los Alamos NM, NM 87545, 2000.
6. H. M. Rietveld, *Acta. Cryst.*, 1967, 22, 151.
7. H. M. Rietveld, *J. Appl. Cryst.*, 1969, 2, 65.
8. K. Nakamoto, *Infrared and Raman Spectra of Inorganic Compounds, Theory*

and Applications in Inorganic Chemistry, Wiley-Interscience, 1997.

9. S. Brunauer, P. H. Emmett and E. Teller, *J. Am. Chem. Soc.*, 1938, 60, 309.
10. P. J. Goodhew, J. H. Humphreys and R. Beanland, *Electron Microscopy and Analysis*, 3 edn., 2001.
11. A. J. Bard and L. R. Faulkner, *Electrochemical Methods: Fundamentals and Applications.*, Wiley, 2000., 2nd edn., 2000.
12. Y. C. Zhou and J. A. Switzer, *Mat. Res. Innovat.*, 1998, 2, 22.

Chapter 3. Nickel nitride as the negative electrode material for sodium-ion batteries

3.1 Introduction

Transition metal nitrides have been extensively studied for their particular properties and wide applications in catalysts and optoelectronic materials.¹⁻⁴ Various synthesis routes to nickel nitride have been studied. Nickel nitrides can be prepared by sputtering of nickel films in Ar/N₂ mixed gas, as well as through ion bombardment of nickel films using N⁺ ions.^{5,6} An intermediate Ni₄N phase can be formed during nitridation of Ni metal into Ni₃N and then transferred into Ni₃N stable phase. Also, nickel nitride can be obtained from rapid and exothermic solid-state metathesis (SSM) reactions, supercritical synthesis and laser-aided synthesis.⁷⁻¹² For example, Ni₃N could be obtained from Ni(NH₃)₆Br₂ by treatment under 50 cm³ min⁻¹ ammonia flow at 420 °C for 15 h.¹² Or, it can be synthesized by a reduction of Ni²⁺ with hydrazine at 340 °C in NH₃ flow.¹¹

Ni₃N is a metallic interstitial nitride, where nitrogen is bonded to metallic nickel with covalent bonds. The weak linkages between nitrogen and nickel result in thermal instability in Ni₃N.⁸ The thermal decomposition of Ni₃N has been reported to occur at relatively low temperatures of around 250 °C in hydrogen atmosphere and around 400 °C in ammonia or nitrogen atmosphere.¹³ It is also reported the Ni₃N reduced to Ni at 290 °C in Ar/H₂ atmosphere.¹⁴ Hence, it is essential to control the maximum temperature during synthesis to avoid the decomposition of nickel nitride.

Nickel nitride has been examined for several applications.¹⁴⁻¹⁸ Ni₃N/Al and Ni₃N/Si nanocomposite films have shown great enhancements in hardness when bombarded with ion beam irradiation.¹⁶ Ni₃N/AlN nanocomposite films have also presented a medium efficiency on magnetic data storage tests.¹⁷ Wang *et al.* have studied the electrochemical interaction of Ni₃N with lithium.¹⁸ Most relevant to the aims of this project, Gillot *et al.* have conducted a comprehensive investigation of Ni₃N as a negative electrode in lithium-ion batteries. They found that nanosized Ni₃N prepared from decomposition of nickel amide achieved a specific capacity of 1200 mA h g⁻¹ in the first reduction reaction. But tough powdered electrodes exhibited poor reversibility and large capacity fading; performance was greatly improved when ‘cast’ binder containing electrodes were used, even at high cycling rates (500 mA h g⁻¹ reversible capacity maintained after 10 cycles at 1 C (theoretical capacity per hour)).¹⁴

In this work, nickel nitride was obtained from ammonolysis of nickel hexamine nitrate and nickel *tris*(ethylenediamine) nitrate salts. The electrochemical performance of nickel nitride as a negative electrode material in lithium- and sodium-ion batteries was then investigated.

3.2 Synthesis and characterization of nickel nitride

3.2.1 Nickel nitride derived from ammonolysis of nickel hexamine nitrate

Nickel (II) nitrate hexahydrate (4 g) was dissolved in deionised water (5 cm³) and 35% ammonia solution (10 cm³, Fisher) was added slowly with stirring, forming a bluish-violet solution. This solution was dried by evaporating under flowing ammonia and further dried in a desiccator over barium oxide (BaO) for three weeks. After

grinding, the precursor was heated under flowing ammonia at 335 °C for 6 h followed by 200 °C for 8 h. This route was proposed by combining the work of Gajbhiye *et al.*⁹ and Gillot *et al.*¹⁴ Gajbhiye *et al.* prepared Ni₃N by heating nickel hexamine nitrate from 340 °C to 420 °C for 4 to 12 hours under ammonia gas flow. In contrast, Gillot *et al.* found that nickel nitride can be synthesized from ammonolysis of nickel nanoparticles at a low temperature. As the weak linkages between nitrogen and nickel result in thermal instability in Ni₃N,⁸ nickel impurity can always be found in the products obtained from ammonolysis of nickel hexamine nitrate route. As a result, the two-stage heating route described was developed to convert the small amounts of Ni back to Ni₃N.

Rietveld refinement of the diffraction data (Figure 3.1) yielded lattice parameters of $a=4.6228(1)$ and $c=4.3067(1)$ Å, which are close to the reported values of $a=4.624(4)$ and $c=4.316(4)$ Å.¹⁹ Crystallite size was determined to be 83(2) nm from the Lorentzian components of the profile fit.²⁰

Table 3.1 Refined structure parameters of Ni₃N derived from [Ni(NH₃)₆](NO₃)₂.

Name	Fractional coordinates			Occupancy	Uiso
	x	y	z		
Ni	0.335838	0.000000	0.000000	1.0	0.00417
N	0.333300	0.666700	0.250000	1.0	0.13187

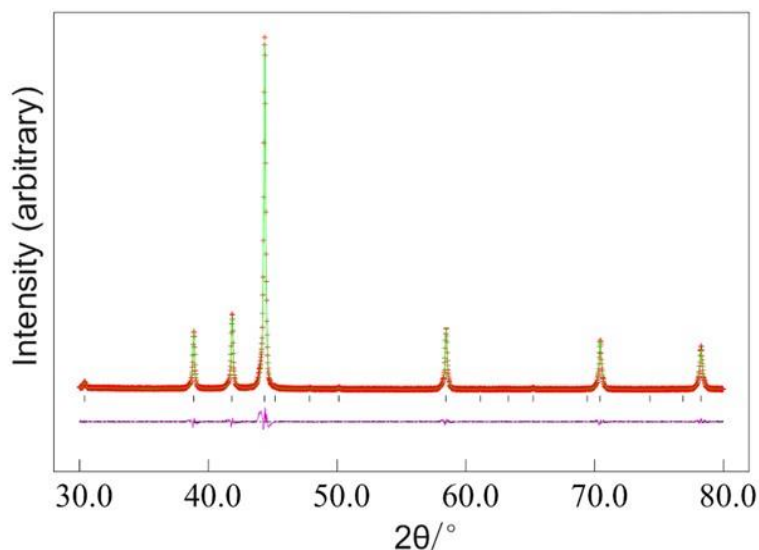


Figure 3.1 Rietveld fit ($R_{wp} = 12.0\%$, $R_p = 8.2\%$) to the PXD data for Ni₃N produced from ammonolysis of [Ni(NH₃)₆](NO₃)₂. Crosses mark the data points, the upper continuous line the fit and the lower continuous line the difference. Tick marks show the allowed positions of reflections for Ni₃N with space group P6₃22.²¹

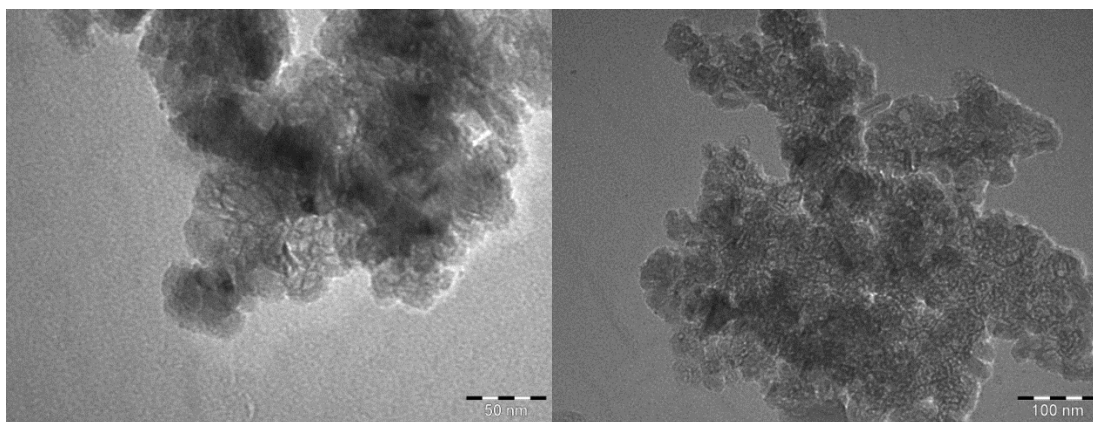


Figure 3.2 TEM pictures of nickel nitride synthesized from nickel hexamine nitrate

Thermogravimetric analysis (TGA) was conducted by heating nickel nitride sample from 25 °C to 800 °C with a ramp rate of 10 °C/min in nitrogen and the result is shown in Figure 3.3. The results show that the sample obtained from nickel hexamine nitrate loses approximately 7.8% of its mass in a single sharp mass loss just above 400 °C,

which is consistent with the result published by Baiker *et al.*¹³ Ni₃N contains 7.4% nitrogen in theory and hence this mass loss is consistent with the mass difference due to the decomposition of nickel nitride into nickel metal and nitrogen.

Elemental analysis shows that this material derived from ammonolysis of nickel hexamine nitrate contained (by mass) 7.3% nitrogen, 0.1% carbon and undetectable amounts of hydrogen (<0.1%), which is matched with the theoretically calculated nitrogen content (7.4%) and the result from TGA measurement above.

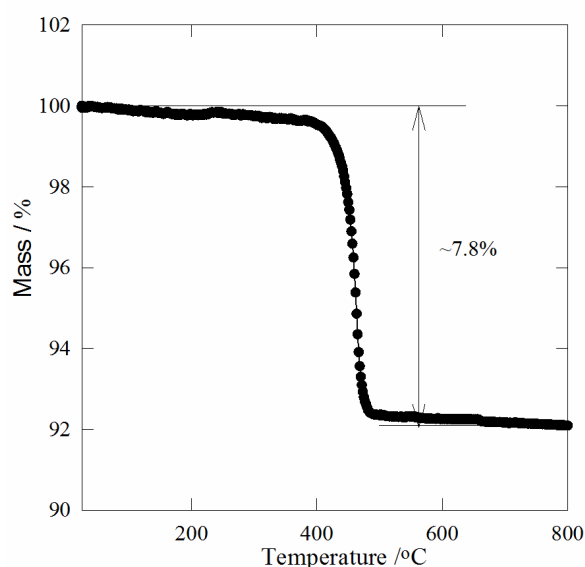


Figure 3.3 TGA trace of Ni₃N sample derived from ammonolysis of [Ni(NH₃)₆](NO₃)₂.

3.2.2 Nickel nitride derived from ammonolysis of nickel *tris*(ethylenediamine) nitrate

Nickel (II) nitrate hexahydrate (1 g, Aldrich) was dissolved in ethanol (10 cm³) with stirring and dried by removing the solvent *in vacuo* with gentle warming. The resulting yellow solid was dissolved in ethanol (5 cm³) and ethylenediamine (2 cm³, Aldrich,

99%) was added drop wise. Pink nickel *tris*(ethylenediamine) nitrate was recovered by removing solvent *in vacuo*. This solid was heated at 360 °C for 4 h then 200 °C for 40 h under flowing ammonia (BOC anhydrous grade, further dried by flowing over 3 Å molecular sieves).

Rietveld refinement of the PXD data graph shows Ni₃N with some Ni which obtained from ammonolysis of nickel *tris*(ethylenediamine) nitrate at 360 °C for 4 h then 200 °C for 40 h under flowing ammonia. Figure 3.4 shows broader peaks in the diffraction pattern than those observed in Figure 3.1, although these samples always contained a small quantity of nickel metal. The refined Ni₃N lattice parameters varied slightly more from literature values, with $a=4.5913(13)$ and $c=4.3251(13)$ Å, and the crystallite size is around 14(1) nm.

Table 3.2 Refined structure parameters of Ni₃N derived from [Ni(EDA)₆](NO₃)₂.

Name	Fractional coordinates			Occupancy	Uiso
	x	y	z		
Ni	0.333000	0.000000	0.000000	1.0	0.03395
N	0.333300	0.666700	0.250000	1.0	0.07408

TEM pictures of Ni₃N produced by this route are shown in Figure 3.5. These show aggregated particles of approximately 20 nm size, with the deviation from that observed by diffraction suggesting the presence of some further disorder in the crystal structure of these particles. Nitrogen adsorption (BET) measurements exhibit a higher surface area in this material of 16.0 m² g⁻¹ compared with the more crystalline sample obtained from nickel hexamine nitrate route.

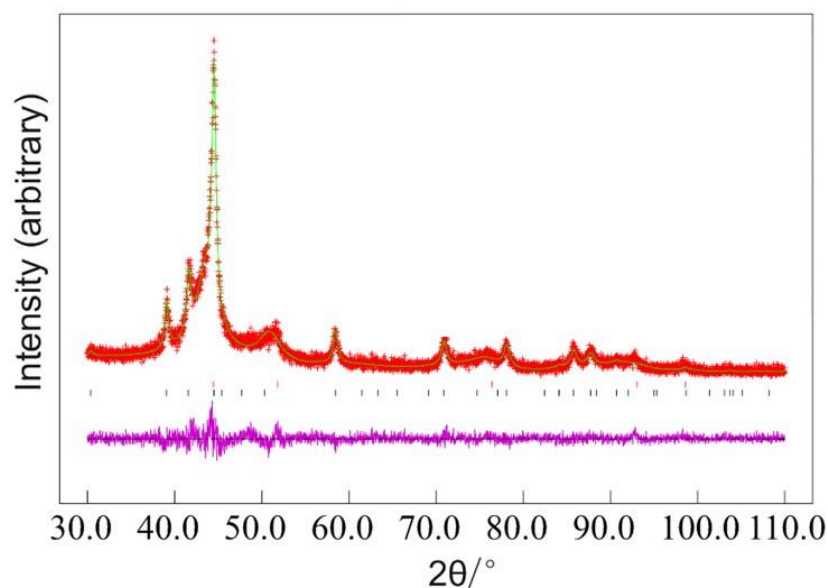


Figure 3.4 Rietveld fit ($R_{wp}=13.5\%$, $R_p=10.3\%$) to the PXD data for Ni₃N produced from ammonolysis of [Ni(EDA)₃](NO₃)₂. Crosses mark the data points, the upper continuous line the fit and the lower continuous line the difference. Tick marks show the allowed positions of reflections for Ni₃N with space group P6₃22, and the upper tick marks those of Ni metal.²¹

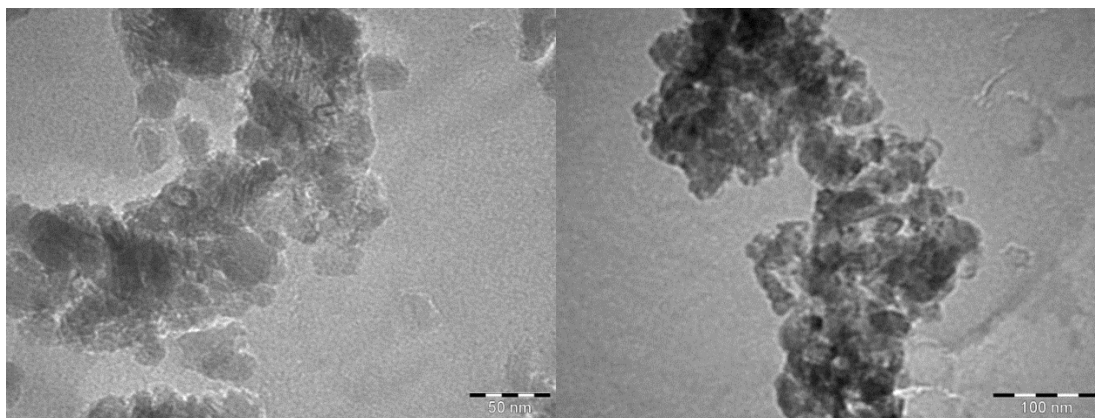


Figure 3.5 TEM pictures of nickel nitride synthesized from nickel *tris*(ethylenediamine) nitrate.

Thermogravimetric analysis (TGA) was conducted by heating from 25 °C to 800 °C with a ramp rate of 10 °C/min in nitrogen and the result is shown in Figure 3.6. TGA shows a much larger mass loss of ~20% from these samples over a broader temperature

range than that observed with the nickel hexamine-derived samples in Figure 3.3.

Previous studies into the formation of metal nitrides from imide-amide polymers have shown that these systems lose most amide and alkylamide groups in this temperature range.²² Furthermore, elemental analysis exhibits the samples to contain 18.2% carbon, 1.7% hydrogen and 16.5% nitrogen (theoretically, 7.4% nitrogen in Ni_3N) and hence these samples are not phase pure Ni_3N and the high carbon and nitrogen content could be attributed to the decomposition of amide and alkylamide groups.

In order to identify whether amide and alkylamide groups have been left in the product, infrared spectra were recorded on a Perkin Elmer Spectrum 100 FTIR with samples prepared as KBr discs. The IR spectra (Figure 3.7) show the presence of amine and amide groups in the form of absorptions at 3150 cm^{-1} ($\nu(\text{NH})$),²² and 1599 cm^{-1} ($\delta(\text{NH}_2)$).^{22, 23} Overall, this material can be considered to consist of nanoparticulate, crystalline Ni_3N with a significant surface coating of organic materials.

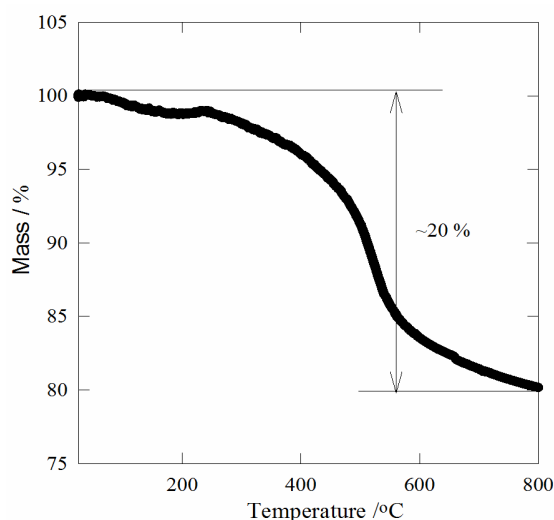


Figure 3.6 TGA trace of Ni_3N sample derived from ammonolysis of $[\text{Ni}(\text{EDA})_3](\text{NO}_3)_2$.

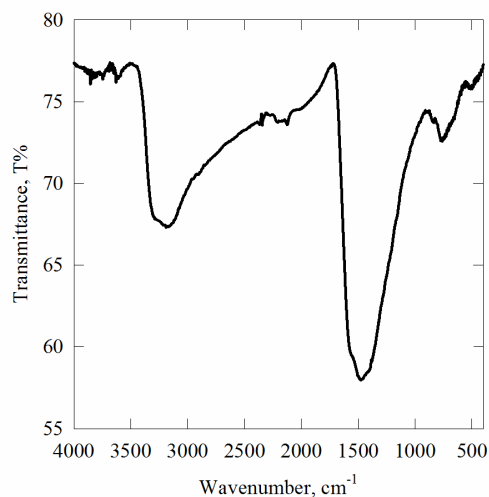


Figure 3.7 IR spectrum of Ni₃N derived from ammonolysis of [Ni(EDA)₃](NO₃)₂.

3.3 Electrochemical performance of nickel nitride in battery applications

The electrochemical performance of nickel nitride in lithium-ion and sodium-ion batteries was investigated in this work. Electrochemical testing used a Bio-Logic SP150 or MPG potentiostat. The working electrode consisted of a powdered mixture of 75% active material with 20% of acetylene black (Shawinigan, Chevron Phillips Chemical Co. LP) and 5% PTFE rolled into a 90 μm thick sheet and then cut into a 10 mm diameter disc.

Electrochemical cells were assembled in two-electrode Swagelok cells using sodium/lithium metal foil (Aldrich, 99.9%) as the counter/reference electrode. Two sheets of Whatman GF/D borosilicate glass fibre were used as separator, soaked with 1 M NaPF₆ in ethylene carbonate/diethyl carbonate (1:1) electrolyte (in Na-ion cells). The electrolyte components were separately dried (solvents dried by distillation from BaO and NaPF₆ dried under vacuum at 80 °C) before combining in the glove box. In lithium

cells, the electrolyte is 1M LiPF₆ in EC:DMC (1:1) (BASF).

3.3.1 Nickel nitride as the negative electrode material for Li-ion batteries

Initially, the behaviours of the two types of Ni₃N prepared in this study were compared with reduction/oxidation rates of 5 C (2115 mA g⁻¹) for lithium-ion half cells as shown in Figure 3.8. The first reduction cycle showed a capacity of 230 mA h g⁻¹ in the [Ni(NH₃)₆](NO₃)₂-derived Ni₃N and 530 mA h g⁻¹ in the [Ni(EDA)₃](NO₃)₂-derived material. In both cases, the capacity dropped significantly in the first 3 cycles, but then stabilised and maintained fairly constant values after 30 cycles, presumably due to solid-electrolyte interphase (SEI) formation. In the higher surface area [Ni(EDA)₃](NO₃)₂-derived sample, the 30th reduction cycle exhibited a specific capacity of 120 mA h g⁻¹ while the [Ni(NH₃)₆](NO₃)₂-derived Ni₃N can offer an approximately 100 mA h g⁻¹ reduction capacity in the 30th cycle.

Figure 3.9 shows the differential capacity plot of Ni₃N derived from two different routes. In both cases, Two large reduction peaks at around 0.5 V and near to 0 V against Li were observed, which are also found in the thin film Ni₃N in lithium cells published before.¹⁸ These peaks could correspond to the reactions of Ni₃N with lithium. The sharp reduction peak at around 0.5 V vanished in the subsequent cycles, suggesting the formation of SEI layer.

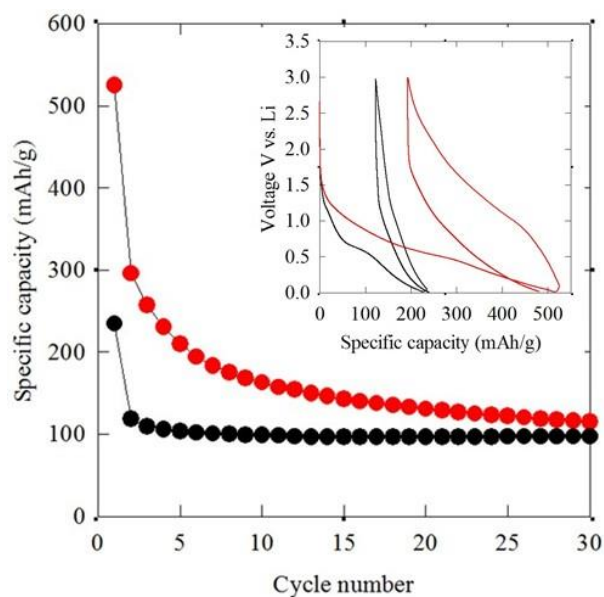


Figure.3.8 Reduction specific capacity vs cycle number of Ni_3N -lithium half cells using $[\text{Ni}(\text{NH}_3)_6](\text{NO}_3)_2$ -derived Ni_3N (black) and $[\text{Ni}(\text{EDA})_3](\text{NO}_3)_2$ -derived Ni_3N (red) cycled between 1 mV and 3 V at 5 C (2115 mA g^{-1}) for 30 cycles. The inset shows voltage vs specific capacity profiles for the first reduction, first oxidation and second reduction. The counter electrode is lithium metal foil and the electrolyte is 1M LiPF_6 in EC:DMC (1:1).

Since the higher surface area $[\text{Ni}(\text{EDA})_3](\text{NO}_3)_2$ -derived Ni_3N has shown a better performance than that of $[\text{Ni}(\text{NH}_3)_6](\text{NO}_3)_2$ -derived Ni_3N , the effect of the current rate on lithium-ion batteries was investigated in the cells using $[\text{Ni}(\text{EDA})_3](\text{NO}_3)_2$ -derived Ni_3N as negative electrode materials. When at different current rates, it can be seen from Figure 3.10 that lower current rate (1 C) can offer a higher reduction capacity, which could be attributed to the internal resistance (IR) drop in the cell increased with the current rate. For example, the first reduction process delivers a capacity of 844 mA h g^{-1} at 1 C (423 mA g^{-1}) but only 530 mA h g^{-1} at 5 C (2115 mA h g^{-1}). The reversibility at both current rates is poor and capacity reduces around 50% in the second cycle, which is similar to phenomenon observed by Gillot *et al.*¹⁴ This defect is the key problem which

hindered the development of conversion mechanism for lithium-ion batteries.²⁴

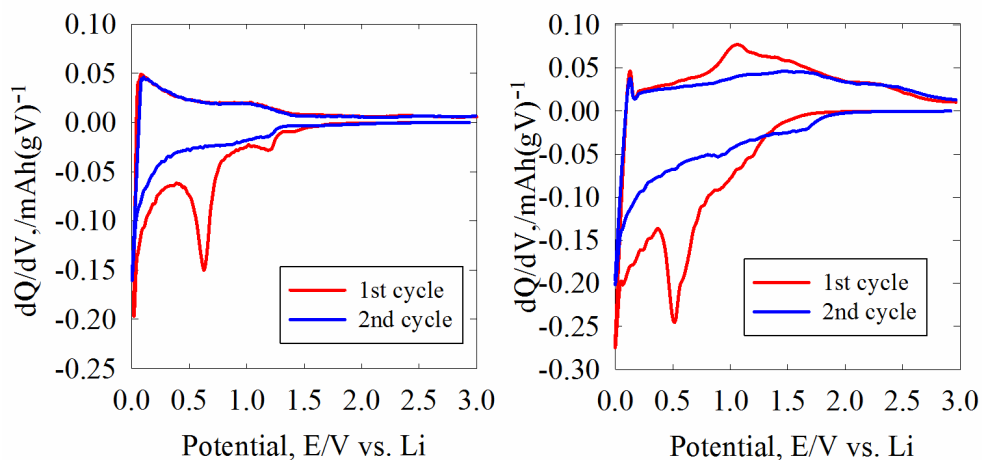


Figure 3.9 Differential capacity versus cell voltage of Ni_3N -lithium half cells using $[\text{Ni}(\text{NH}_3)_6](\text{NO}_3)_2$ -derived Ni_3N (left) and $[\text{Ni}(\text{EDA})_3](\text{NO}_3)_2$ -derived Ni_3N (right) cycled between 1 mV and 3 V at 5 C (2115 mA g^{-1}). The counter electrode is lithium metal foil and the electrolyte is 1M LiPF_6 in EC:DMC (1:1).

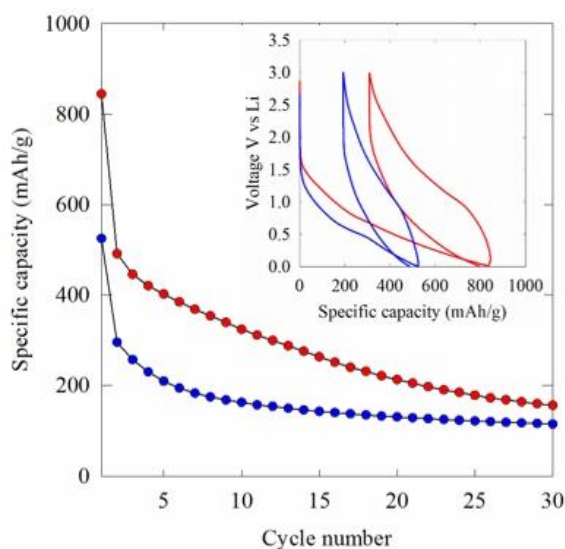


Figure 3.10 Reduction specific capacity versus cycle number and voltage versus specific capacity profile of half lithium cells using $[\text{Ni}(\text{EDA})_3](\text{NO}_3)_2$ -derived Ni_3N cycled between 1 mV and 3 V at 1 C (423 mA g^{-1} red), and 5 C (2115 mA g^{-1} blue), respectively, for 30 cycles. The counter electrode is lithium metal foil and the electrolyte is 1M LiPF_6 in EC:DMC (1:1).

During the first reduction at 1 C, 840 mA h g⁻¹ capacities were obtained as the potential fell from 3 V to 1 mV. However, much of this is believed to be irreversible capacity due to solid-electrolyte interface (SEI)-forming side reactions, as the capacity of 400 mA h g⁻¹ in the first oxidation was retained and this value fell smoothly to ~210 mA h g⁻¹ after 30 cycles. At a faster rate of 5 C (2115 mA g⁻¹) the capacities were lower (530 mA h g⁻¹ in the first reduction and 290 mA h g⁻¹ in the first oxidation) but the capacity profile was more level on cycling, delivering 190 mA h g⁻¹ in the 5th oxidation and 120 mA h g⁻¹ in the 30th oxidation (Figure 3.11), which is similar to the results published by Gillot *et al.*¹⁴ In addition, it can be seen that at both rates the reduction and oxidation curves are close together, and hence the Coulombic efficiency is close to 100% after the first cycle. In all, galvanostatic cycling of the [Ni(EDA)₃](NO₃)₂-derived Ni₃N samples vs Li exhibited very similar results to those recently reported by Gillot *et al.* using nickel amide-derived Ni₃N.¹⁴

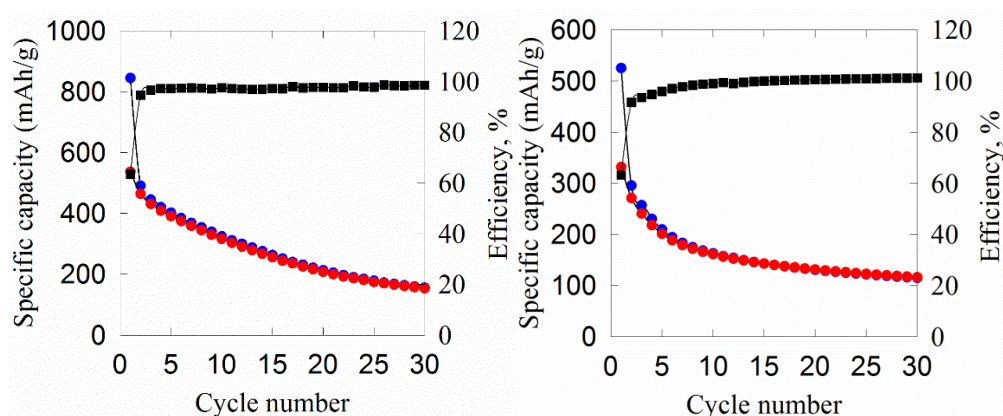


Figure 3.11 Specific capacity versus cycle number profile of Ni₃N-lithium half cells cycled between 1 mV and 3 V for 20 cycles at 1 C (423 mA g⁻¹, left), and 5 C (2115 mA g⁻¹, right). In the specific capacity vs cycle number plots blue circles show specific reduction capacity, red circles show specific oxidation capacity and black squares depict Coulombic efficiency.

3.3.2 Nickel nitride as the negative electrode material for Na-ion batteries

The electrochemical behaviours of the two types of Ni_3N prepared in this study were compared at a cycling rate of 0.5 C (211 mA g^{-1}). In both cases, after the stabilization of the SEI layer as observed in Li cells in the first 5 cycles, the capacity maintained fairly constant after 30 cycles. Specifically, the first reduction cycle showed a capacity of 120 mA h g^{-1} in the $[\text{Ni}(\text{NH}_3)_6](\text{NO}_3)_2$ -derived Ni_3N and 465 mA h g^{-1} in the $[\text{Ni}(\text{EDA})_3](\text{NO}_3)_2$ -derived material (Figure 3.12). In the higher surface area $[\text{Ni}(\text{EDA})_3](\text{NO}_3)_2$ -derived sample the 30th reduction cycle showed a specific capacity of 126 mA h g^{-1} . The higher capacity from the $[\text{Ni}(\text{EDA})_3](\text{NO}_3)_2$ -derived material exhibits that despite the expected conversion mechanism the particle size is very significant in determining the capacity that can be derived from Ni_3N . Hence further cycling studies focussed on this smaller particle size material. The inset to Figure 3.12 shows that most of the oxidation profile is observed below 1.5 V and hence use of Ni_3N as a negative electrode in high voltage cells, where the oxidation process would occur during cell discharge, is feasible.

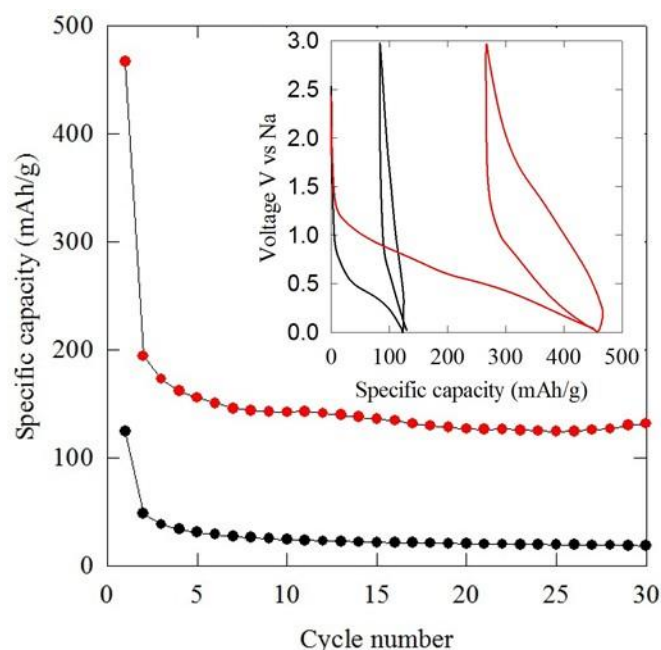


Figure 3.12 Reduction specific capacity versus cycle number of Ni_3N -sodium half cells using $[\text{Ni}(\text{NH}_3)_6](\text{NO}_3)_2$ -derived Ni_3N (black) and $[\text{Ni}(\text{EDA})_3](\text{NO}_3)_2$ -derived Ni_3N (red) cycled between 1 mV and 3 V at 0.5 C (211 mA g^{-1}) for 30 cycles. The inset shows voltage vs specific capacity profiles for the first reduction, first oxidation and second reduction.

As with that in lithium ion cells, the differential capacity plot of Ni_3N in Na-ion cells exhibits a sharp reduction peak in the first cycle at around 0.5 V in both cases, which corresponds to the shoulder slope in the first reduction of their voltage profiles. And this reduction peak was not found in the subsequent cycles, suggesting the irreversible process of the formation of SEI layer. The voltage hysteresis of Ni_3N in Na-ion cells cycled at 0.5 C (211.5 mA g^{-1}) can be observed in Figure 3.13. It can be seen that $[\text{Ni}(\text{EDA})_3](\text{NO}_3)_2$ -derived Ni_3N with small particle size showed a lower voltage hysteresis (around 0.7 V) than that of $[\text{Ni}(\text{NH}_3)_6](\text{NO}_3)_2$ -derived Ni_3N (0.9 V), which could be attributed to the small particles shortened the electron pathway

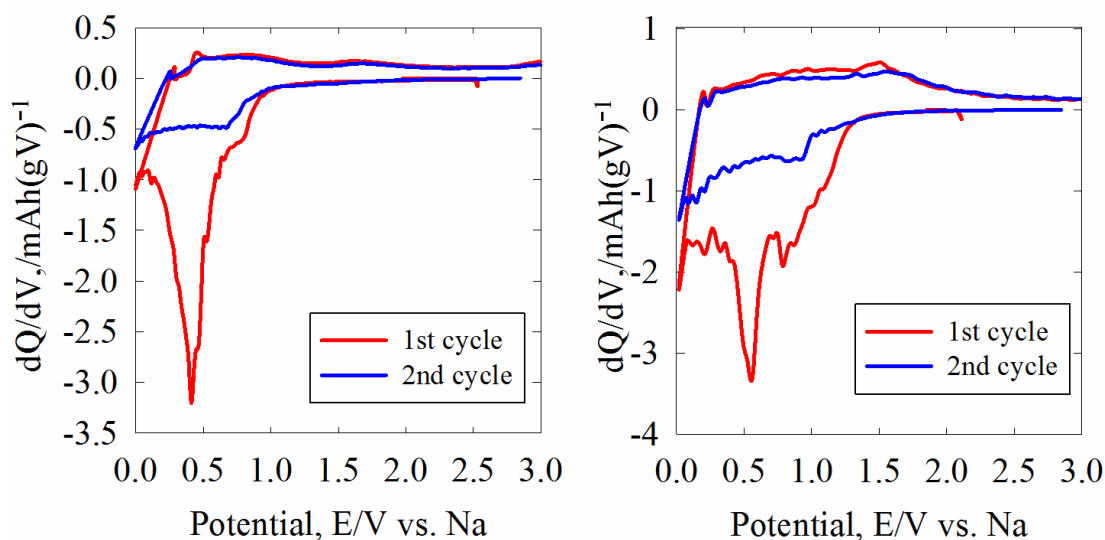


Figure 3.13 Differential capacity versus cell voltage of Ni_3N -sodium half cells using $[\text{Ni}(\text{NH}_3)_6](\text{NO}_3)_2$ -derived Ni_3N (left) and $[\text{Ni}(\text{EDA})_3](\text{NO}_3)_2$ -derived Ni_3N (right) cycled between 1 mV and 3 V at 0.5 C (211.5 mA g^{-1}). The counter electrode is lithium metal foil and the electrolyte is 1M NaPF_6 in EC:DEC (1:1).

The cyclic voltammetry of $[\text{Ni}(\text{EDA})_3](\text{NO}_3)_2$ -derived Ni_3N was conducted at 5 mV s^{-1} between 1 mV and 3 V for 30 cycles. (Figure 3.14) It can be seen that a large amorphous reduction peak at around 0.2 V and a small reduction peak at around 1.5 V in the first negative scan. The sharp reduction peak was not observed in the subsequent cycles, suggesting the irreversible charge storage due to the formation of solid electrolyte interphase (SEI). The charge reduced significantly after the first cycle and gradually stabilized in the subsequent cycles, which is observed in its galvanostatic performance. It also can be found the large voltage polarization increased during the cycling, which could be due to the internal resistance increased with the SEI layer formation.

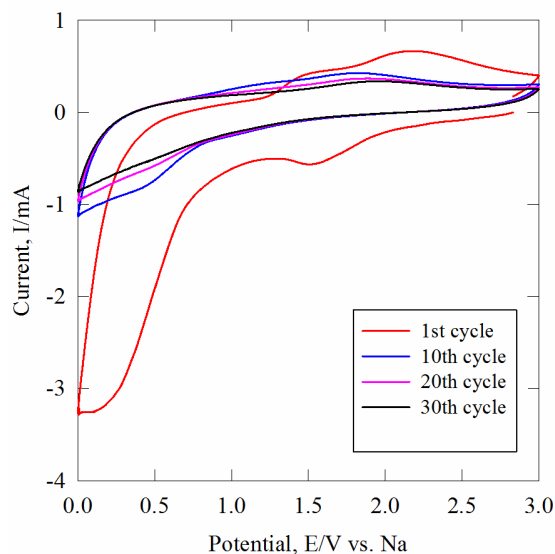


Figure 3.14 Cyclic voltammetry at 5 mV s^{-1} of Ni_3N derived from $[\text{Ni}(\text{EDA})_3](\text{NO}_3)_2$ in the 1st, 10th, 20th and 30th cycle. The counter electrode and reference electrode is sodium metal foil and the electrolyte is 1M NaPF_6 in EC:DEC (1:1).

The galvanostatic electrochemical performance of sodium-ion batteries using $[\text{Ni}(\text{EDA})_3](\text{NO}_3)_2$ -derived Ni_3N was investigated at different current rates. The results are shown in Figure 3.15. Similar cycling performance to that found in lithium-ion batteries was observed. The reversibility in initial cycles is still poor, which may be attributed to the SEI formation. At a lower current rate, sodium cells exhibit a higher reduction capacity. For example, when cycling at 0.1 C (42.3 mA g^{-1}), it has a 227 mA h g^{-1} first reversible reduction capacity and 134 mA h g^{-1} of this capacity is maintained in the 20th cycle. In contrast, when cycling at a higher current rate, 1 C (423 mA g^{-1}), it can only offer a 137 mA h g^{-1} first reversible reduction capacity and 80 mA h g^{-1} in the 20th cycle.

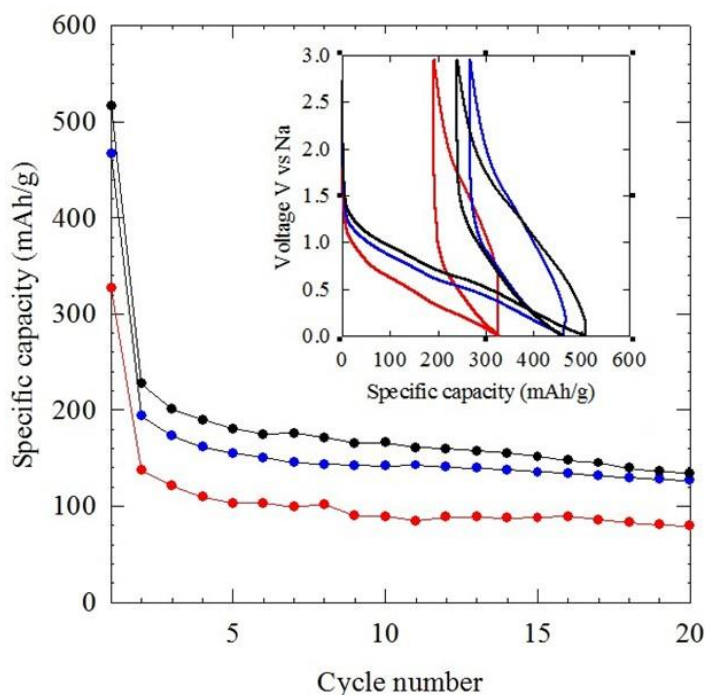


Figure 3.15 Reduction specific capacity versus cycle number and voltage versus specific capacity profile of half sodium cells using $[\text{Ni}(\text{EDA})_3](\text{NO}_3)_2$ -derived Ni_3N cycled between 1 mV and 3 V at 423 mA g^{-1} (red), 211 mA g^{-1} (blue) and 42.3 mA g^{-1} (black), respectively, for 20 cycles. The counter electrode is sodium metal foil and electrolyte is 1M NaPF_6 in EC:DEC (1:1).

The loss of current to SEI formation during initial cycles means that consideration of the oxidation process, which is discharge in the context of using Ni_3N as the negative electrode in a sodium-ion cell, and the Coulombic efficiency (charge passed on discharging/oxidation divided by charge passed on charging/reduction) are as important as the specific capacity. Figure 3.16 shows the performance for $[\text{Ni}(\text{EDA})_3](\text{NO}_3)_2$ -derived Ni_3N -sodium half cells cycling at various current rates. It is interesting that at all three rates the reduction and oxidation curves are close together, and hence the Coulombic efficiency is close to 100%, from the third cycle. This suggests that irreversible processes such as SEI formation are close to complete at this

point. The specific capacity is always greater at lower reduction/oxidation rates, e.g. the first reduction process requires 517 mA h g^{-1} of charge at 0.1 C (42.3 mA g^{-1}) but only 326 mA h g^{-1} at 1 C (423 mA h g^{-1}). The first oxidation delivers 137 (1 C), 193 (0.5 C) or 227 (0.1 C) mA h g^{-1} and after 20 cycles these values fall to 80 (1 C), 126 (0.5 C) or 134 (0.1 C) mA h g^{-1} . The $\sim 75\%$ reduction capacity drop on cycling was similar to that previously¹⁴ (and herein) observed for Ni_3N -lithium cells but note that a smaller drop in capacity is observed when only the oxidation (sodium-ion cell discharge) process is considered.

The mechanism of charge storage by Ni_3N in sodium cells was explored by collecting X-ray diffraction data on an assembled Ni_3N composite electrode, electrochemically reducing it in a sodium half-cell to 1 mV at a slow scan rate to maximise conversion, and re-recording the diffraction pattern (without air exposure) under identical conditions. In contrast to studies on Ni_3N thin films cycled vs Li where crystalline Ni was observed,²⁵ no new peaks, e.g. assigned to Na_3N , were found suggesting that the reduction products were amorphous. Interestingly, though, the Ni_3N peaks were only reduced in magnitude. This suggests that the reaction occurred at the surface layer and not all active material was involved in this electrochemical process and herein still smaller crystallites might result in the availability of greater capacity as the accessibility to the electrode increased with larger specific surface area. It is possible that the reducing capacity on cycling is due to gradual consumption of the Ni_3N active material, but note that after 20 cycles the specific oxidation capacity at 0.1 C (134 mA h g^{-1}) is still 32% of the theoretical capacity of 423 mA h g^{-1} for complete conversion to Ni metal and Na_3N .

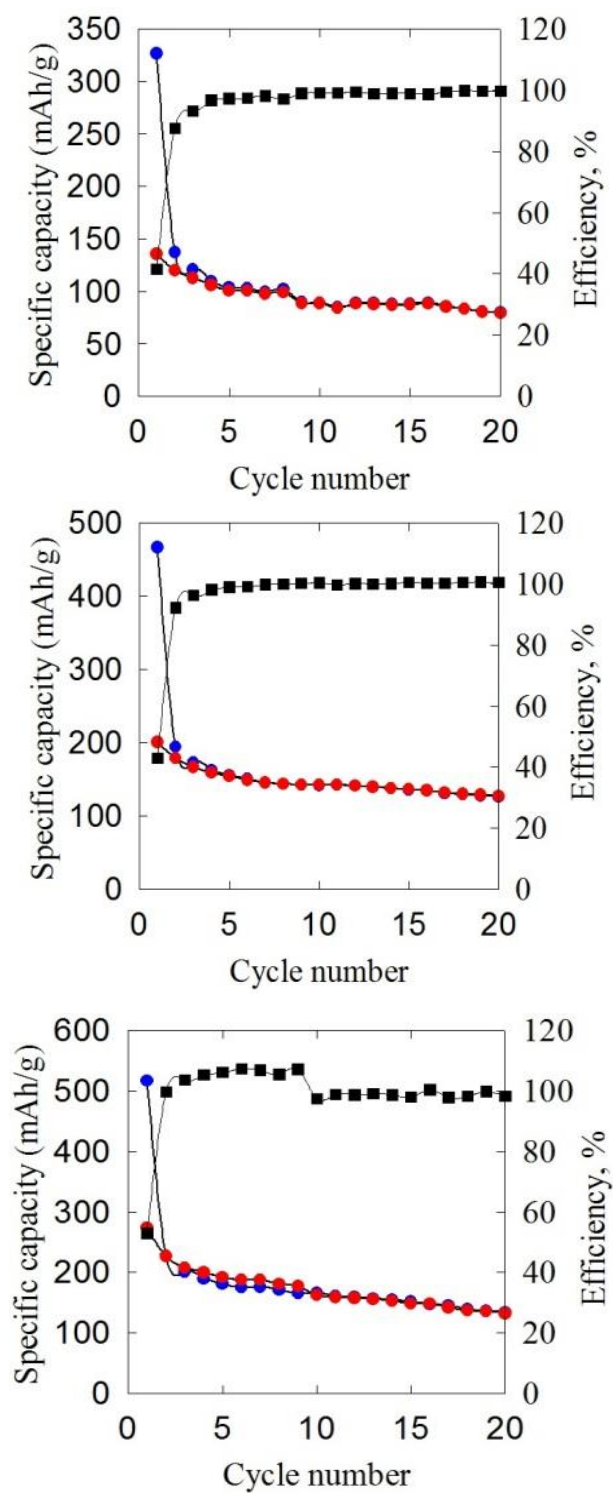


Figure 3.16 Specific capacity versus cycle number profile of Ni₃N-sodium half cells cycled between 1 mV and 3 V for 20 cycles at 1 C (423 mA g⁻¹, top), 0.5 C (211.5 mA g⁻¹, centre) and 0.1 C (42.3 mA g⁻¹, bottom).

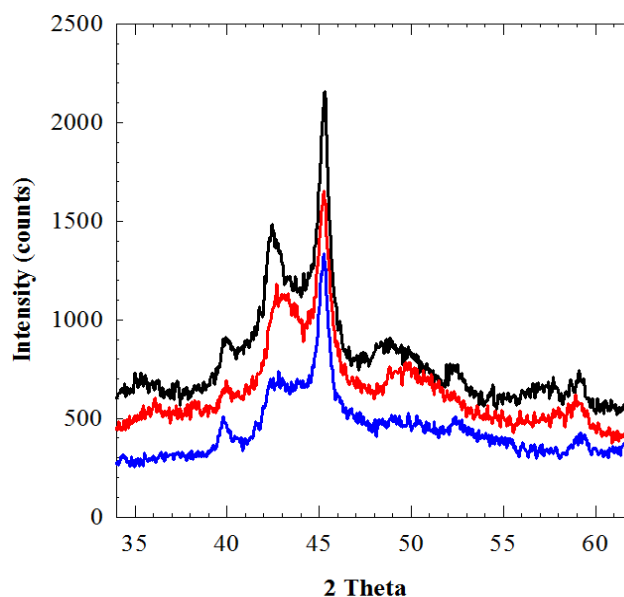


Figure 3.17 *Ex situ* PXD patterns of Ni_3N electrodes before any electrochemical cycling (top), after reduction at a rate of 0.067 C (28.2 mA g^{-1}) to 0.001 V (middle) and after reduction at a rate of 0.5 C (211.5 mA g^{-1}) for 20 cycles (bottom). PXD patterns were collected on the same sample before and after reduction with the same geometry and detector integration regions to ensure comparability.

Overall, the performance of Ni_3N as the active material for negative electrodes in sodium-ion cells is comparable with that of many of the best materials in the literature. The best capacity after 20 cycles (134 mA h g^{-1}) exceeds the capacity of carbon black, for which extended cycling studies were not reported, with charge and discharge over a similar potential range.²⁶ “Templated carbon”²⁷ and $\text{NaTi}_2(\text{PO}_4)_3$ ²⁸ both delivered $\sim 120 \text{ mA h g}^{-1}$ over this number of cycles, again with a similar potential range. “Hard carbon” has significantly higher capacity but was initially found to plate sodium during charging, making it unacceptable for use over multiple cycles due to the risk of dendrite formation.²⁹ A more recent study of hard carbon found it possible to show $\sim 220 \text{ mA h g}^{-1}$ reversible capacity over 100 cycles,³⁰ and a similar performance has been

demonstrated in hollow carbon nanowire materials.¹⁶ It is likely that the already promising performance of Ni₃N might be further improved by reductions in particle size to bring it closer to this performance level, since the diffraction results show incomplete conversion.

3.3.3 Effects of electrolytes on the performance of Ni₃N in sodium-ion batteries

In 2011, Komaba *et al*³⁰ have studied different electrolytes, in the form of 1M NaClO₄ in EC: DMC, PC and EC. They found that 1M NaClO₄ in PC electrolyte can provide an optimal performance for hard carbon negative electrode materials in sodium-ion cells. After that, in 2012, Ponrouch *et al.*³¹ investigated electrolytes for sodium-ion cells and compared the performance of NaClO₄ and NaPF₆. They benchmarked various electrolytes containing diverse solvent mixtures (cyclic, acyclic carbonates, glymes), and concluded that the two different sodium salts have similar performance in sodium-ion cells and EC: PC binary electrolyte gave the best performance. The cell using EC:PC electrolyte exhibited the capacity of 180 mA h g⁻¹ over 70 cycles in the hard carbon-sodium half-cell while the PC and EC:DEC electrolytes were rapidly faded after 30 cycles. As a result, 1M NaClO₄ in PC and 1M NaPF₆ in EC: PC electrolytes have been made. After drying PC (propyl carbonate) by distillation from BaO and drying NaClO₄ and NaPF₆ at 130 °C, two types of electrolytes were prepared by certain mixture. The performance of the sodium half cells using Ni₃N as the negative electrode material with these electrolytes is shown below.

It can be seen from Figure 3.18 that 1M NaPF₆ in EC:PC has the best performance of

the three. Specifically the first reversible reduction capacity is 227 mA h g⁻¹, which is higher than 1M NaPF₆ in EC:DEC (193 mA h g⁻¹) and 1M NaClO₄ in PC (178 mA h g⁻¹). After 30 cycles, it remains 134 mA h g⁻¹ which is similar to that of 1M NaPF₆ in EC:DEC (131 mA h g⁻¹). For 1M NaClO₄ in PC, the capacity decreased to 102 mA h g⁻¹ in the 30th cycle. This improvement of 1M NaPF₆ in EC:PC in cycling performance could be attributed to the stable SEI layer formed during cycling. In all, by comparing the three different types electrolytes, 1M NaPF₆ in EC:PC can offer an optimal performance in sodium-ion batteries using nickel nitride as the negative electrode material, which is consistent with the literature results.³¹ However, not massive improvements were found against the current using electrolyte, 1M NaPF₆ in EC:DEC.

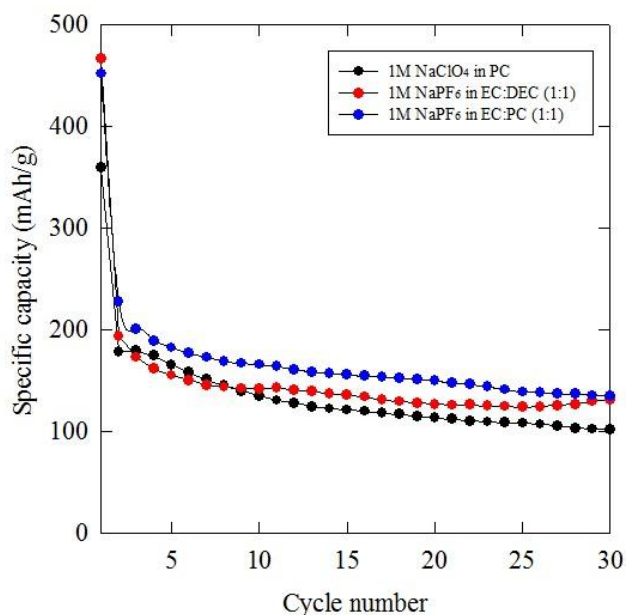


Figure 3.18 Specific capacity versus cycles of three electrolytes at 0.5 C rate. The working electrode is [Ni(EDA)₃](NO₃)₂-derived Ni₃N and the counter electrode is sodium foil.

3.4 Conclusions

Nickel nitride has been synthesized from two routes. One is from ammonolysis of

nickel hexamine nitrate at 335 °C for 6 h followed by 200 °C for 8 h, the other is from heating nickel *tris*(ethylenediamine) nitrate at 360 °C for 4 h then 200 °C for 40 h under flowing ammonia. Characterization of nickel nitride, in terms of powder XRD, TEM, TGA and CHN analysis, has been conducted.

Furthermore, the electrochemistry of Ni₃N has been investigated in lithium-ion as well as sodium-ion batteries. For the cycling performance in lithium-ion cells,

[Ni(EDA)₃](NO₃)₂-derived Ni₃N sample showed similar performance to amide-derived Ni₃N published by Gillot *et al.*¹⁴ It can deliver a quite high specific reduction capacity, which is around 3 times ($\sim 1200 \text{ mA h g}^{-1}$) more than its theoretical specific capacity (423 mA h g⁻¹), in the first reduction process. However, the cycling stability of this material for lithium ion batteries is not satisfied.

Ni₃N was applied as the negative electrode material in sodium ion batteries for the first time. And it showed good capacity and cycling characteristics on redox cycling vs sodium. Although the Coulombic efficiency in the first cycle is low, around 45%, the cycling performance (134 mA h g⁻¹ at 0.5 C after 20 cycles) can be competitive with the most nanoparticulate carbon materials.

3.5 Reference

1. R. Marchand, F. Tessier and F. J. DiSalvo, *J. Mater. Chem.*, 1999, 9, 297.
2. A. J. Steckl and R. Birkhahn, *Appl. Phys. Lett.*, 1998, 73, 1700.
3. A. A. Andreev, *Phys. Solid State*, 2003, 45, 419.
4. K. P. O. Donnell and B. Hourahine, *Eur. Phys. J. Apply. Phys.*, 2006, 36, 91.
5. I. M. Neklyudov and A. N. Morozov, *Phys. B: Conden. Matt.*, 2004, 350, 325.
6. M. Kawamura, Y. Abe and K. Sasaki, *Vacuum*, 2000, 59, 721.

7. P. Kroll, *J. Solid State Chem.*, 2003, 176, 530.
8. A. Leineweber, H. Jacobs and S. Hull, *Inorg. Chem.*, 2001, 40, 5818.
9. N. S. Gajbhiye, R. S. Ningthoujam and J. Weissmüller, *Phys. status solidi (a)*, 2002, 189, 691.
10. V. R. Juza and F. Hund, *Allg. Chem.*, 1948, 257 13.
11. Z. Wang, W. Yu, J. Chen, M. Zhang, W. Li and K. Tao, *J. Alloy. Compd.*, 2008, 466, 352.
12. R. Juza, W. Sachsze and Z. Anorg, *Allg. Chem.*, 1943, 251, 201.
13. A. Baiker and M. Maciejewski, *J. Chem. Soc.*, 1984, 80, 2331.
14. F. Gillot, J. Oro-Sole and M. R. Palacin, *J. Mater. Chem.*, 2011, 21, 9997.
15. S. Dhar, L. Rissanen, K. Engel, M. Wenderoth and K. P. Lieb, *Nucl. Instrum. Meth. B*, 2001, 178, 297.
16. L. Rissanen, S. Dhar, K. P. Lieb, K. Engel and M. Wenderoth, *Nucl. Instru. Meth. B*, 2000, 161, 986.
17. L. Maya, T. Thundat, J. R. Thompson and R. J. Stevenson, *Appl. Phys.Lett.*, 1995, 67, 3034.
18. Y. Wang, W. Y. Liu and Z. W. Fu, *Acta Phys. Chim. Sin.*, 2006, 22, 65.
19. N. S. Gajbhiye, Ningthoujam, R.S. and Weissmüller, J., *Phys. status solidi (a)*, 2002, 189, 691.
20. H. M. Rietveld, *J. Appl. Cryst.*, 1969, 2, 65.
21. Inorganic Crystal Structure Database (ICSD, Fiz Karlsruhe) accessed via the National Chemical Database Service hosted by the Royal Society of Chemistry.
22. D. V. Baxter, M. H. Chisholm, G. J. Gama, V. F. DiStasi, A. L. Hector and I. P. Parkin, *Chem. Mater.*, 1996, 8, 1222.
23. K. Nakamoto, *Infrared and Raman Spectra of Inorganic Compounds, Theory and Applicatios in Inorganic Chemistry*, Wiley-Interscience, 1997.
24. A. L. Dalverny, J. S. Filhol and M. L. Doublet, *J. Mater. Chem.*, 2011, 21, 10134.

25. Y. Wang, Z.-W. Fu, X.-L. Yue and Q.-Z. Qin, *J. Electrochem. Soc.*, 2004, 151, E162.
26. R. Alcántara, J. M. Jiménez-Mateos, P. Lavela and J. L. Tirado, *Electrochem. Commun.*, 2001, 3, 639.
27. S. Wenzel, T. Hara, J. Janek and P. Adelhelm, *Energy Environ. Sci.*, 2011, 4, 3342.
28. S. I. Park, I. Gocheva, S. Okada and J.-i. Yamaki, *J. Electrochem. Soc.*, 2011, 158, A1067.
29. D. A. Stevens and J. R. Dahn, *J. Electrochem. Soc.*, 2000, 147, 1271.
30. S. Komaba, W. Murata, T. Ishikawa, N. Yabuuchi, T. Ozeki, T. Nakayama, A. Ogata, K. Gotoh and K. Fujiwara, *Adv.Funct. Mater.*, 2011, 21, 3859.
31. A. Ponrouch, E. Marchante, M. Courty, J.-M. Tarascon and M. R. Palacin, *Energy Environ. Sci.*, 2012, 5, 8572.

Chapter 4. Copper nitride as the negative electrode material for sodium-ion batteries

4.1 Introduction

Copper nitride (Cu_3N) has been studied as a promising material for optical storage devices,^{1,2} high-speed integrated circuits,³ and microscopic metal links.^{4,5} Copper nitride was firstly studied by Juza and Hahn in the early 1940s.⁶ After that, related work focused on the synthesis of Cu_3N films by various techniques.^{5,7,8} Bulk copper nitride has been successfully prepared from ammonolysis of CuF_2 at 300 °C,⁹ and nanocrystalline copper nitride can also be obtained from solvothermal synthesis route.¹⁰ Apart from the more traditional solid state synthesis routes, Haibin *et al.* have developed a solution phase route in which size controlled copper nitride nanocubes can be synthesized from a one phase facile process in organic solvents.¹¹

In recent years, the electrochemical properties of copper nitride have been explored. Copper nitride (Cu_3N) is an intriguing phase for comparison as it adopts an anti- ReO_3 type structure (Figure 4.1) with a vacant site that could be occupied by cations, and which is occupied by further copper atoms in the anti-perovskite Cu_4N .¹²⁻¹⁵ Haibin *et al.* demonstrated that Cu_3N nanocubes are promising Pt-free electrocatalysts for alkaline fuel cell applications.¹¹ In lithium cells Pereira *et al* showed an initial lattice expansion that they attributed to lithium insertion, followed by reduction to copper metal and Li_3N .¹⁶ After an initial loss of capacity these electrodes provided stable reduction capacities of 140-170 mA h g^{-1} at 1.67 C, and an unusual gradual increase in capacity when they were

oxidised beyond 2 V vs Li, which the authors attributed to oxide formation linked to the electrolyte degradation.

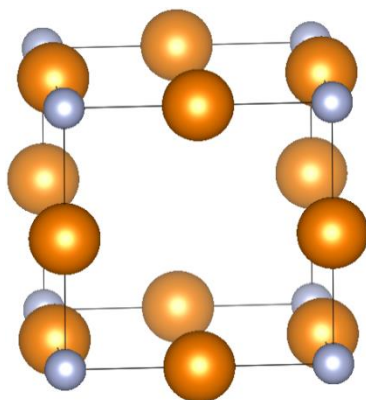


Figure 4.1 The anti-ReO₃ structure of Cu₃N (Cu atoms as large orange spheres, N as small blue spheres) showing the linear CuN₂ coordination.¹³

In this work, copper nitride was synthesized from two different routes; one is from ammonolysis of anhydrous CuF₂ salts, the other was from ammonolysis of copper pivalate salts. Their electrochemical performance in sodium and lithium-half cells was evaluated.

4.2 Synthesis and characterization of copper nitride

4.2.1 Copper nitride derived from ammonolysis of anhydrous copper

fluoride

This route was previously described by Pereira *et al.*⁹ Specifically, anhydrous copper fluoride (2 g, Aldrich, 99%) was dried in flowing nitrogen at 140 °C for 6 h then heated to 300 °C at 2 °C min⁻¹ under flowing ammonia (BOC anhydrous grade, further dried with 3 Å molecular sieves) and maintained at 300 °C for 8 h.

Rietveld refinement of the diffraction data (Figure 4.2) yielded lattice parameters of $a = 3.81105(5) \text{ \AA}$, which is in the range of previous reports containing lattice parameters between 3.802 and 3.819 \AA .¹⁷ A refined crystallite size of 412(11) nm was calculated from the Lorentzian components of the profile fit.¹⁸

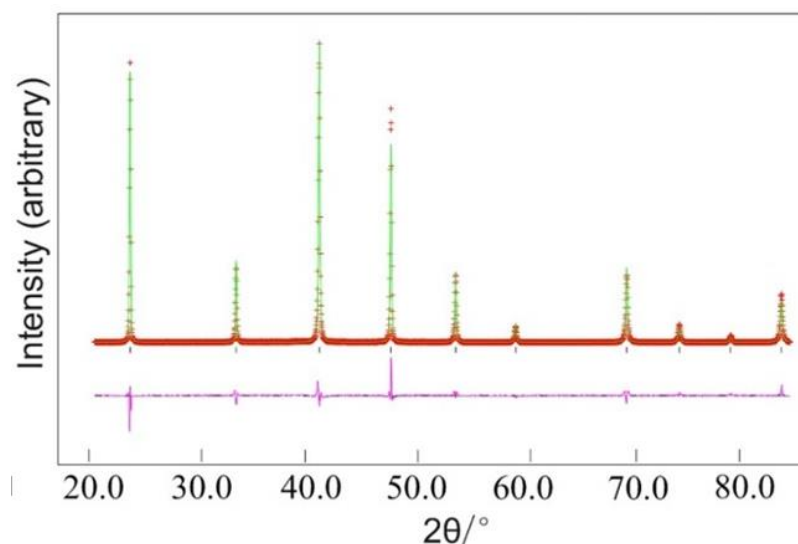


Figure 4.2 Rietveld fit ($R_{wp} = 12.6\%$, $R_p = 9.3\%$) to the PXD data for Cu_3N produced from ammonolysis of anhydrous copper fluoride at 300 °C. Crosses mark the data points, the upper continuous line the fit and the lower continuous line the difference. Tick marks show the allowed positions of reflections for Cu_3N with space group Pm-3m.¹⁹

TEM images (Figure 4.3) exhibit large crystallite with a diameter of around 400 nm. The large particle size could result in a low accessible surface. In BET measurement, it shows approximately $1 \text{ m}^2 \text{ g}^{-1}$ specific surface area of the sample obtained from ammonolysis of anhydrous copper fluoride at 300 °C.

Infrared spectroscopy (IR) result shows a sharp copper-nitrogen bond at around 630 cm^{-1} which is close to the reported value, 642 cm^{-1} .²⁰ Also, there are several minor peaks at around 3400 cm^{-1} and 1400 cm^{-1} , which could be the form of absorptions of hydroxyl

group.²² This could be due to the minor moisture attaching to the sample surface. This result is consistent to its combustion analysis which shows no traceable carbon or hydrogen found in this sample.

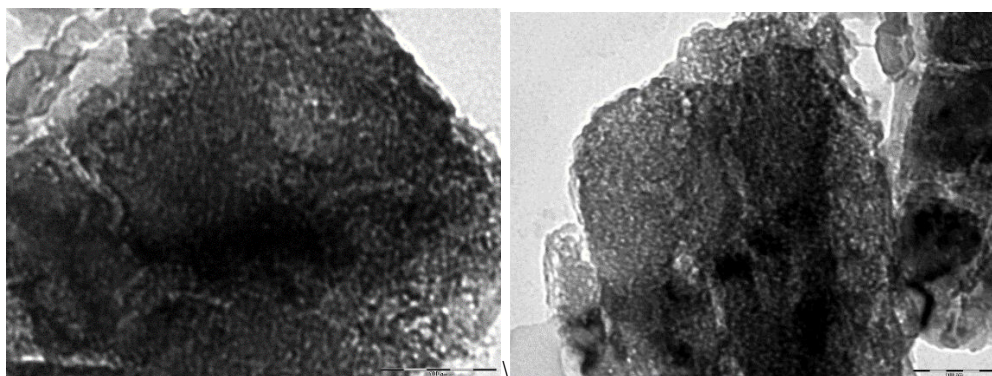


Figure 4.3 TEM image (scale bar = 100 nm) of Cu₃N produced from ammonolysis of anhydrous copper fluoride at 300 °C.

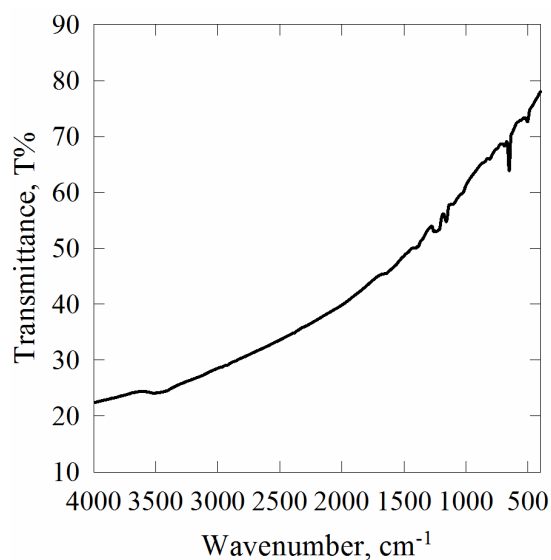


Figure 4.4 Infrared spectroscopy (IR) of Cu₃N produced from ammonolysis of anhydrous copper fluoride at 300 °C.

Thermogravimetric analysis (TGA) exhibits approximately 8% mass loss when the sample was heated up to 900 °C. It can be found in Figure 4.5 that the minor mass loss occurred at around 300 °C and a distinct mass loss observed around 480 °C. This is

consistent to the previous published results showing Cu_3N started to loss nitrogen at around $300\text{ }^\circ\text{C}$ and completed reduced to Cu at around $500\text{ }^\circ\text{C}$.²¹ Its combustion analysis shows this material contains 6.6% nitrogen in mass (6.8% calculated for Cu_3N).

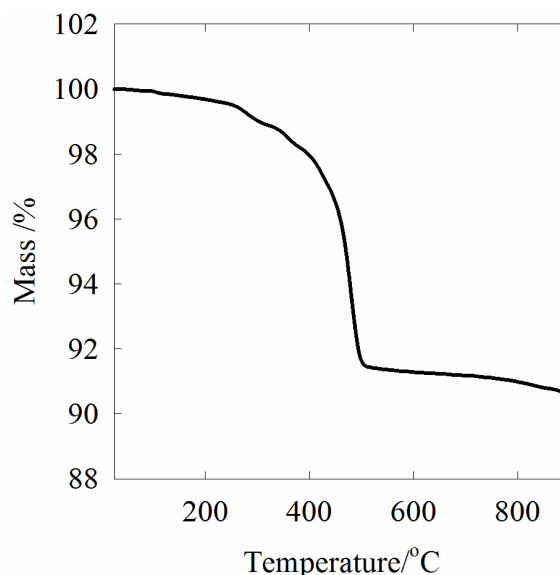


Figure 4.5 Thermogravimetric analysis (TGA) of Cu_3N produced from ammonolysis of anhydrous copper fluoride at $300\text{ }^\circ\text{C}$.

4.2.2 Copper nitride derived from ammonolysis of copper pivalate

This route is described by Giordano *et al.*²² 2 g of copper (II) carbonate basic – $\text{CuCO}_3 \cdot \text{Cu}(\text{OH})_2$ – from Aldrich were dissolved in 30 mL of deionised water and left for 15 minutes at $50\text{ }^\circ\text{C}$ in order to help the dissociation of $\text{Cu}(\text{II})$. After that, 25 ml of pivalic acid from Aldrich (99%) was added to the solution and stirred for 30 minutes at $70\text{ }^\circ\text{C}$ to release CO_2 and to precipitate copper(II) pivalate salt. The solution was then cooled down to room temperature and filtered to recover the product. The final product is dark green fine powder. Then the powder was heated at $250\text{ }^\circ\text{C}$ for 10 h under flowing ammonia gas (BOC anhydrous grade, further dried by flowing over 3 \AA

molecular sieves).

Ammonolysis of copper(II) pivalate was carried out at various temperatures with the aim of producing a lower crystallite size, thereby higher surface area sample of Cu_3N . At 180 °C peaks, corresponding to Cu_3N were found in a mixture of phases, which could be attributed to uncompleted reaction. And when at 200 and 250 °C, phase-pure Cu_3N was obtained. Then at 300 °C, the decomposition to copper metal was observed.²³ (Figure 4.6) Due to some irreproducibility at 200 °C, samples produced at 250 °C were carried forward for further study.

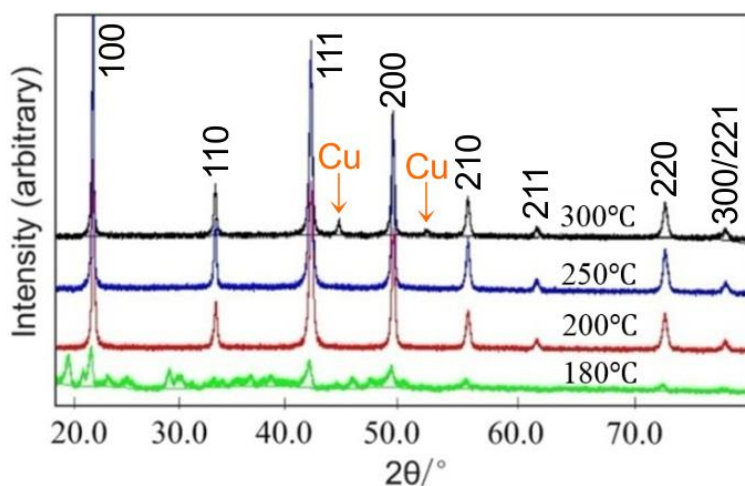


Figure 4.6 Powder XRD pattern of the products of ammonolysis of copper(II) pivalate at various temperatures (10 h heating time). Phase-pure Cu_3N is obtained at 200 and 250 °C.

The sample obtained at 250 °C was found to have $a = 3.811495(22)$ Å and a crystallite size of 51.3(1) nm was calculated from the Lorentzian components of the profile fit.¹⁸ (Figure 4.7). TEM images (Figure 4.8) exhibit small crystallites with a diameter of ~ 20 to 30 nm. These small crystallites were aggregated in the certain regions of the images. Comparing with Cu_3N derived from CuF_2 route, the accessible surface should be larger observing from the images. In BET measurements, it shows a higher surface area, $6 \text{ m}^2 \text{ g}^{-1}$,

than that derived from CuF_2 route, $1 \text{ m}^2 \text{ g}^{-1}$, which is consistent to the TEM and PXD results.

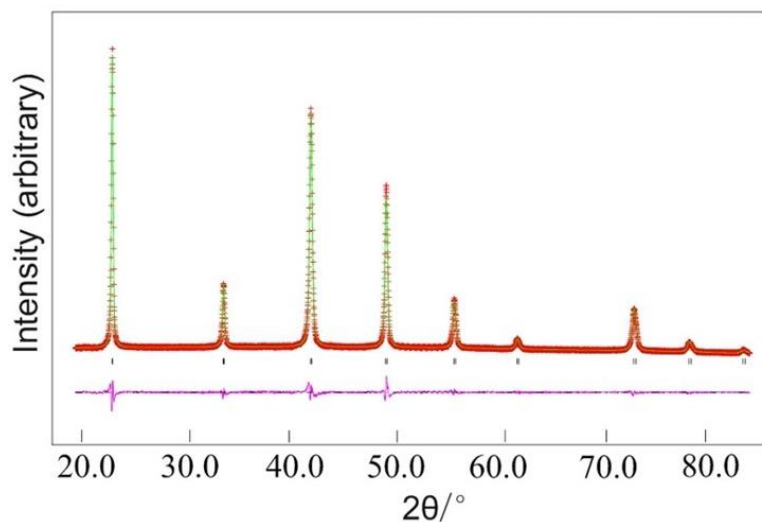


Figure 4.7 Rietveld fit ($R_{\text{wp}} = 3.8\%$, $R_{\text{p}} = 2.8\%$, crystallite size = $51.3(1) \text{ nm}$) to the PXD data for Cu_3N produced from ammonolysis of copper(II) pivalate at $250 \text{ }^\circ\text{C}$. Crosses mark the data points, the upper continuous line the fit and the lower continuous line the difference. Tick marks show the allowed positions of reflections for Cu_3N with space group $Pm-3m$.¹⁹

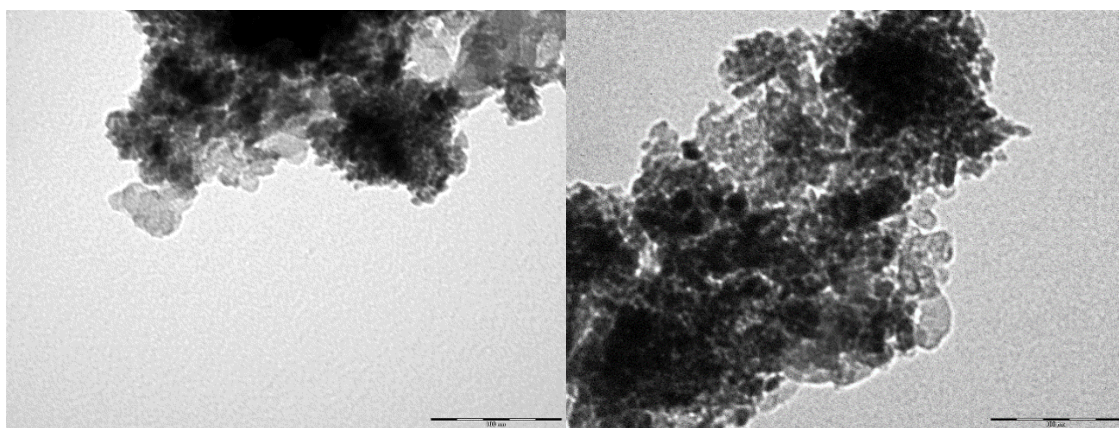


Figure 4.8 TEM image (scale bar = 100 nm) of Cu_3N produced from ammonolysis of copper(II) pivalate at $250 \text{ }^\circ\text{C}$.

Comparing with the sample derived from CuF_2 precursor, Cu_3N obtained from

ammonolysis of copper pivalate exhibits a similar IR result (Figure 4.9). A sharp copper-nitrogen bond at around 600 cm^{-1} which is close to the reported value, 642 cm^{-1} .²⁰ Its IR spectra also show several extra peaks at around 2800 cm^{-1} and 1400 cm^{-1} , which could be corresponding to alkyl group²² due to the residues of the precursor.

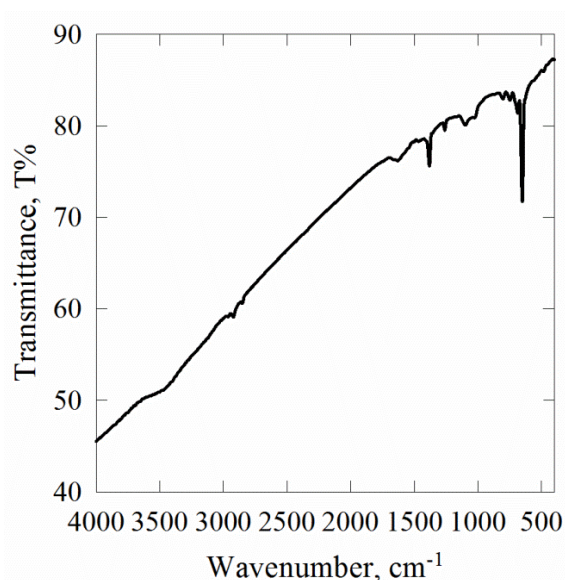


Figure 4.9 Infrared spectroscopy (IR) of Cu_3N produced from ammonolysis of copper(II) pivalate at $250\text{ }^\circ\text{C}$.

Thermogravimetric analysis (TGA) exhibits approximately 10% mass loss when the sample was heated up to $900\text{ }^\circ\text{C}$, which is a little higher than that of the sample obtained from CuF_2 route. As with Cu_3N derived from ammonolysis of CuF_2 , the TGA graph of the sample obtained from pivalate route shows the similar mass loss curve, a distinct mass loss observed around $480\text{ }^\circ\text{C}$. But, it can be found in Figure 4.10 that the mass occurred to loss at a lower temperature ($150\text{ }^\circ\text{C}$), which could be due to the loss of the residual alkane group from the uncompleted decomposition of the precursor. Also, its combustion analysis shows a $\sim 6.5\%$ nitrogen content, less than that of the sample prepared from CuF_2 route, suggesting the residue alkane attaching to the sample.

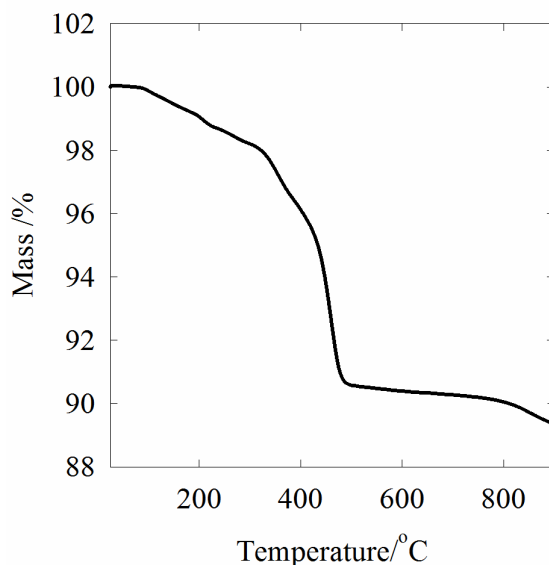


Figure 4.10 Thermogravimetric analysis (TGA) of Cu₃N produced from ammonolysis of copper(II) pivalate at 250 °C.

4.3 Electrochemical performance of copper nitride

The electrochemical performance of copper nitride in sodium and lithium -ion batteries was investigated in this work. Electrochemical testing used a Bio-Logic SP150 or MPG potentiostat. The working electrode consisted of a powdered mixture of 75% active material with 20% of acetylene black (Shawinigan, Chevron Phillips Chemical Co. LP) and 5% PVdF dissolving into cyclopentanone to form the ink, then dropping onto 50 μm copper foil.

4.3.1 Copper nitride as the negative electrode material for Na-ion batteries

Cyclic voltammetry of both samples show similar multiple reduction steps in the first reduction cycle and then gradually settled in the next cycles. A reduction peak appearing at around 0.2 V against Na was observed in CV graphs for both samples (Figure 4.11).

Pereira *et al.* proposed that the conversion of Cu₃N to Cu occurred at around 0.5 V

against Li in the first cycle.⁹ Hence, it can be extrapolated that the reduction peak at 0.2 V in Na cells could be corresponding to the conversion reaction, as the standard potential of sodium is around 0.3 V lower than that of lithium. It is interesting to see that with the cycle number increase, the oxidation peak at around 0.2 V increasingly grew. This could be due to the formation of the solid electrolyte interphase (SEI) layer at working electrode surface.

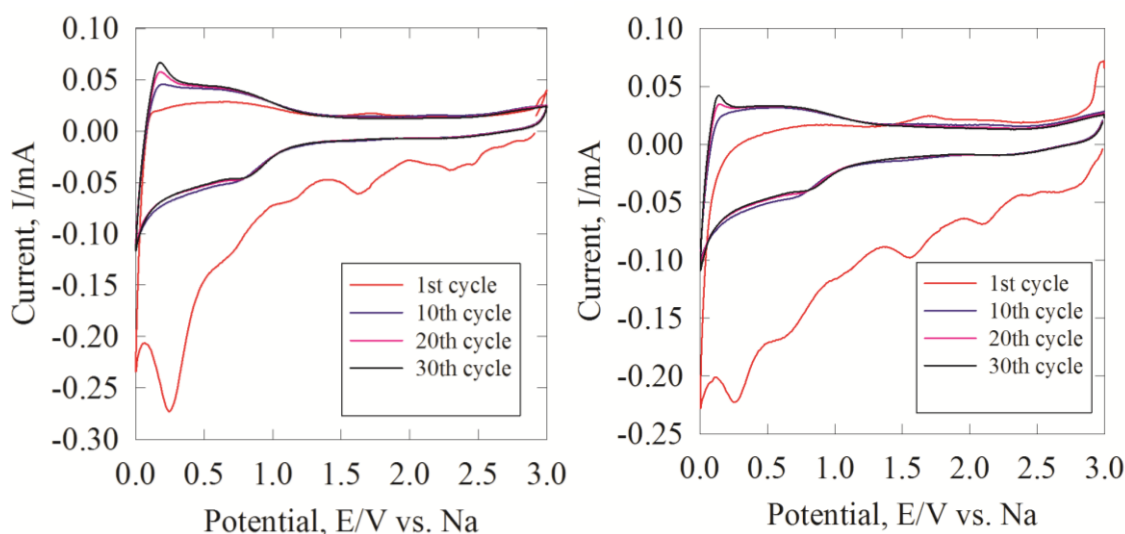


Figure 4.11 Cyclic voltammetry at 1 mV s^{-1} of Cu_3N derived from copper fluoride (left) and copper pivalate (right) at 1st, 10th, 20th and 30th cycle. The counter electrode and reference electrode is sodium metal foil and the electrolyte is 1M NaPF_6 in EC:DEC (1:1).

The behaviours of the two types of Cu_3N prepared in this study were compared with reduction/oxidation rates of 1 C (392 mA g^{-1}). The first reduction cycle shows a capacity of 277 mA h g^{-1} in copper pivalate derived Cu_3N and 210 mA h g^{-1} in copper fluoride derived Cu_3N , respectively. In both cases, the first cycle Coulombic efficiency is low, which could be attributed to the formation of SEI layer. Although a significant capacity drop is observed between the first and second reduction steps, it can be seen that the capacity quickly stabilises in both samples. In the higher surface area Cu_3N

derived from copper pivalate, the higher capacity decreased from 80 mA h g⁻¹ at 10th reduction cycle to 70 mA h g⁻¹ at 50th cycle, 88% capacity retention. The more crystalline CuF₂-derived Cu₃N still shows decent and stable capacity, from 51 mA h g⁻¹ at 10th reduction cycles to 49 mA h g⁻¹ at 50th cycle, only around 4% capacity loss over 40 cycles. However, considering the entire cycling performance, further study focused on Cu₃N derived from copper pivalate in lithium and sodium ion batteries.

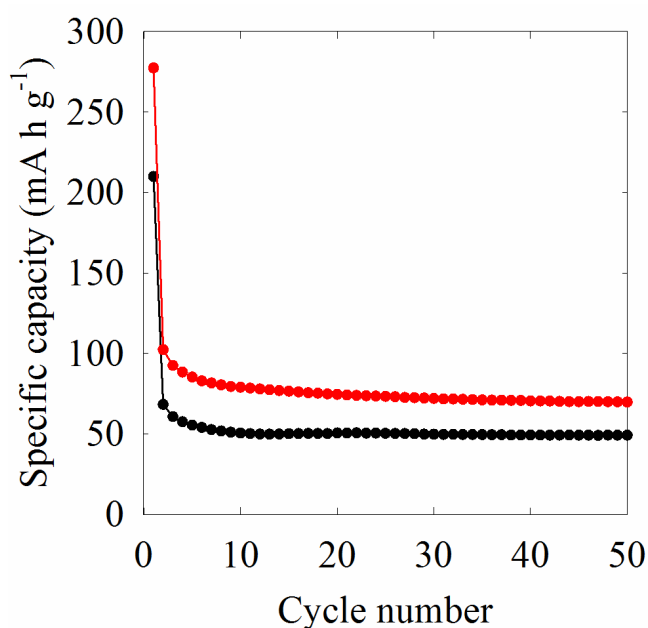


Figure 4.12 Reduction specific capacity versus cycle number of Cu₃N-sodium half cells using CuF₂-derived Cu₃N (black) and copper pivalate-derived Cu₃N (red) cycled between 1 mV and 3 V at 1C (392 mA g⁻¹) for 50 cycles. The counter electrode is sodium metal foil and electrolyte is 1M NaPF₆ in EC:DEC (1:1).

Galvanostatic testing of the copper(II) pivalate-derived Cu₃N at various rates shows a large irreversible reduction capacity in the first reduction (277, 343 and 485 mA h g⁻¹ at 1 C, 0.5 C and 0.1 C) which was followed by a much smaller amount of charge passed in the first re-oxidation (102, 117 and 133 mA h g⁻¹). Apart from this low Coulombic

efficiency in the first cycle, it is similar to the results of Ni_3N in Na-ion cells. The specific capacity is always greater at lower reduction/oxidation rates, e.g. the first reduction capacity was 485 mA h g^{-1} at 0.1 C, which was approximately twice as that at 1 C (277 mA h g^{-1}). However, unlike nickel nitride, Cu_3N derived from copper pivalate shows a rapid stabilisation in the reduction/oxidation over the first few cycles, with much smaller changes observed in both the reduction (discharge) and the oxidation (charge) processes and efficiency close to 100% from the second cycle onwards. Reduction capacities in the 2nd cycle were 102 (1 C), 117(0.5 C) and 133 (0.1 C) mA h g^{-1} while those in the 50th cycle were 70 (1 C), 87 (0.5 C) or 89 (0.1 C) mA h g^{-1} using a 3V cut-off, which indicates only around 30% capacity loss since the second cycle.

When calculating the specific capacity from the cut-off voltage to 2 V, it can be observed that the large proportion of reduction capacity remained. 261 (1 C), 311 (0.5 C) and 407 (0.1 C) mA h g^{-1} were retrieved in the 1st cycle, dropping to 66 (1 C), 82(1 C) or 85 (1 C) mA h g^{-1} in the 50th cycle. However, it is interesting to see that the oxidation profile slopes were more even (58, 71 and 69 mA h g^{-1} in the 1st cycle, becoming 50, 65 or 65 mA h g^{-1} in the 50th cycle).

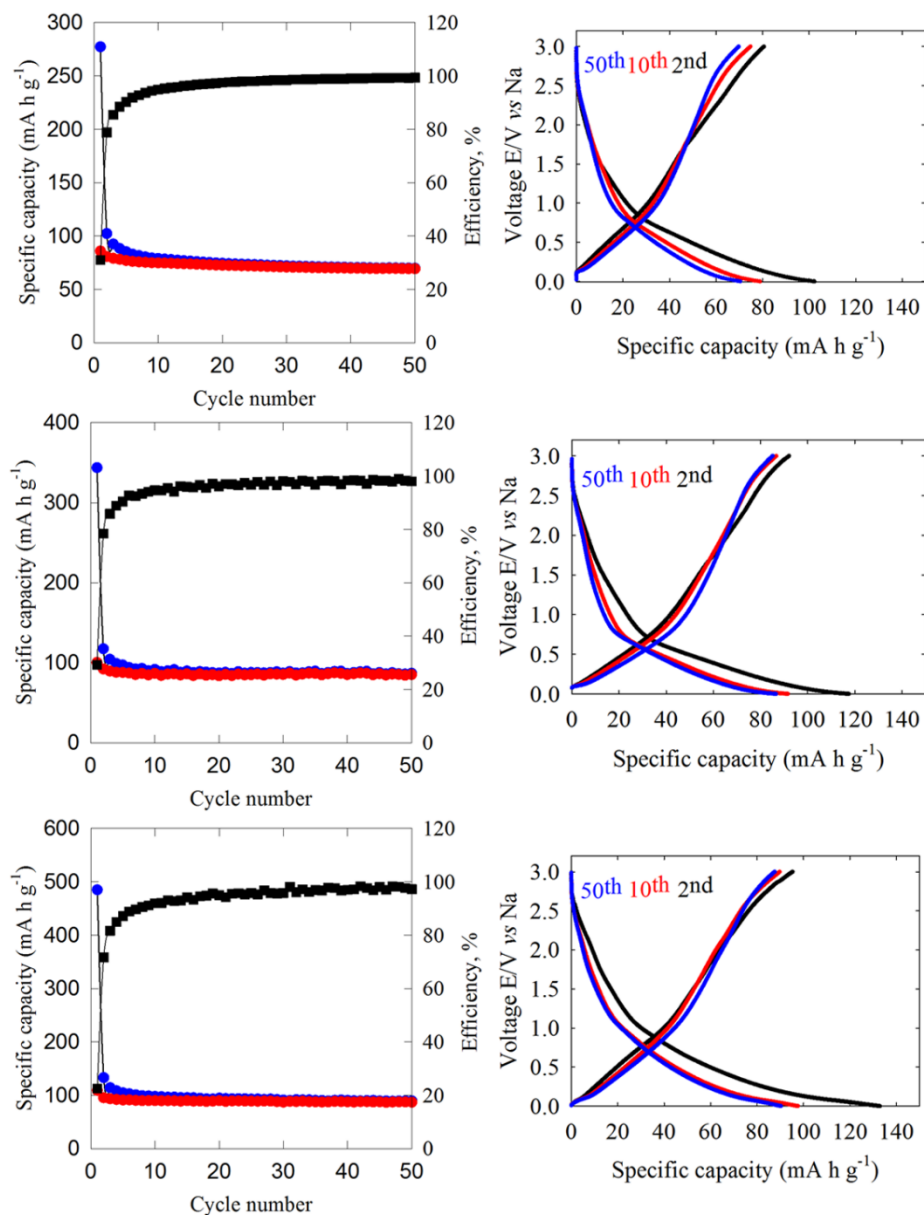


Figure 4.13 Specific capacity versus cycle number (left) and voltage profile in the 2nd, 10th and 40th cycles (right) of Cu₃N-sodium half cells cycled between 1 mV and 3 V at 1 C (392 mA g⁻¹, top), 0.5 C (196 mA g⁻¹, centre) and 0.1 C (39.2 mA g⁻¹, bottom). In the specific capacity vs cycle number plots blue circles show specific reduction capacity, red circles show specific oxidation capacity and black squares depict Coulombic efficiency.

As the real capacity of Cu₃N in sodium-ion batteries is still much lower than its

theoretical capacity based on conversion reaction, *ex situ* X-ray diffraction was recorded to explore the charge storage mechanism of this material. Since copper was expected to be one of the products of electrochemical reduction of Cu_3N , it was necessary to change the current collector used for *ex situ* X-ray diffraction. Titanium foil was found to deliver identical electrochemistry without obscuring the XRD features of interest. The diffraction pattern of a dried Cu_3N ink before any electrochemical treatment (Figure 4.14) exhibits peaks for Cu_3N and Ti metal. When reducing Cu_3N to a series of different cut-off voltages, reflections due to metallic copper were observed to appear. However, these reflections were not disappeared or diminished on oxidising back to 3 V as expected re-conversion reaction (oxidising Cu to Cu_3N) occurred. After 50 cycles Cu_3N and Cu were still presented in roughly the similar proportions, though the peaks were broadened somewhat suggesting the loss of crystallinity. In a previous study, Pereira *et.al.* evaluated Cu_3N in lithium-ion cells and found that with relatively large crystallites (~100 nm) complete conversion to Cu metal was observed.⁹ This may have been aided by lithium intercalation into the Cu_3N structure as observed through an expansion of the unit cell from $a = 3.81$ to 3.84 Å in the initial stages of reduction.⁹ Interestingly, they did not achieve full conversion back to Cu_3N either.

In this case, the Cu_3N lattice parameters were refined after collecting from SmartLab instrument. Specifically, before cycling, it was $a = 3.7655(5)$ Å; at 1 V, it was $3.8309(4)$ Å; at 0.5 V, $3.8226(5)$ Å; at 0.001 V, $3.8174(7)$ Å, after re-oxidising to 3 V, $3.8394(4)$ Å and after 50 cycles, $3.7928(5)$ Å. These variations likely indicate the scatter in the refined values due to the broad reflections and small amount of material measured. From *ex situ* XRD result, there is no compelling evidence for intercalation of sodium

ion into Cu_3N unit cell. It is likely that Cu_3N is mainly storing charge by a conversion mechanism, but that only a small proportion of the material is being converted, and that neither the reduction or the oxidation process is fully reversible even in that surface region of the particles. Based on the result above, it can be extrapolated that if the surface region (SEI layer) is responsible for much of the activity, it follows that smaller still particle sizes will provide larger capacities and optimization on SEI layer can be beneficial to its electrochemical performance.

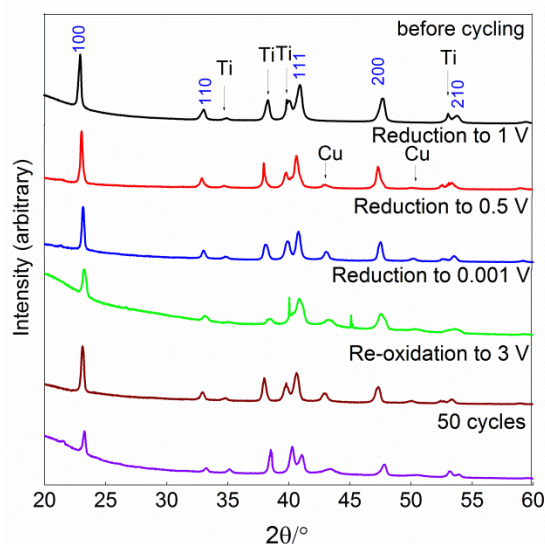


Figure 4.14 *Ex situ* XRD patterns of Cu_3N derived from copper pivalate cycled in sodium ion batteries. Reflections from the titanium current collector and the copper metal produced by reduction of Cu_3N are labelled; all other reflections are due to Cu_3N .¹⁹

4.3.2 Copper nitride as the negative electrode material for Li-ion batteries

As the Cu_3N derived from copper pivalate route had a smaller size than previously reported one by Pereira *et al.*,⁹ its electrochemical performance in lithium-ion batteries was also examined using a 1 M LiPF_6 in 1:1 EC:DMC electrolyte and lithium foil counter electrode.

From its CV graph, it can be found that a large sharp peak appeared at around 0.2 V which could be the formation of SEI layer, and a shoulder peak at 0.5 V which could be corresponding to converting Cu_3N to Cu .⁹ It had a large irreversible reduction charge in the first cycle, as observed in Na-ion cells. However, the charge stored in Li-ion cells was not quickly stabilized as found in Na-ion cells, instead the capacity gradually dropped during repeated scans.

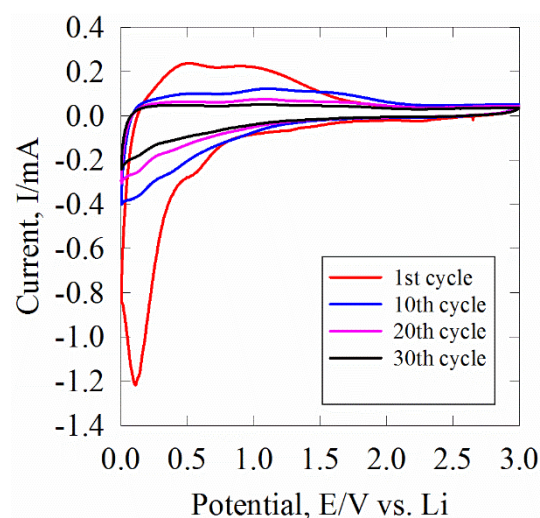


Figure 4.15 Cyclic voltammetry at 1 mV s^{-1} of Cu_3N derived from copper pivalate at 1st, 10th, 20th and 30th cycle. The counter electrode and reference electrode is lithium metal foil and the electrolyte is 1M LiPF_6 in EC:DMC (1:1).

The galvanostatic performance of Cu_3N derived from copper pivalate route in lithium half cells also shows similar cycle stability problems. As with sodium, a large irreversible reduction was observed in the first reduction cycle (Figure 4.16) and this gradually settled into a stable cyclic pattern with continuous capacity loss. From its voltage profile in both cases, a long plateau at approximately 0.5 V in the first reduction was observed, which is similar to that reported by Pereira *et al.*⁹ However, the capacity changes with extended cycling are very different. A much higher specific capacity was

observed in the beginning of cycling tests using Cu_3N derived from copper pivalate. Specifically, the first reduction capacity was 1135 mA h g^{-1} at 1 C and 1811 mA h g^{-1} at 0.5 C, respectively. The first oxidation capacity was 663 mA h g^{-1} at 1 C or 1082 mA h g^{-1} at 0.5 C, respectively. Then a gradual reduction in capacity to the 50th cycle (233 mA h g^{-1} at 1 C and 287 mA h g^{-1} at 0.5 C, respectively) was found. In contrast, Pereira *et al* found modest capacities in the early stages of cycling ($\sim 640 \text{ mA h g}^{-1}$ in the first reduction dropping to $\sim 250 \text{ mA h g}^{-1}$ after 20 cycles) but then a gradual increase to more than 300 mA h g^{-1} after 200 cycles. Their larger crystallites broke into smaller units as cycling progressed, whereas Cu_3N derived from pivalate was small from the beginning.

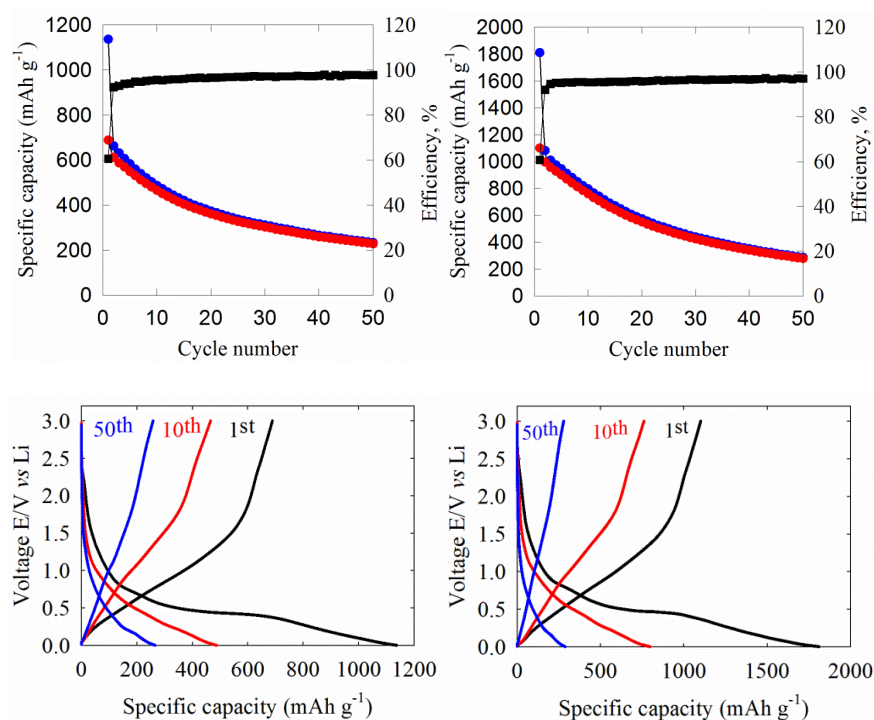


Figure 4.16 Voltage profile against specific cycles (bottom) and specific capacity versus cycle number profile (top) of Cu_3N -lithium half cells cycled between 1 mV and 3 V for cycles at 1 C (392 mA g^{-1} , left), 0.5 C (196 mA g^{-1} , right).

The differential capacity plot of Cu_3N derived from copper pivalate in lithium cells is

presented in Figure 4.17. At lower current rate, a minor reduction peak at around 0.8 V and a sharp peak near to 0.5 V were observed in the first cycle, which is similar to that published by Pereira *et al.*⁹ They attributed these electrochemical processes to the formation of the organic SEI layer and the reaction of Cu_3N with lithium. In the subsequent cycles, these peaks were diminished and a minor reduction peak formed at around 0.2 V which could be due to the development of the surface electrolyte layer storing the charge. In differential capacity plots, the effect of the current rate on the internal resistance loss can also be presented by the potential shift from 0.48 V at 0.5 C to 0.42 V at 1 C.

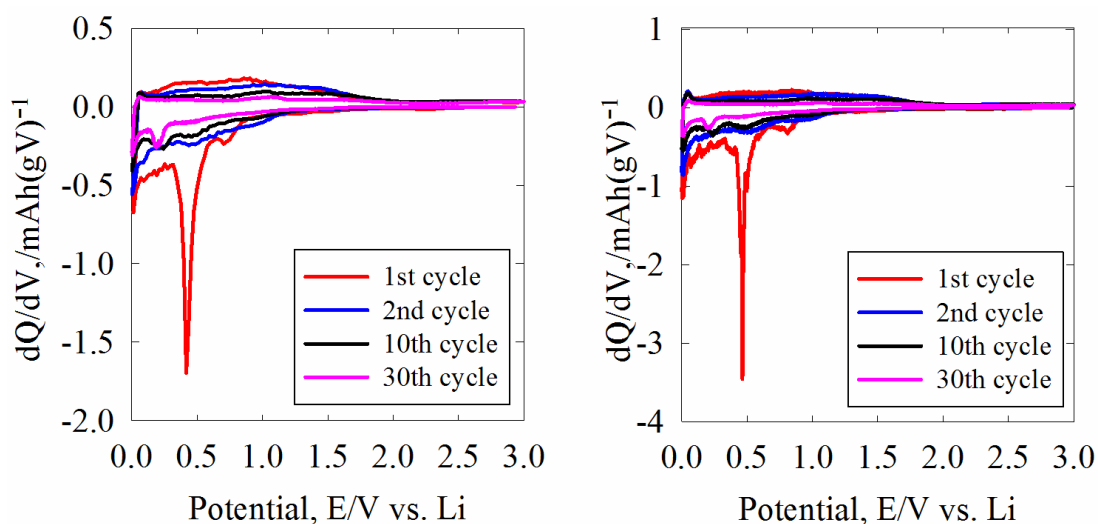


Figure 4.17 Differential capacity versus cell voltage of Cu_3N -lithium half cells using Cu_3N derived from copper pivalate route between 1 mV and 3 V at 1 C (392 mA g^{-1} , left), 0.5 C (196 mA g^{-1} , right). The counter electrode is lithium metal foil and the electrolyte is 1M LiPF_6 in EC:DMC (1:1).

4.3.3 CuO as the negative electrode material for Na-ion batteries

Sodium carboxymethyl cellulose (CMC) has been widely used in lithium ion batteries

due to a higher tolerance for volume changes during cycling.²⁴⁻²⁶ However, in an attempt to improve the electrode fabrication process by depositing from a water-based ink with carboxymethyl cellulose (CMC), the Cu_3N was inadvertently converted to CuO . The electrochemical performance of this CuO hydrolysed from Cu_3N was investigated in Na-ion cells.

It can be seen in Figure 4.18 that a large amorphous reduction peak appeared at around 0.2 V against Na which could be the conversion reaction of CuO to Cu_2O , or to Cu, and a broad reduction peak at 1.4 V which could be corresponding to the formation of SEI layer. There a large hump in the oxidation process around 2.3 V. Still, the irreversible charge stored in the first reduction process is similar to metal nitride materials studied before. However, the charge stored of CuO was not rapidly stabilized as Cu_3N in Na-ion cells, instead, the capacity gradually dropped during the scan.

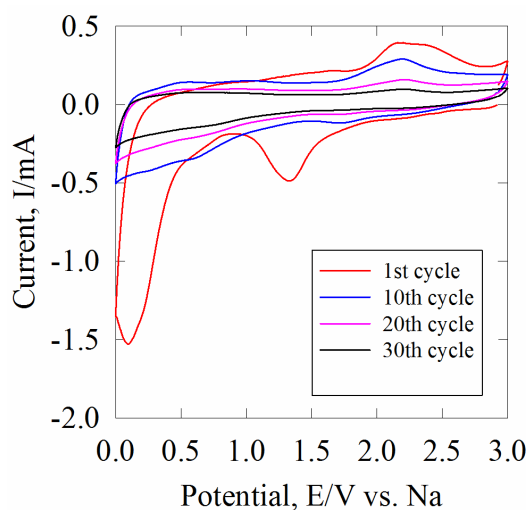


Figure 4.18 Cyclic voltammetry at 1 mV s^{-1} of CuO derived from hydrolysis of Cu_3N in the 1st, 10th, 20th and 30th cycle.

It can be found in Figure 4.19 that this material showed reasonably good electrochemical behaviours in Na-ion cells at a 196 mA g^{-1} cycling rate which is

equivalent to 0.29 C based on complete reduction of CuO to copper metal and Na₂O. Specifically, 795 mA h g⁻¹ specific capacity was retrieved in the first reduction cycle and 419 mA h g⁻¹ of this was recovered in the first oxidation. With more than 50% Coulombic efficiency in the first cycle, its Coulombic efficiency quickly reached around 100% after the first 2-3 cycles. However, the capacity gradually dropped, with 138 mA h g⁻¹ remaining in the 30th reduction cycle. Klein *et al* previously examined the performance of CuO in half cells vs sodium and observed a similar first reduction potential curve to that shown in Figure 4.16 (right), which exhibited a shorter plateau at 1.5-1.0 V and a lower first reduction capacity of ~600 mA h g⁻¹.²⁷ The plateau at ~0.5 V tailing down to 0 V is of similar shape and length. They only presented 5 reduction/oxidation cycles, but their capacities at this point were similar to the results of hydrolysed CuO from Cu₃N.

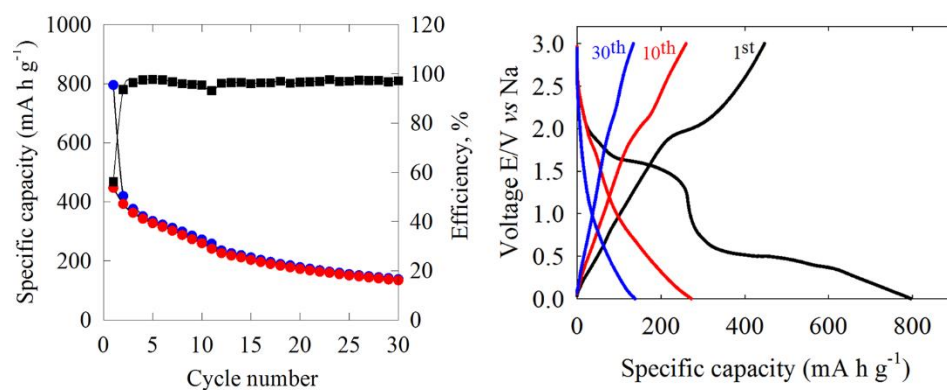


Figure 4.19 Voltage profile against specific cycles (right) and specific capacity for several different cycles (left) of CuO hydrolysed from Cu₃N-sodium half cells cycled between 1 mV and 3 V at 196 mA g⁻¹. Blue circles show specific reduction capacity, red circles show specific oxidation capacity and squares depict Coulombic efficiency.

In order to conduct deep understanding in the charge storage mechanism of CuO in

Na-ion cells, *ex situ* XRD data were collected on electrode foils in grazing incidence geometry using the SmartLab instrument. With reference to its voltage profile, a cut-off voltage was set at 0.8 V against Na foil, just below the first plateau in the reduction profile shown in Figure 4.19 (right). It is interesting to see that the Cu₂O XRD patterns were observed when reducing to 0.8 V. These Cu₂O reflections were the explanations of the plateau appearing above 0.8V observed in its voltage profile. With further reduction, Cu₂O reflections diminished while broad Cu reflections were found. This indicated that when reduced to 1 mV, CuO was completely reduced to Cu. The changes in the active materials after the first plateau showed that this plateau was not due solely to SEI formation, but to conversion reaction. In addition, the broad Cu peaks relative to the sharper peaks of the CuO starting material showed a reduction in crystallite size during this electrochemical process. When oxidising to 3V, the patterns were mixed with the reflections of CuO, Cu₂O and Cu, which also indicated that the conversion reaction of CuO in Na-ion cells was not a completely reversible process. The *ex situ* XRD results of CuO in Na-ion cells were similar to that in lithium cells, where the reduction of CuO results in complete conversion to Cu₂O with partial conversion back to CuO observed on re-oxidation process.²⁷

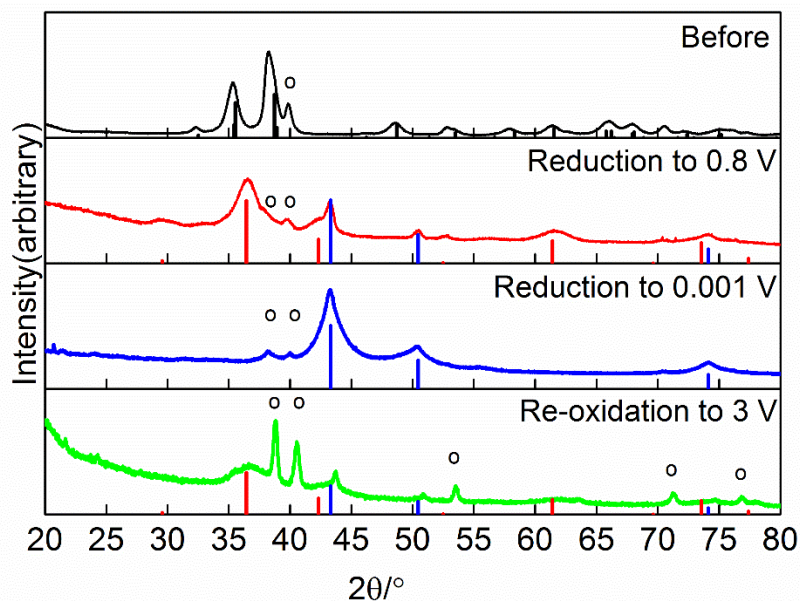


Figure 4.20 *Ex situ* XRD of CuO derived from oxidation of copper nitride reduced at 0.1C to different voltages in the first cycle. The black vertical lines show the standard positions of CuO reflections, the red of Cu₂O, and the blue of Cu metal.¹⁹ Open circles show the positions of reflections from the Ti substrate. Lattice parameters CuO (before reduction) $a = 4.6831(18)$, $b = 3.4132(14)$, $c = 5.1102(18)$ Å, Cu₂O (0.8 V) $a = 4.253(3)$ Å, Cu (0.001 V) $a = 3.636(3)$ Å.

4.4 Conclusions

Cu₃N was synthesized from ammonolysis of anhydrous copper fluoride and copper(II) pivalate. These two samples were compared with different characterization techniques, and the one derived from pivalate route showed a larger surface area and smaller particle size. Better electrochemical performance was also achieved by using Cu₃N derived from the ammonolysis of copper(II) pivalate. And it exhibits a competitive negative electrode behaviour in sodium-ion cells. After an initial conditioning period the capacity is reversible and is stable over 50 cycles at rates between 1 C, 0.5 C and 0.1 C, with 89 mA h g⁻¹ observed on the 50th cycle at 0.1 C. *Ex situ* XRD shows the formation of metallic

copper in the first cycle but the reflections of metallic copper did not diminish after re-oxidizing to 3 V, which indicates the conversion reaction from Cu_3N to Cu is not a completely reversible process. Cu_3N is retained throughout and hence the reactions appear to take place mainly at the surface of the electrode.

Furthermore, this Cu_3N provided similar electrochemical performance in lithium-ion cells to that reported previously, with 287 mA h g^{-1} on the 50th cycle at 0.5 C. Exposure to water resulted in hydrolysis and the formation of CuO, which offered larger initial capacities in sodium cells but was less stable during cycling, with 138 mA h g^{-1} on the 30th cycle at 0.29 C. In these cells CuO was reduced to Cu_2O and then to Cu metal, with partial re-oxidation to Cu_2O and copper metal on oxidizing back to 3 V.

4.5 Reference

1. M. Asano, K. Umeda and A. Tasaki, *Jpn. J. Appl. Phys. Part 1*, 1990, 29, 1985.
2. T. Maruyama and T. Morishita, *Appl. Phys. Lett.*, 1996, 69, 890.
3. D. M. Borsa, S. Grachev, C. Presura and D. O. Boerma, *Appl. Phys. Lett.*, 2002, 80, 1823.
4. L. Maya, *J. Vac. Sci. Technol.*, 1993, 11, 604.
5. D. M. Borsa and D. O. Boerma, *Appl. Surf. Sci.*, 2004, 548, 95.
6. R. Juza and H. Z. Hahn, *Anorg. Allg. Chem.*, 1939, 241, 172.
7. K. J. Kim, J. H. Kim and J. H. Kang, *J. Cryst. Growth*, 2001, 222, 762.
8. J. Pinkas, J. C. Huffman, D. V. Baxter, M. H. Chisholm and K. G. Caulton, *Chem. Mater.*, 1995, 7, 1589.
9. N. Pereira, L. Dupont, M. Tarascon, J. C. Klein, L. and G. Amatucci, *J. Electrochem. Soc.*, 2003, 150, A1273.
10. J. Choi and E. G. Gillan, *Inorg. Chem.*, 2005, 44, 7385.

11. H. Wu and W. Chen, *J. Am. Chem. Soc.*, 2011, 133, 15236.
12. R. Juza and H. Hahn, *Z. Anorg. Allg. Chem.*, 1938, 239, 282.
13. U. Hahn and W. Weber, *Phys. Rev. B*, 1996, 53, 12684.
14. U. Zachwieja and H. Jacobs, *J. Less. Common. Met.*, 1991, 170, 185.
15. G. Paniconi, Z. Stoeva, H. Doberstein, R. I. Smith, B. L. Gallagher and D. H. Gregory, *Solid State Sci.*, 2007, 9, 907.
16. N. Pereira, L. Dupont, J. M. Tarascon, L. C. Klein and G. G. Amatucci, *J Electrochem. Soc.*, 2003, 150, A1273.
17. D. R. Ketchum and J. W. Kolis, *J. Cryst. Growth*, 2001, 222, 431.
18. H. M. Rietveld, *J. Appl. Cryst.*, 1969, 2, 65.
19. Inorganic Crystal Structure Database (ICSD, Fiz Karlsruhe) accessed via the National Chemical Database Service hosted by the Royal Society of Chemistry.
20. L. Maya, *J. Vac. Sci. Technol. A*, 1993, 11, 604.
21. C. Navío, J. Alvarez, M. J. Capitan, J. Camarero and R. Miranda, *Appl. Phys. Lett.*, 2009, 94, 3112.
22. G. Paniconi, PhD thesis PhD thesis, University of Nottingham 2012.
23. A. Leineweber, H. Jacobs and S. Hull, *Inorg. Chem.*, 2001, 40, 5818.
24. J. Li, R. B. Lewis and J. R. Dahn, *Electrochem. Solid-State Lett.*, 2007, 10, A17.
25. S.-L. Chou, X.-W. Gao, J.-Z. Wang, D. Wexler, Z.-X. Wang, L.-Q. Chen and H.-K. Liu, *Dalton Trans.*, 2011, 40, 12801.
26. M. Mancini, F. Nobili, R. Tossici, M. Wohlfahrt-Mehrens and R. Marassi, *J. Power Sources*, 2011, 196, 9665.
27. F. Klein, B. Jache, A. Bhide and P. Adelhelm, *Phys. Chem. Chem. Phys.*, 2013, 15, 15876.

Chapter 5. Tin nitride as the negative electrode material for sodium-ion and batteries

5.1 Introduction

With the recent improvements in the negative electrode materials in sodium-ion and lithium-ion batteries, a series of compounds can store charge in a hybrid mechanism combining conversion and alloying/de-alloying process in battery applications. In this hybrid mechanism, the electrode material was firstly reduced to metal via conversion reaction and then alloyed with Na/Li ions to store the charge. Comparing to traditional electrode materials, these compounds can offer a higher theoretical capacity by combining two mechanisms, e.g. Sb_2S_3 : 946 mA h g^{-1} ,¹ SnO_2 : 1378 mA h g^{-1} ,²⁻⁴ Sn_4P_3 : 1132 mA h g^{-1} ,^{5,6} SnS : 1022 mA h g^{-1} .^{7,8} In reality, although the theoretical capacity cannot be fully retained through the cycling, the retained capacity can be satisfactory for Na-ion batteries. For example, Sb_2S_3 with graphene was shown by Yu *et al.* to exhibit a reversible capacity of 670 mA h g^{-1} at 50 mA g^{-1} over 50 cycles and an initial Coulombic efficiency of 69%.¹ SnO_2 with graphene studied by Su *et al.* showed a stable cycling performance with above 600 mA h g^{-1} capacity at 20 mA g^{-1} over 100 cycles.⁴ However, due to the poor conductivity of oxides and sulphides, most of them required to mix with extra carbonaceous materials, such as reduced graphene oxide or carbon, to increase the conductivity.

Combining the performance of nitrides and the published conversion-alloy materials in Na-ion cells,⁵⁻⁹ tin nitride has a great potential to be a competitive negative electrode

material in Na-ion cells. The electrochemical performance of tin nitride as thin film in lithium-ion batteries was examined by Park *et al.*¹⁰ and Baggetto *et al.*¹¹ Both of them proposed a two-step process combining conversion and alloy reaction. Baggetto showed that in the first insertion 7.4 Li atoms per Sn atom were inserted, but the capacity of Sn₃N₄ thin films decayed over 30 cycles. Also, a film with a 1:1 ratio of Sn:N had a high volumetric capacity (700 μAh cm⁻² μm⁻¹) and good cycle stability over 50 cycles.

Tin nitride thin films (SnN_x) have been synthesized by chemical vapour deposition (CVD), decomposition of *tetrakis*(diethylamido)tin,^{12, 13} and by magnetron sputtering.^{11, 14} It has been found that the crystallinity was poor when obtained under 300 °C.¹⁰ Bulk Sn₃N₄ was firstly prepared by pyrolysis of a tin amide imide polymeric precursor.¹⁵ The amide imide polymer was obtained from the reaction of tin(IV) bromide with potassium amide in liquid ammonia. The product was washed by exhaustive ammonia for several times but only 95% pure sample was recovered. Sn₃N₄ nanoparticles were obtained by a rapid synthesis from metathesis reaction under high pressure (350 °C and 2.5 GPa) and pure phase was obtained via washing with 3 M HCl.¹⁶ Baxter *et al.* proposed a molecular route to make metal nitrides.¹⁷ Metal nitrides in group 4, 5 or 6 with high oxidation states have been made using solution phase ammonolysis synthesis. Inspired by this work, tin nitride nanoparticles were synthesized from pyrolysis of a polymeric precursor formed from solution phase ammonolysis of tin amide and its electrochemical performance in lithium-ion as well as sodium-ion batteries was investigated.

5.2 Synthesis and characterization of tin nitride

5.2.1 Synthesis of Sn(NEt₂)₄

LiNEt₂ was prepared by reacting ~50 ml dry diethylamine with 500 ml ice cold 1.6 M ⁿBuLi in hexane (Aldrich) in a 1000 ml round bottom flask, filtering and drying the product under vacuum. LiNEt₂ (23 g, 0.3 mol) was added in to a 1000 ml round bottom flask inside the glove box and the flask assembly was sealed and transferred to fume hood and attached to a Schlenk line. Around 150 ml of dry ether and 100 ml of dry hexane was added to LiNEt₂ and stirred until the amide was dissolved. The dry solvents used in this work were dried by distillation from sodium/benzophenone and used freshly. ~8.9 ml of SnCl₄ (0.075 mol) was dissolved into 50 ml of hexane in a 250 ml round bottom flask under nitrogen. SnCl₄ solution was then added dropwise to the ice cold LiNEt₂ slurry via a cannula. The mixture was left stirring overnight. The clear pale yellow solute was transferred to a 500 ml round bottom flask via a cannula under nitrogen. The solvent was stripped off under vacuum until only the light brown oil was left in the flask without bubbling. The reaction can be written below:



This *tetrakis*(diethylamido)tin was characterized by NMR, which showed a distinct ethyl group with negligible impurities. (Figure 5.1) Several attempts have been conducted to remove the negligible impurities, e.g. by distillation, unfortunately without success. Its CHN composition was analysed by the combustion measurement. It showed the synthesized tin amide with 45.5% carbon, 9.5% hydrogen and 11.9% nitrogen, which is close to its theoretical CHN composition (47.2% C, 9.9% H and 13.7% N).

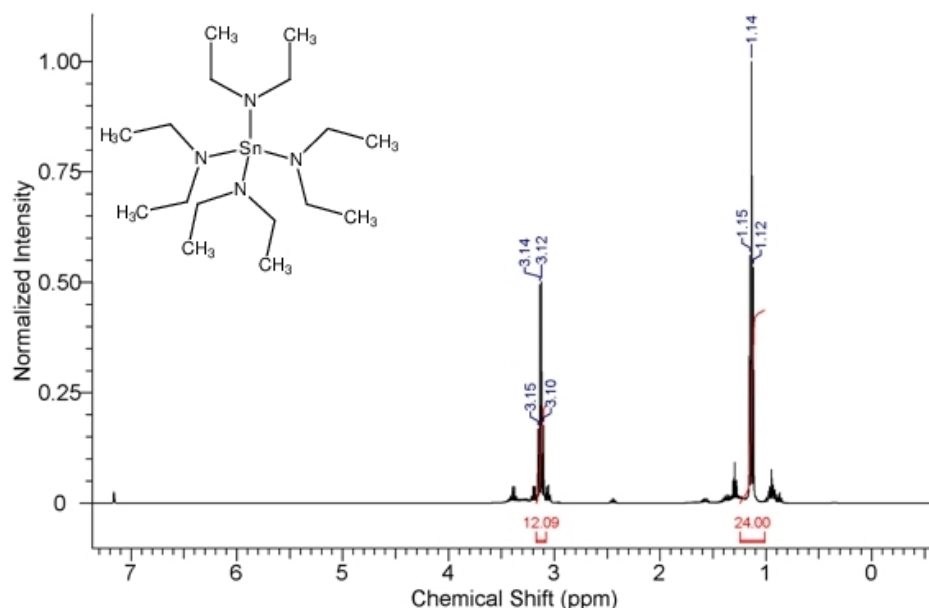
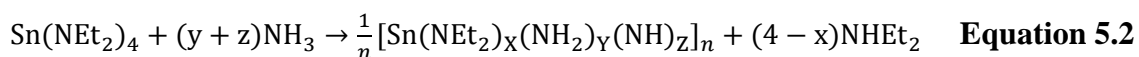


Figure 5.1 NMR spectra of as-synthesized tin diethylamide. The molecular structure is shown in the inset graph.

5.2.2 Solution phase ammonolysis of $\text{Sn}(\text{NEt}_2)_4$

The reaction was carried out using a Schlenk line. Liquid NH_3 (25 ml) was dried by condensing over sodium then distilled into a stirred 2 ml *tetrakis*(diethylamido)tin in dry THF (20 ml) solution at -78°C . The reaction mixture was left to warm to room temperature to evaporate the excess ammonia. The pale yellow precipitate of tin amide polymer, around 1.5 g, was then filtered and dried under vacuum. The likely reaction is given below:¹⁸



This polymeric tin amide precursor was characterized by CHN analysis which showed 10.3% carbon, 5.4% hydrogen and 14.2% nitrogen.

5.2.3 Ammonolysis of polymeric tin amide precursor

The polymer was transferred to a ceramic crucible (boat shape) inside a silica tube, which was loaded inside the glove box. The sample tube was then heated under flowing ammonia (BOC anhydrous grade, further dried with 3 Å molecular sieves) at 150 °C for 6 hours to stabilize the polymer, and then heated to 300, 350, or 400 °C at 2 °C min⁻¹ and maintained for 2 hours. The furnace tube was sealed with Teflon tape and had a bypass to allow flushing without exposing the sample to air. The product was collected and washed with 3 M HCl, followed by ethanol for 3 times. Pure phase Sn₃N₄ was obtained after washing.

Ammonolysis of polymeric tin amide precursor was carried out at 300, 350, or 400 °C with the aim of producing a small crystallite size and hence high surface area sample of Sn₃N₄. At 300 °C, two broad reflections were observed at around 33° and 55°, suggesting the poor crystallinity of this sample. This could presumably be due to some disordering in the anion vacancy.¹⁹ Its elemental analysis showed 2% carbon 0.1% hydrogen and ~7% nitrogen (13% N in theory), which could be due to the presence of incompletely reacted polymeric precursor left in the sample. Another possibility was that the minor tin metal was formed and left in the product which lowered the nitrogen content. With the increase of temperature, the sample changed to more crystalline proven by its sharper XRD reflections. Figure 5.2 shows that the tin metal reflections were observed at 350 °C and 400 °C, which is consistent with the work in high pressure synthesis published by Shemkunas *et al.*¹⁶ The pure phase Sn₃N₄ was obtained after washing with 3M HCl and ethanol. After washing, the impurities, e.g. residual polymeric precursor or tin metal, were removed, which is also certified by the CHN analysis of the sample obtained at

350 °C with washing showing 1.7% carbon, 0.1% hydrogen and 8.3% nitrogen.

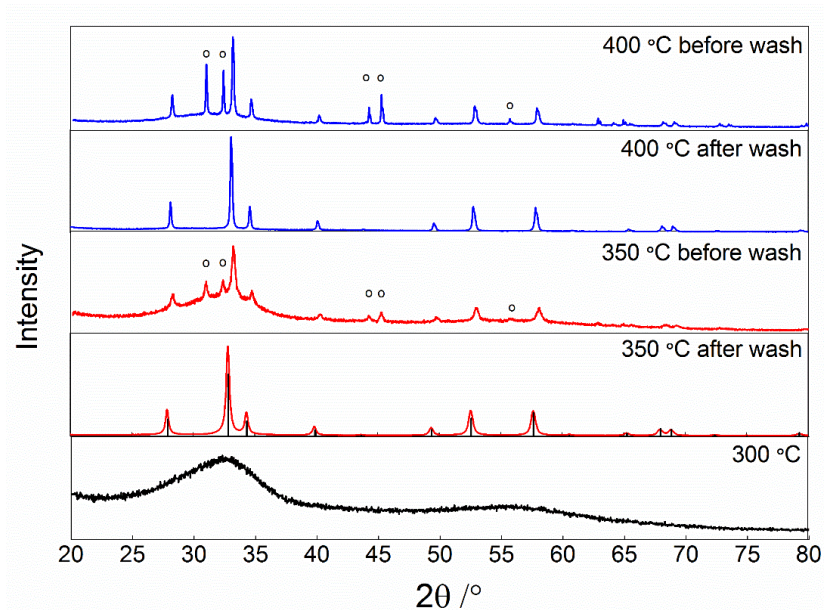


Figure 5.2 Powder XRD pattern of the products of ammonolysis of tin amide polymer at various temperatures (after washing). The round symbols denote the reflections of the tin metal and the stick pattern those of Sn_3N_4 .²⁰

The Rietveld fit of sample obtained at 350 °C after washing is shown in Figure 5.3.

Rietveld refinement of the diffraction data yielded lattice parameters of $a = 9.03716(5) \text{ \AA}$, which is extremely close to the value of $a = 9.037(3) \text{ \AA}$ published by Scotti *et al.* from neutron diffraction.²¹ A refined crystallite size of $32.2(1) \text{ nm}$ was calculated from the Lorentzian components of the profile fit.²²

TEM image (Figure 5.4) shows polycrystalline morphology of Sn_3N_4 with small spherical particles with average diameter of $\sim 30 \text{ nm}$ close to the crystallite size derived from XRD data. Also, it shows clustering of several crystallites in various area of the sample, which is similar to the tin nitride obtained from high pressure solid-state metathesis reaction.¹⁶

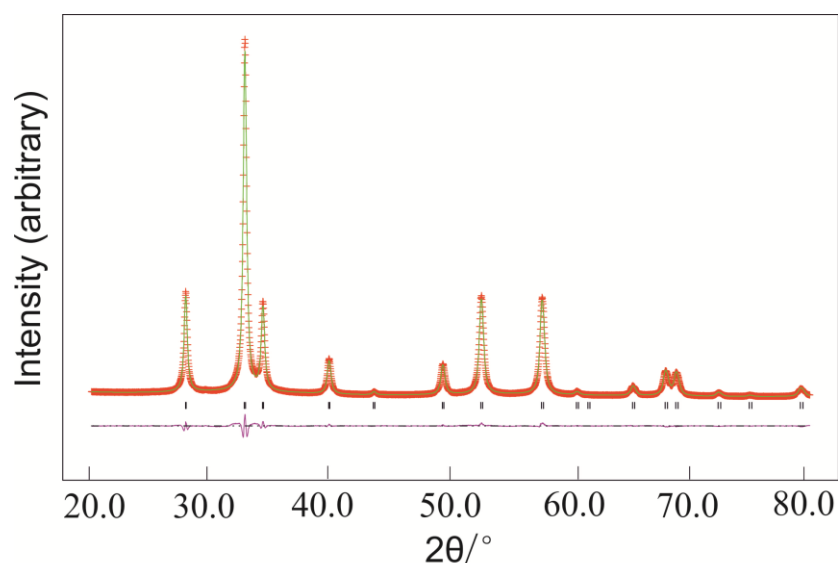


Figure 5.3 Rietveld fit ($R_{wp} = 3.6\%$, $R_p = 2.8\%$, $a = 9.03716(5)\text{\AA}$, crystallite size = $32.2(1)\text{ nm}$) to the PXD data for Sn_3N_4 produced from ammonolysis of the tin amide polymer at $350\text{ }^\circ\text{C}$ and washed with 3M HCl . Crosses mark the data points, the upper continuous line the fit and the lower continuous line the difference. Tick marks show the allowed positions of reflections for Sn_3N_4 with space group Fd-3m .²⁰

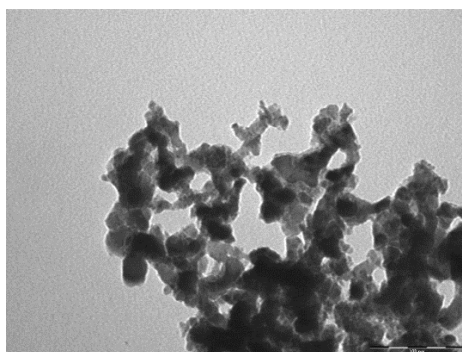


Figure 5.4 TEM image (scale bar = 100 nm) of Sn_3N_4 produced from ammonolysis of tin amide polymer at $350\text{ }^\circ\text{C}$ followed by washing with 3M HCl .

The infrared spectra of the samples obtained at $300\text{ }^\circ\text{C}$ and $350\text{ }^\circ\text{C}$ are compared in Figure 5.5. The sample prepared at $300\text{ }^\circ\text{C}$ has more amide and amine contents, according to the peaks at 3200 cm^{-1} $\nu(\text{NH})$ ¹⁷ and 1609 cm^{-1} $\delta(\text{NH}_2)$,^{17, 23} The M-N bond¹⁷ at around 550

cm^{-1} was also clearer in this lower temperature sample, presumably due to scattering by the Sn_3N_4 particles in the more crystalline sample. In both cases, there are low intensity peaks at $3030\text{-}2760\text{ cm}^{-1}$ attributed to $\nu(\text{CH})$.¹⁷ However, due to washing with 3M HCl, a residual hydroxide group is observed in both IR spectra at around 3400 cm^{-1} .¹⁷

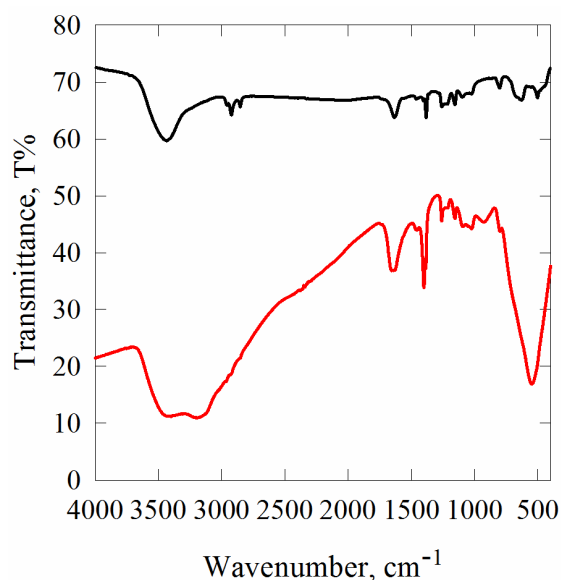


Figure 5.5 Infrared spectra of Sn_3N_4 obtained at $300\text{ }^\circ\text{C}$ (red) and $350\text{ }^\circ\text{C}$ (black).

When conducting the BET measurements on each sample, it is interesting to see that the one obtained at $300\text{ }^\circ\text{C}$ showed a specific surface area of $9\text{ m}^2\text{ g}^{-1}$ and the sample prepared at $350\text{ }^\circ\text{C}$ exhibited a largest specific surface area, $40\text{ m}^2\text{ g}^{-1}$ when washing with 3M HCl. The possible explanation is removing the extra tin metal by 3M HCl resulted in pores left in the sample. The sample obtained at $400\text{ }^\circ\text{C}$ has a specific surface area of around $9\text{ m}^2\text{ g}^{-1}$, lower than the one prepared at $350\text{ }^\circ\text{C}$, presumably due to the larger crystallite size observed in the XRD.

5.3 Electrochemical performance of tin nitride in Na-ion batteries

When preparing the ink composite with the sample obtained at $300\text{ }^\circ\text{C}$ which presumably

has the smallest crystallites, the ink could not be mixed homogeneously and was not found to produce a good thin layer on the copper foil substrate. Hence, considering the large surface area, the further studies of tin nitrides were mainly focused on the sample obtained at 350 °C.

Electrochemical testing used a Bio-Logic SP150 or MPG potentiostat. The working electrode consisted of a powdered mixture of 75% active material with 20% of acetylene black (Shawinigan, Chevron Phillips Chemical Co. LP) and 5% binder (Carboxymethyl cellulose (CMC) or alginate (Aldrich)) dissolving into deionized water to form the ink, then dropping the ink onto 50 µm thick and 10 mm in diameter copper foil disk.

Since Sn₃N₄ showed good stability in deionised water, water-based binders were selected to improve its electrochemical performance in battery applications. Carboxymethyl cellulose (CMC) has exhibited good ability to withstand the large volume changes during insertion/deinsertion of Li into Si or Sn electrode materials in lithium-ion batteries.²⁴⁻²⁷ It has also been shown to be beneficial for metal oxide materials which have a large volume change due to conversion reaction, e.g. Fe₂O₃.²⁸ In very recent work, sodium alginate showed better electrochemical performance in lithium-ion cells using Si²⁹ or Fe₂O₃³⁰ as negative electrode materials than that with CMC binder.

In this work, the Sn₃N₄ electrode with CMC binder was firstly investigated in sodium-ion batteries. The galvanostatic performance at different current rates is shown in Figure 5.6. In both cases, it showed a stable cycling performance after the first cycle. At 100 mA g⁻¹, around 420 mA h g⁻¹ capacity was passed in the first cycle and around 157 mA h g⁻¹ of that was recovered. The Coulombic efficiency in the first cycle is low (37%), which could be attributed to the irreversible process to form the SEI layer. Minor capacity loss was found

during the rest cycling and around 150 mA h g⁻¹ capacity was left in the 50th cycle. High internal resistance loss always comes with high current rate. When at a current rate of 200 mA g⁻¹, approximately 350 mA h g⁻¹ capacity was obtained in the first cycle, and 118 mA h g⁻¹ was recovered in the first oxidation cycle. After 50 cycles, around 110 mA h g⁻¹ capacity was left. It can be found that the real capacity is much lower than its theoretical capacity (1440 mA h g⁻¹) calculated from conversion and alloy reactions in Equation 5.3 and 5.4. This could be attributed to the fact that only surface portion of the tin nitride was involved in conversion reaction like the results of Cu₃N (Chapter 4).



From their voltage profiles, most of the capacity was virtually passed below 2 V region in reduction/ oxidation process. It can be predicted that with the lower current rate, the stable cycling performance can be maintained while the higher capacity can be obtained.

The differential capacity plots of Sn₃N₄ in sodium half cells using CMC binder at different current rates are shown in Figure 5.7. In both cases, multiple peaks were observed in the first reduction cycle, which could correspond to several electrochemical processes. The sharp peak in the first reduction cycle observed at around 0.4 V (200 mA g⁻¹) and 0.5 V (100 mA g⁻¹) could be attributed to the converting Sn₃N₄ to Sn. And the ones close to 0 V could be due to the alloying process of sodium with tin.⁵ In the first oxidation cycle, no oxidation peaks were found corresponding to the sharp reduction peaks in both cases, suggesting the conversion reaction could be an irreversible process. The cycling performance was stable afterwards. The peak position shifts observed in first

cycle at different current rates could be attributed to the different internal resistance losses resulted from current rates difference. As a result, in the first reduction cycle, the peak ~ 0.4 V at high current rate (200 mA g^{-1}) moved to ~ 0.5 V at low current rate (100 mA g^{-1}).

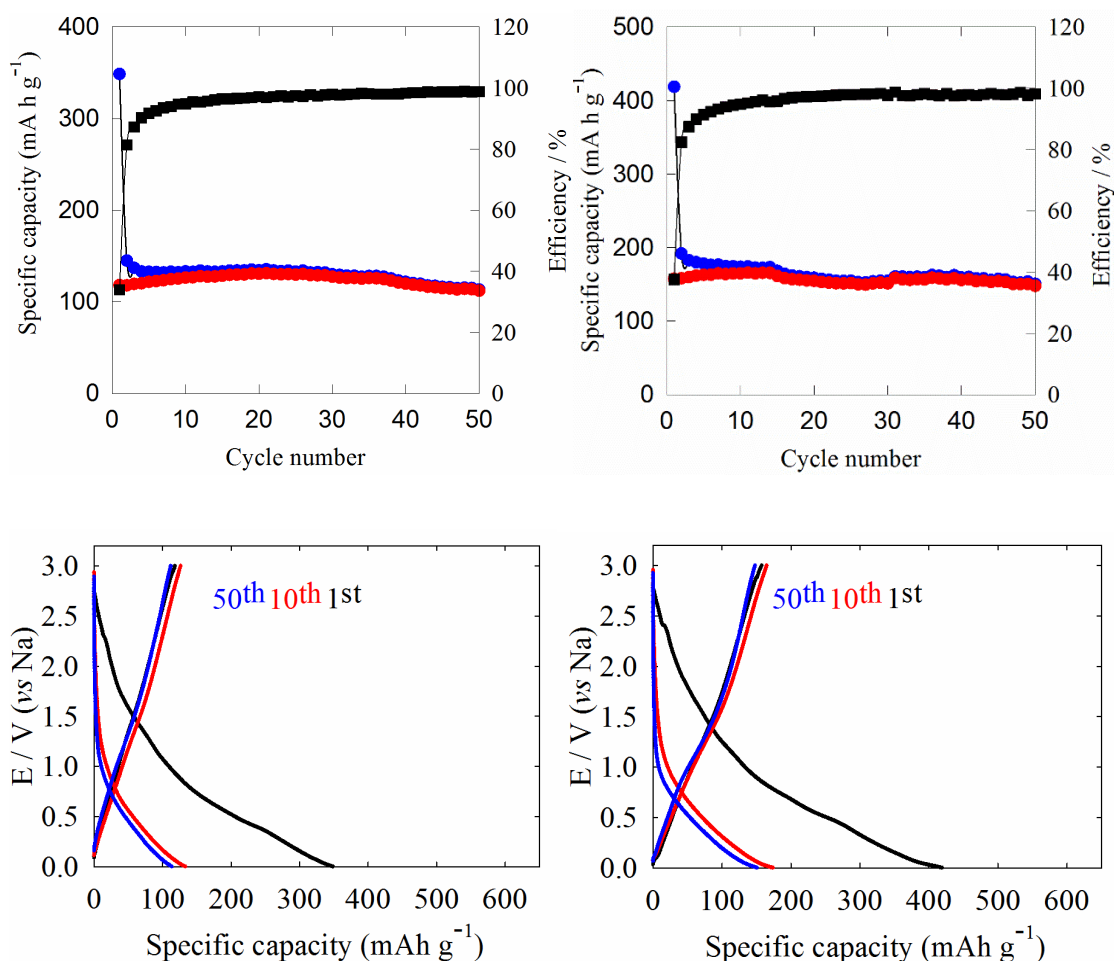


Figure 5.6 Voltage profile against specific cycles (bottom) and specific capacity versus cycle number profile (top) of Sn_3N_4 -sodium half cells cycled between 1 mV and 3 V using CMC binder for 50 cycles at 200 mA g^{-1} (left), 100 mA g^{-1} (right). In the specific capacity vs cycle number plots blue circles show specific reduction capacity, red circles show specific oxidation capacity and black ones depict Coulombic efficiency.

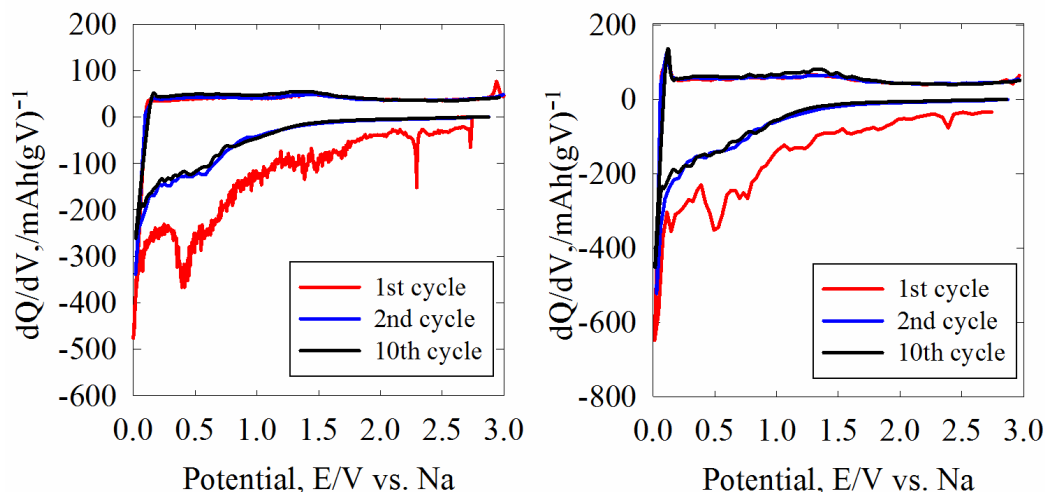


Figure 5.7 Differential capacity vs voltage of Sn_3N_4 -sodium half cells cycled between 1 mV and 3 V using CMC binder at 200 mA g^{-1} (left), 100 mA g^{-1} (right). The counter electrode is sodium metal foil and the electrolyte is 1 M NaPF_6 in EC:DEC (1:1).

In order to select an optimal binder for the further electrochemical work on Sn_3N_4 , the cycling performance of Sn_3N_4 -sodium half-cell using these two binders (CMC binder and alginate binder) was compared at 200 mA g^{-1} over 50 cycles. In general, the one using alginate binder showed higher capacity and more stable cycling performance than that using CMC binder. Specifically, the first reduction cycle exhibited around 539 mA h g^{-1} capacity of Sn_3N_4 with alginate binder and 348 mA h g^{-1} capacity with CMC binder. In both cases, the capacity dropped significantly after the first cycle, which could be due to the irreversible capacity loss in Na-ion cells. The two cells with different binders both showed stable cycling performance in Sn_3N_4 -sodium half cells. The one with alginate binder had a capacity of 175 mA h g^{-1} in the 2nd cycle and 155 mA h g^{-1} in the 50th cycle (89% capacity retention) while the cell with CMC binder showed a capacity of 144 mA h g^{-1} in the 2nd cycle and 113 mA h g^{-1} in the 50th cycle (79% capacity retention). The cell with alginate binder presented the higher specific capacity and better capacity retention.

These differences between the two binders were attributed to their chemical properties, in which alginate macromolecules were more polar and highly ordered carboxylic groups than the CMC polymer chains. These properties result in a better interfacial interaction between the alginate binder and the active materials, as well as stronger adhesion between the electrode layer and Cu substrate.²⁹ Hence, further investigation on electrochemical performance of Sn_3N_4 in battery applications will be conducted using the electrodes with alginate binder.

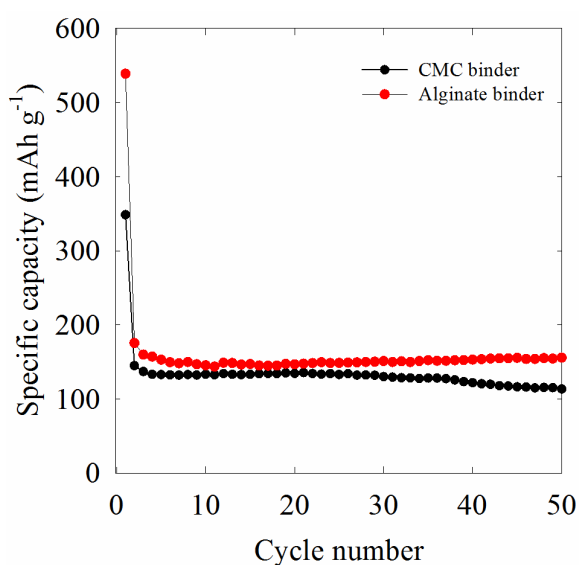


Figure 5.8 Reduction specific capacity versus cycle number of Sn_3N_4 -sodium half cells using CMC binder (black) and alginate binder (red) cycled between 1 mV and 3 V at 200 mA g^{-1} for 50 cycles. The counter electrode is sodium metal foil and electrolyte is 1 M NaPF_6 in EC:DEC (1:1).

The cyclic voltammetry of Sn_3N_4 with alginate binder in the sodium half-cell at 1 mV s^{-1} between 1 mV and 3 V is shown in Figure 5.9. During the first cycle, several reduction humps were observed above 2 V, which could be corresponding to the side reactions to form the SEI layer. A shoulder peak was observed at around 0.6 V and it rapidly decreased in the subsequent cycles. A broad oxidation peak was observed at around 1.5 V,

which could correspond to the minor reduction shoulder peak at around 1 V showing the conversion reaction of Sn_3N_4 . It can be seen that the cycle stability is reasonably good after the first cycle, though the electrochemical processes were not clearly presented due to the relatively quick scan rate (1 mV s^{-1}).

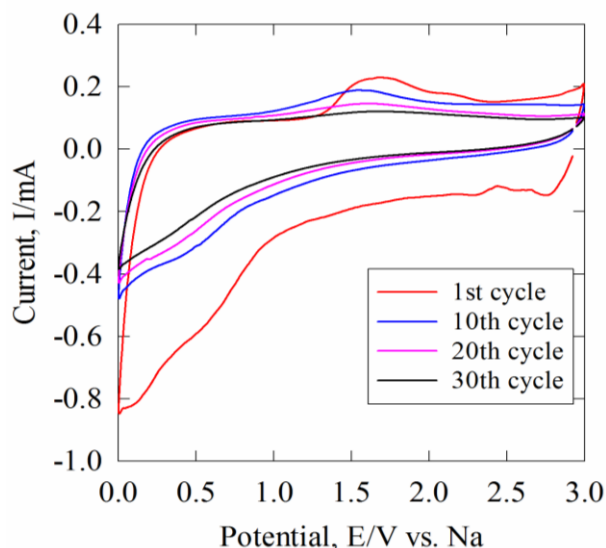


Figure 5.9 Cyclic voltammetry of Sn_3N_4 with alginate binder at 1st, 10th, 20th and 30th cycle. Scan rate is 1 mV s^{-1} . The counter electrode and reference electrode is sodium metal foil and the electrolyte is 1 M NaPF_6 in EC:DEC (1:1).

The galvanostatic performance of Sn_3N_4 -sodium half-cell using alginate binder was investigated at 200 mA g^{-1} for 50 cycles and 50 mA g^{-1} for 100 cycles. As with the cells using CMC binders, similar cycling trend was observed in the cells using alginate binder, e.g. low Coulombic efficiency in the first cycle and higher capacity achieved at lower current rate. A reduction capacity of 538 mA h g^{-1} capacity was obtained in the first cycle at 200 mA g^{-1} while 705 mA h g^{-1} was passed at a lower current rate (50 mA g^{-1}). The difference was also observed in their oxidation performance. Around 118 mA h g^{-1} capacity was recovered at 200 mA g^{-1} and more than 67% of that capacity (198 mA h g^{-1})

was achieved at 50 mA g^{-1} in the first oxidation cycle. It exhibited good capacity retention in both cases. At slow cycling rate (50 mA g^{-1}), 210 mA h g^{-1} reduction capacity was retrieved in the 20th cycle and it retained 190 mA h g^{-1} after 100 cycles, over 90% capacity retention. It also showed a good capacity retention in oxidation process. Around 198 mA h g^{-1} capacity was passed in the first oxidation cycle and 188 of that was remained at 100 cycles, over 95% capacity retention. Most of this was below 2 V , which is competitive to most negative electrode materials performance in Na-ion batteries.

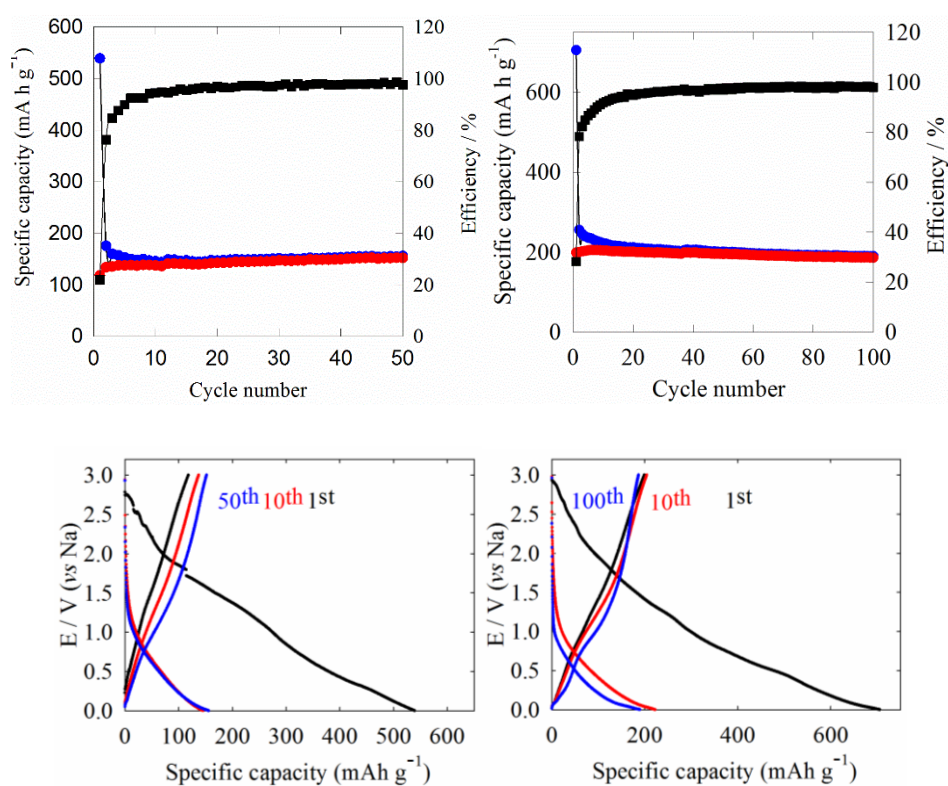


Figure 5.10 Voltage profile against specific cycles (bottom) and specific capacity versus cycle number profile (top) of Sn_3N_4 -sodium half cells cycled between 1 mV and 3 V using alginate binder for 50 cycles at 200 mA g^{-1} (left), 100 cycles at 50 mA g^{-1} (right). In the specific capacity vs cycle number plots blue circles show specific reduction capacity, red circles show specific oxidation capacity and black ones depict Coulombic efficiency.

The rate capability of Sn_3N_4 in sodium half-cell was explored at various current rates from 50 to 400 mA g^{-1} . It can be seen in Figure 5.11 that the Sn_3N_4 electrode can offer an average reversible capacity of around 216 mA h g^{-1} in the first 10 cycles at 50 mA g^{-1} , 190 mA h g^{-1} in the second 10 cycles at 100 mA g^{-1} , 164 mA h g^{-1} in the third 10 cycles at 200 mA g^{-1} , 127 mA h g^{-1} in the fourth 10 cycles at 400 mA g^{-1} and 220 mA h g^{-1} in the rest cycles at 50 mA g^{-1} . It is interesting to see that it can still deliver approximately 127 mA h g^{-1} reversible reduction capacity at the rate of 400 mA g^{-1} in the 40th cycle, which is around 55% of the capacity in the first 10 cycles at 50 mA g^{-1} . It can be seen that 220 mA h g^{-1} capacity remained after 40 cycles at 50 mA g^{-1} (110% capacity retention respect to first 10 cycles), which also suggests the good cycle stability of Sn_3N_4 as the negative electrode material in sodium-ion batteries.

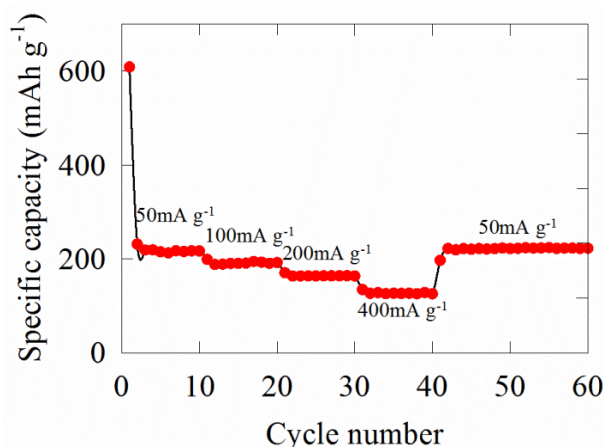


Figure 5.11 Rate capability of Sn_3N_4 in sodium half-cell at various current rates from 50 to 400 mA g^{-1} for 60 cycles.

In order to understand the charge mechanism of Sn_3N_4 in sodium-ion cells, *ex situ* XRD experiments were conducted and the patterns are shown in Figure 5.12. In all cycling stages, there are several minor peaks below 28° (Figure 5.12), which could be due to the residual electrolyte at the electrode surface.³¹ Upon the first reduction to 1 mV, it can be

seen that the intensity of Sn_3N_4 reflections decreased compared to the copper substrate peaks, suggesting that amorphous compounds were formed at the electrode surface. Also, a broad feature in the background was found near to 20° , which could be attributed to the amorphous Na-Sn alloy.⁵ On re-oxidation, the intensity of the broad background feature was diminished, which could correspond to the de-alloying process of sodium and tin. In the second reduction, no new crystalline peaks were found in the *ex situ* XRD graph and the intensity of Sn_3N_4 reflections became weak. In the *ex situ* XRD measurements, no distinct phase changes due to the conversion reaction or alloying/de-alloying process were observed, which could be attributed to the amorphous layer at the electrolyte surface. In the work on tin phosphide in Na-ion batteries by Kim *et al.*,⁵ the main Sn_4P_3 reflections were observed during reduction/oxidation in the *ex situ* XRD measurements. They attributed that phenomenon to the amorphous phases formed at the electrode surface.

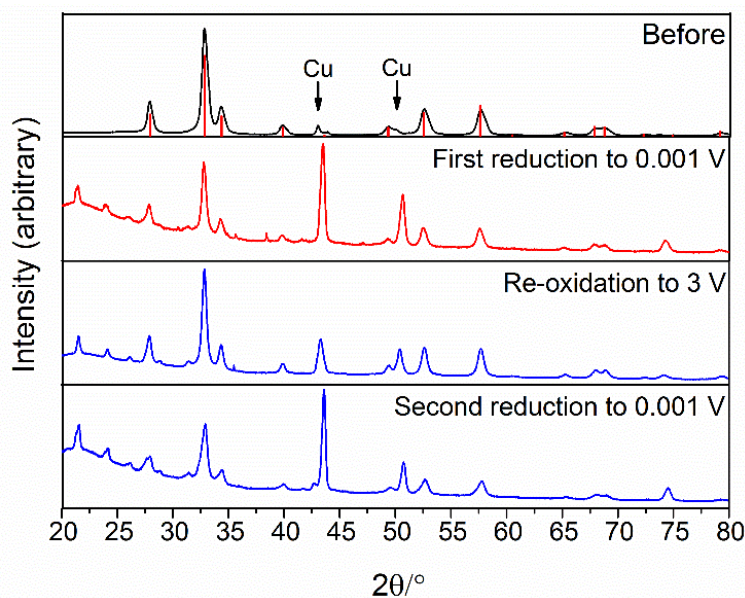


Figure 5.12 *Ex situ* XRD of Sn_3N_4 obtained at 350°C cycled at 50 mA g^{-1} to different stages in Na-ion batteries. Sn_3N_4 reflections are labelled in red tags and copper substrate peaks were denoted.²⁰

Fluorinated ethylene carbonate (FEC) additive is a well-known electrolyte additive that can form a passivation film to improve the cycling performance in lithium batteries.³²⁻³⁵ It was also found to be effective to improve the performance of Na-ion cells using hard carbon,³⁶ tin,³⁷ or antimony³⁸ as the negative electrode. It can compact SEI films, thereby withstanding the volume change of the alloy particles.

The effect of fluorinated ethylene carbonate (FEC) additive on the electrochemical performance of Sn₃N₄-sodium half cells was investigated. It is obvious from Figure 5.13 that with FEC additives, the specific capacity as well as cycle stability were much better than that without the additives. The first cycle exhibited 680 mA h g⁻¹ reduction capacity, 47% of which (320 mA h g⁻¹) was recovered in the second cycle. In contrast, without FEC additives, only 255 mA h g⁻¹ remained in the second cycle, which is only 35% of that in the first reduction cycle. Around 270 mA h g⁻¹ (85% capacity retention comparing with the capacity in the 2nd cycle) was obtained over 50 cycles in the cell with FEC additives, which is 35% higher than the capacity (~200 mA h g⁻¹) of the one without FEC additives. The reduction/oxidation cycling profile of the cell with FEC additives showed the first oxidation capacity was around 240 mA h g⁻¹, gradually increased to 258 mA h g⁻¹ in the 10th cycle, thereby the Coulombic efficiency close to 95%. The good performance of the cell with FEC additives could be attributed to the additive which can modify the SEI layer.³ And this modified layer is probably composed of stable alkali fluoride or fluoroalkyl carbonate, which could enhance the conductivity of SEI layer at the surface of the electrode.³⁸

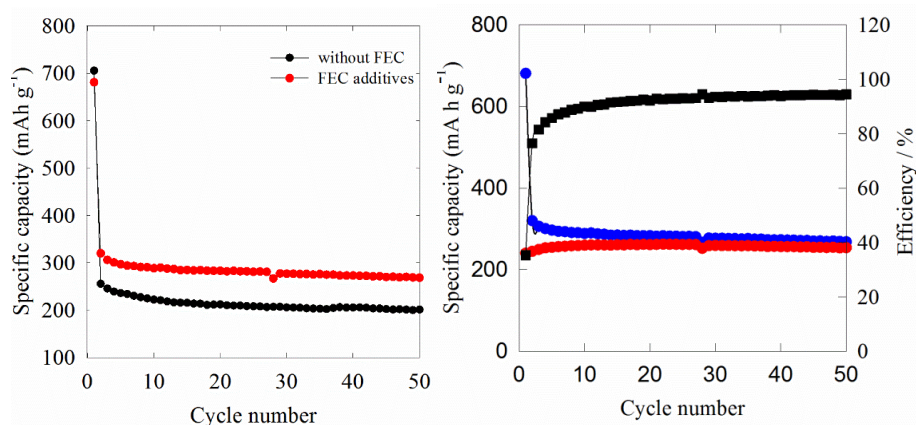


Figure 5.13 Reduction specific capacities versus cycle number (left) of Sn_3N_4 -sodium half cells in the electrolyte with 5% FEC (red) and without FEC (black) cycled between 1 mV and 3 V at 50 mA g^{-1} for 50 cycles. Specific capacity versus cycle number profile (right) of Sn_3N_4 -sodium half cells with 5% FEC additives cycled at 50 mA g^{-1} . In the specific capacity vs cycle number plots blue circles show specific reduction capacity, red circles show specific oxidation capacity and black ones depict Coulombic efficiency.

5.4 Electrochemical performance of tin nitride in Li-ion batteries

Tin nitride has shown a promising electrochemical performance as the negative electrode material in Na-ion batteries, however, its electrochemical performance in Li-ion cells was only investigated in thin film form.^{10, 11} Hence, in this work, the electrochemical performance of as-synthesized bulk Sn_3N_4 was explored in lithium-ion batteries.

It can be seen in Figure 5.14 that in the first reduction cycle, there is a large sharp peak at around 0.3 V and its corresponding oxidation peak at around 0.4 V, which could be assigned to the insertion/deinsertion of lithium into reduced tin metal.³⁹ A relatively small shoulder at around 0.7 V could be attributed to converting Sn_3N_4 into Sn. This

smaller shoulder disappeared in the subsequent cycles, which indicated this reaction is not a reversible process, further suggesting the main charge storage process of Sn_3N_4 in Li-ion batteries is alloying/de-alloying of reduced Sn with lithium. Hence, the likely reactions of Sn_3N_4 in Li-ion batteries can be described as follows and the theoretical capacity should be 1560 mA h g^{-1} .



In addition, it can be found that the redox peaks at around 0.3 V in the first cycle rapidly decayed in the subsequent cycles and hardly to be identified in the 30th cycle, which could indicate the poor cycle stability due to the large volume change of insertion/deinsertion of lithium into reduced tin metal.⁴⁰

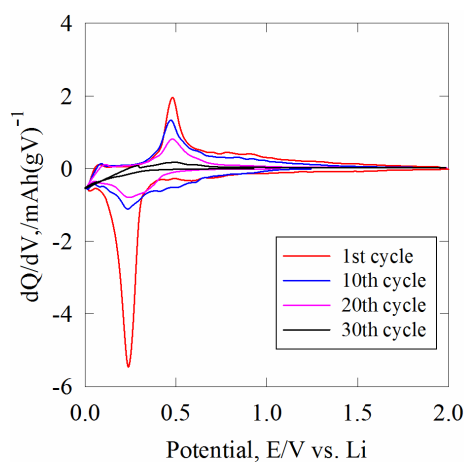


Figure 5.14 Differential capacity versus cell voltage at 200 mA g^{-1} of as synthesized bulk Sn_3N_4 with alginate binder in lithium-ion cells between 1 mV and 2 V in the 1st, 10th, 20th and 30th cycle. The counter electrode and reference electrode is lithium metal foil and the electrolyte is 1M LiPF_6 in EC:DMC (1:1).

The galvanostatic performance of Sn_3N_4 in lithium half cells was investigated at different current rates. It can be seen in Figure 5.15 that higher capacity (2600 mA h g^{-1}) in the first reduction cycle at 100 mA g^{-1} was achieved than that (1550 mA h g^{-1}) at 200 mA g^{-1} , which could be due to the lower IR drop at lower current rates. 2600 mA h g^{-1} capacity at 100 mA g^{-1} is higher than its theoretical capacity (1560 mA h g^{-1}), as is the second reduction capacity of 1660 mA h g^{-1} . However, in both cases, rapid capacity decay occurred during cycling, which could be attributed to the SEI film cracks and the electrode material falling off the copper substrate due to the large volume change of alloying/de-alloying. It can be also seen in its voltage profile that the plateau at 0.3 V diminished rapidly with cycle number. Hence, the stabilization of the SEI film could be a good solution to improve the electrochemical performance of Sn_3N_4 in lithium-ion batteries.

In order to understand the charge storage mechanism of Sn_3N_4 in Li-ion half-cells, *ex situ* XRD data were collected (Figure 5.16). Reduction to a cut-off voltage of 0.5 V just above the large voltage plateau in the reduction profile in Figure 5.15 (below), showed main reflections due to Sn_3N_4 and minor reflections due to Sn. Hence the conversion reactions were incomplete before the plateau. With further reduction, the reflections of Sn_3N_4 as well as Sn were diminished while the patterns of electrode materials changed to be amorphous, which is also observed in the Li-ion half-cells with tin electrodes.⁴¹ On oxidizing back to 2 V , broad reflections of Sn were observed in the XRD pattern, showing the de-alloying of lithium and recrystallization of Sn metal from amorphous Li-Sn alloying with no Sn_3N_4 formation. The *ex situ* XRD data show that the charge mechanism of Sn_3N_4 in lithium cells was mainly the alloying/de-alloying of lithium with tin while the

conversion reaction of Sn_3N_4 into Sn is not a fully reversible process.

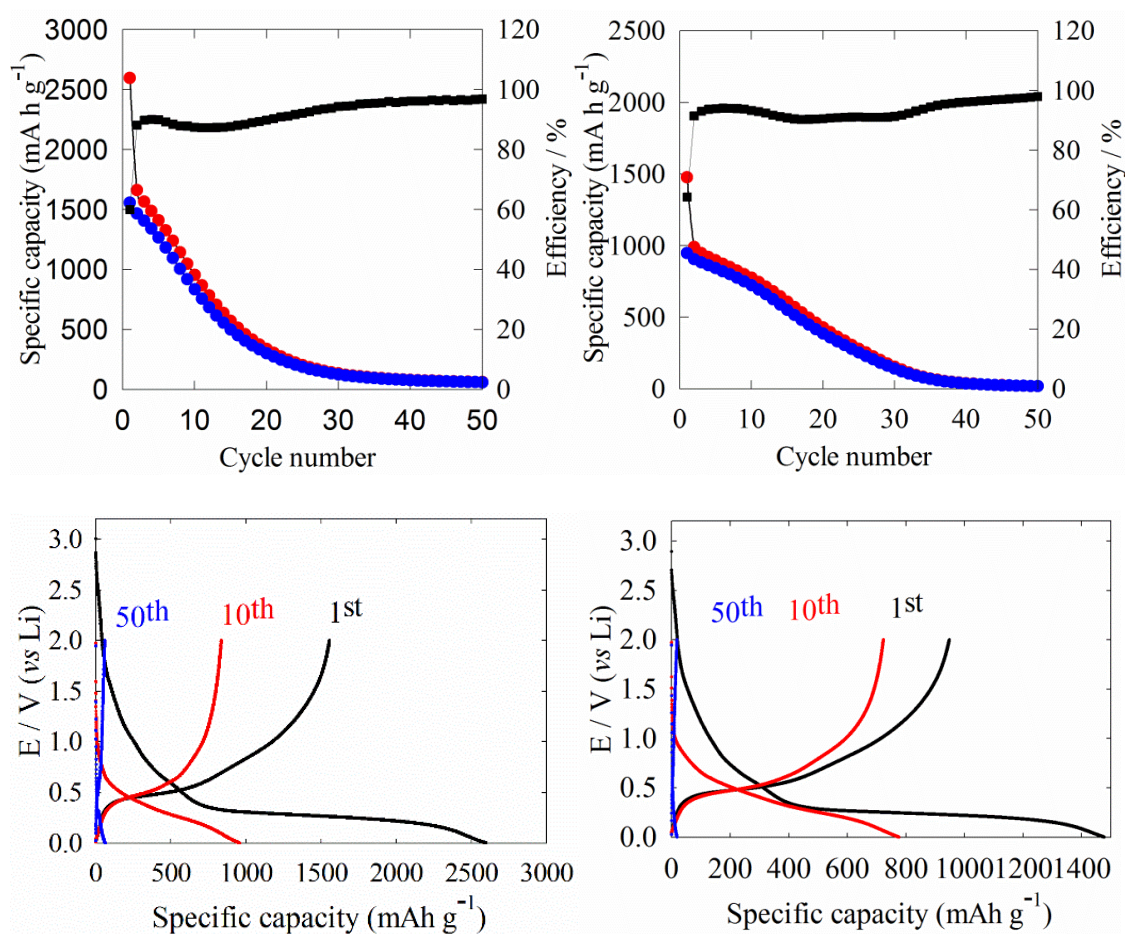


Figure 5.15 Voltage profile against specific cycles (bottom) and specific capacity versus cycle number profile (top) of Sn_3N_4 -lithium half cells cycled between 1 mV and 2 V for cycles at 100 mA g^{-1} (left), 200 mA g^{-1} (right). In the specific capacity vs cycle number plots red circles show specific reduction capacity, blue circles show specific oxidation capacity and black squares depict Coulombic efficiency.

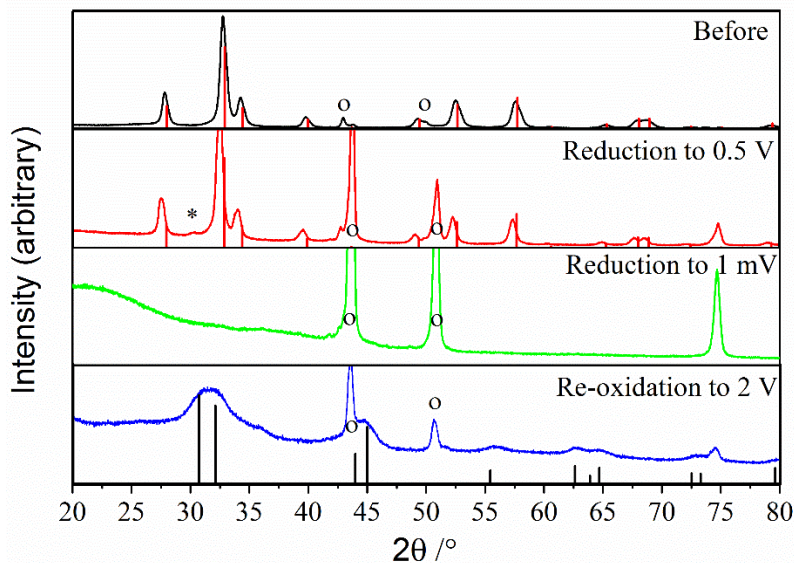


Figure 5.16 *Ex situ* XRD of Sn_3N_4 obtained at $350\text{ }^\circ\text{C}$ cycled at 100 mA g^{-1} to different voltages in the first cycle. The black vertical lines show the standard positions of Sn reflections and the red of Sn_3N_4 .²⁰ Open circles show the positions of reflections from the Cu substrate and asterisk symbol shows the position of the reflection from the Sn.

Fluorinated ethylene carbonate (FEC) additive has shown beneficial effects on the electrochemical performance of Sn_3N_4 -sodium half cells, in terms of the specific capacity and cycle stability. In lithium cells, with FEC additives, it exhibited similar reduction capacity in the first cycle (1540 mA h g^{-1}) to that without FEC additives (1470 mA h g^{-1}) at 200 mA g^{-1} . In contrast, the reduction capacity of the cell with FEC additives dropped rapidly to approximately 620 mA h g^{-1} in the 10th cycle while the capacity remained 770 mA h g^{-1} in the cell without FEC additives in 10th cycle. However, the capacity loss in the cell with FEC additives slowed down in the subsequent cycles comparing to the rapid capacity decay in the cell without FEC additives. In the 50th cycle, the remained capacity in the cell using FEC additives is

around 370 mA h g^{-1} (60% retention of the 10th cycle) while only 20 mA h g^{-1} (2.5% retention of the 10th cycle) left in the one without FEC additives.

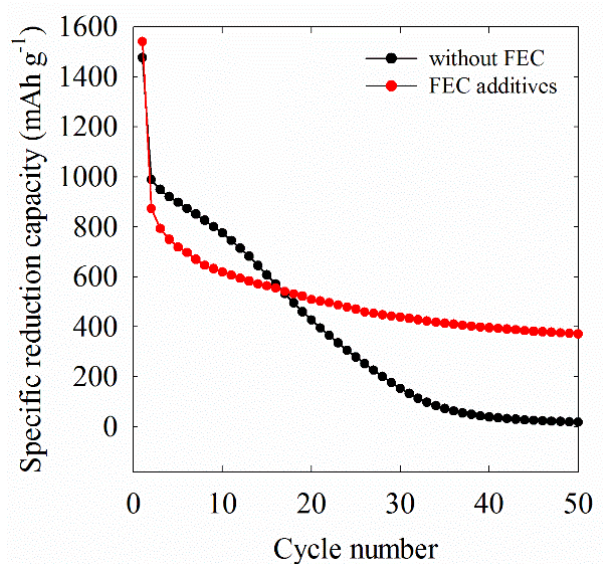


Figure 5.17 Reduction specific capacity versus cycle number of Sn_3N_4 -lithium half cells in the electrolyte with FEC (red) and without FEC (black) cycled between 1mV and 2V at 200 mA g^{-1} for 50 cycles. The counter electrode and reference electrode is lithium metal foil and the electrolyte is 1M LiPF_6 in EC:DMC (1:1).

The improvements of FEC additives in Sn_3N_4 -lithium half cells could be attributed to the modified SEI interphase formed at the surface of the electrode, which can be seen in Figure 5.18. Comparing to the differential capacity profile of the one without FEC additives, the one with FEC additives showed an extra couple of redox peaks at around 0.5 V after 20 cycles which could be due to the formation of the modified SEI film. Hence, the capacity stored due to the formed SEI film buffered the capacity decay due to the volume change Sn alloying/de-alloying processes. With FEC additives, the plateau at 0.3 V was stabilized with contrast to the cell without FEC additives.

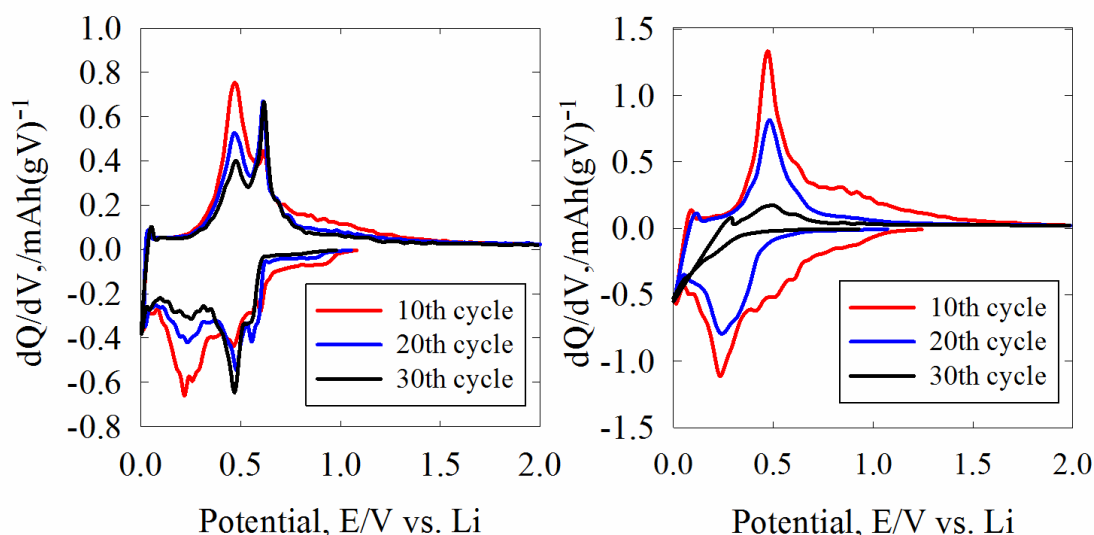


Figure 5.18 Differential capacity versus cell voltage at 200 mA g^{-1} of as synthesized bulk Sn_3N_4 between 1 mV and 2 V in the 10th, 20th and 30th cycle with FEC additives (left) and without FEC additives (right).

5.5 Conclusions

Bulk tin nitride was synthesized from ammonolysis of amide-derived precursor without high pressure. After washing with 3M HCl to remove tin, pure phase Sn_3N_4 was obtained. Samples obtained at $350 \text{ }^\circ\text{C}$ were observed to exhibit small particle size with the highest specific surface area among all samples. After characterization by different techniques such as XRD, TEM and IR, the sample derived at $350 \text{ }^\circ\text{C}$ was used to investigate its electrochemical performance in sodium- and lithium-ion batteries.

With several improvements conducted, e.g. binder and additives, Sn_3N_4 using alginate based binder showed a capacity of 680 mA h g^{-1} in the first cycle at 50 mA g^{-1} in the sodium-ion cells with FEC additives. Approximately 47% capacity (320 mA h g^{-1}) was

remained in the second cycle and the stable cycle performance (around 85% capacity retention compared to the reduction capacity in the 2nd cycle) was observed over 50 cycles, which is the best electrochemical performance in Na-ion cells using metal nitrides as negative electrode materials. This performance can be competitive to mostly current negative electrode materials in Na-ion batteries.

Bulk tin nitride was firstly investigated as the negative electrode material in Li-ion batteries. Comparing to the electrochemical performance of thin film tin nitride, bulk samples showed a similar voltage profile and higher capacity in the first cycles (1600 mA h g⁻¹ reversible capacity at 100 mA g⁻¹). However, the capacity decayed rapidly thereafter, which could be attributed to large volume change resulting from alloying/de-alloying of lithium with Sn. Herein, with the FEC additives help, the stability was largely improved and remained 370 mA h g⁻¹ capacity over 50 cycles at 200 mA g⁻¹.

5.6 Reference

1. D. Y. W. Yu, P. V. Prikhodchenko, C. W. Mason, S. K. Batabyal, J. Gun, S. Sladkevich, A. G. Medvedev and O. Lev, *Nat. Commun.*, 2013, 4, 2922.
2. Y. Wang, D. Su, C. Wang and G. Wang, *Electrochem. Commun.*, 2013, 29, 8.
3. Y.-X. Wang, Y.-G. Lim, M.-S. Park, S.-L. Chou, J. H. Kim, H.-K. Liu, S.-X. Dou and Y.-J. Kim, *J. Mater. Chem. A*, 2014, 2, 529.
4. D. Su, H.-J. Ahn and G. Wang, *Chem. Commun.*, 2013, 49, 3131.
5. Y. Kim, Y. Kim, A. Choi, S. Woo, D. Mok, N.-S. Choi, Y. S. Jung, J. H. Ryu, S. M. Oh and K. T. Lee, *Adv. Mater.*, 2014, 26, 4139.
6. J. Qian, Y. Xiong, Y. Cao, X. Ai and H. Yang, *Nano Lett.*, 2014, 14, 1865.

7. L. Wu, H. Lu, L. Xiao, J. Qian, X. Ai, H. Yang and Y. Cao, *J. Mater. Chem. A*, 2014.
8. B. Qu, C. Ma, G. Ji, C. Xu, J. Xu, Y. S. Meng, T. Wang and J. Y. Lee, *Adv. Mater.*, 2014, 26, 3854.
9. X. Li, M. M. Hasan, A. L. Hector and J. R. Owen, *J. Mater. Chem. A*, 2013, 1, 6441.
10. K. S. Park, Y. J. Park, M. K. Kim, J. T. Son, H. G. Kim and S. J. Kim, *J. Power Sources*, 2001, 103, 67.
11. L. Baggetto, N. A. M. Verhaegh, R. A. H. Niessen, F. Roozeboom, J.-C. Jumas and P. H. L. Notten, *J. Electrochem. Soc.*, 2010, 157, A340.
12. S. V. Nand, K. Ankur, K. Brijesh and M. B. Raj, *Solid State Sci.*, 2008, 10, 569.
13. R. G. Gordon, D. M. Hoffman and U. Riaz, *Mater. Res. Soc. Symp. Proc.*, 1991, 204, 95.
14. Y. Inoue, M. Nomiya and O. Takai, *Vacuum*, 1998, 51, 673.
15. L. Maya, *Inorg. Chem.*, 1992, 31, 1958.
16. M. P. Shemkunas, G. H. Wolf, K. Leinenweber and W. T. Petuskey, *J. Am. Ceram. Soc.*, 2002, 85, 101.
17. D. V. Baxter, M. H. Chisholm, G. J. Gama, V. F. DiStasi, A. L. Hector and I. P. Parkin, *Chem. Mater.*, 1996, 8, 1222.
18. S. I. U. Shah, A. L. Hector and J. R. Owen, *J. Power Sources*, 2014, 266, 456.
19. A. Salamat, A. L. Hector, B. M. Gray, S. A. J. Kimber, P. Bouvier and P. F. McMillan, *J. Am. Chem. Soc.*, 2013, 135, 9503.
20. Inorganic Crystal Structure Database (ICSD, Fiz Karlsruhe) accessed via the National Chemical Database Service hosted by the Royal Society of Chemistry.
21. N. Scotti, W. Kockelmann, J. Senker, S. Trassel and H. Jacobs, *Z. Anorg. Allg. Chem.*, 1999, 625, 1435.
22. H. M. Rietveld, *J. Appl. Cryst.*, 1969, 2, 65.
23. K. Nakamoto, ed., *Infrared and Raman Spectra of Inorganic and Organic*

Compounds 3rd ed, J. Wiley: New York, 1978.

24. B. Lestriez, S. Bahri, I. Sandu, L. Roué and D. Guyomard, *Electrochem. Commun.*, 2007, 9, 2801.
25. N. S. Hochgatterer, M. R. Schweiger, S. Koller, P. R. Raimann, T. Wöhrle, C. Wurm and M. Winter, *Electrochem. Solid-State Lett.*, 2008, 11, A76.
26. D. Mazouzi, B. Lestriez, L. Roué and D. Guyomard, *Electrochem. Solid-State Lett.*, 2009, 12, A215.
27. J. S. Bridel, T. Azaïs, M. Morcrette, J. M. Tarascon and D. Larcher, *Chem. Mater.*, 2009, 22, 1229.
28. J. Li, H. M. Dahn, L. J. Krause, D.-B. Le and J. R. Dahn, *J. Electrochem. Soc.*, 2008, 155, A812.
29. I. Kovalenko, B. Zdyrko, A. Magasinski, B. Hertzberg, Z. Milicev, R. Burtovyy, I. Luzinov and G. Yushin, *Science*, 2011, 334, 75.
30. P. S. Veluri and S. Mitra, *RSC Adv.*, 2013, 3, 15132.
31. J. C. Fitzmaurice, A. L. Hector and I. P. Parkin, *Polyhedron*, 1993, 12, 1295.
32. H. Nakai, T. Kubota, A. Kita and A. Kawashima, *J. Electrochem. Soc.*, 2011, 158, A798.
33. M. Kobayashi, T. Inoguchi, T. Iida, T. Tanioka, H. Kumase and Y. Fukai, *J. Fluorine Chem.*, 2003, 120, 105.
34. R. Mogi, M. Inaba, S.-K. Jeong, Y. Iriyama, T. Abe and Z. Ogumi, *J. Electrochem. Soc.*, 2002, 149, A1578.
35. R. McMillan, H. Slegel, Z. X. Shu and W. Wang, *J. Power Sources*, 1999, 81–82, 20.
36. S. Komaba, T. Ishikawa, N. Yabuuchi, W. Murata, A. Ito and Y. Ohsawa, *ACS Appl. Mater. Interf.*, 2011, 3, 4165.
37. S. Komaba, Y. Matsuura, T. Ishikawa, N. Yabuuchi, W. Murata and S. Kuze, *Electrochem. Commun.*, 2012, 21, 65.
38. J. Qian, Y. Chen, L. Wu, Y. Cao, X. Ai and H. Yang, *Chem. Commun.*, 2012, 48,

7070.

39. C. Wang, Y. Li, Y.-S. Chui, Q.-H. Wu, X. Chen and W. Zhang, *Nanoscale*, 2013, 5, 10599.
40. M. Winter and J. O. Besenhard, *Electrochim. Acta*, 1999, 45, 31.
41. H. S. Im, Y. J. Cho, Y. R. Lim, C. S. Jung, D. M. Jang, J. Park, F. Shojaei and H. S. Kang, *ACS Nano*, 2013, 7, 11103.

Chapter 6. Screening of other metal nitrides for sodium-ion batteries

Screening of the electrochemical performance of other metal nitrides in Na-ion batteries was investigated in this work. These materials have been studied as the negative electrode material in lithium-ion batteries in the literature, but not in sodium-ion batteries. In this chapter, the electrochemical performance of these materials as the negative electrode in sodium-ion batteries is presented. Some of them showed a poor electrochemical performance in sodium-ion batteries, thus no further research would be worthy to continue.

Specifically, chromium nitride was synthesized and its electrochemical performance in lithium-ion batteries was compared with the literature and its behaviour in sodium-ion batteries was investigated. Vanadium nitride, molybdenum nitride and manganese nitride samples were prepared by my colleague, Mr Syed Imran Ullah Shah from solution phase ammonolysis synthesis. Their electrochemical performances as the negative electrode material in sodium-ion batteries were evaluated. In this work, the general study of nickel zinc nitride prepared by Dr Kripasindhu Sardar from solid-state synthesis, as the negative electrode material in sodium cells was conducted. Nickel phosphide, worked jointly with my project student, Miss Deborah Benjamin, was synthesized from hydrothermal route and its preliminary electrochemical performance in lithium-ion and sodium-ion batteries was investigated.

In this work, electrochemical testing used a Bio-Logic SP150 or MPG potentiostat. The

working electrode consisted of a powdered mixture of 75% active material with 20% of acetylene black (Shawinigan, Chevron Phillips Chemical Co. LP) and 5% PVdF dissolved into cyclopentanone to form the ink, then dropping onto 50 μm thick and 10mm in diameter copper foil disk.

Electrochemical cells were assembled in two-electrode Swagelok cells using sodium or lithium metal foil (Aldrich, 99.9%) as the counter and reference electrode. Two sheets of Whatman GF/D borosilicate glass fibre were used as separator, soaked with 1 M LiPF_6 in ethylene carbonate/dimethyl carbonate (1:1) electrolyte in lithium-ion batteries and 1 M NaPF_6 in ethylene carbonate/diethyl carbonate (1:1) electrolyte in sodium-ion batteries.

6.1 Chromium nitride

Chromium nitride (CrN) has a rock salt structure with nitrogen atoms occupying the octahedral holes in the chromium lattice.¹ It exhibited a paramagnetic to antiferromagnetic transition at 280 K.² CrN coatings have been used for corrosion resistance and plastic moulding applications³ and in the case of hot corrosion resistance, these showed superior properties to TiN .^{4,5} CrN was also used for optical and decorative coatings.^{6,7} Amorphous CrN can be obtained from ammonolysis of CrCl_3 precursor at 500 $^\circ\text{C}$ and the crystallinity increased with the temperature.⁸ At 550 $^\circ\text{C}$, around 8 nm crystallites was observed, and increased to 30 nm at 800 $^\circ\text{C}$. Chromium nitride was obtained via solvothermal reactions of CrCl_3 with Li_3N in benzene at 400 $^\circ\text{C}$.⁹ It was also prepared from the molecular precursor, $\text{Cr}(\text{NEt}_2)_4$, from 335 $^\circ\text{C}$ and Cr_2N was obtained heated up to 1000 $^\circ\text{C}$.¹⁰ Das *et al.*¹¹ proposed a synthesis route of ammonolysis of Cr-urea precursor, which is adopted in this project.

Chromium nitride (CrN) has a large nitrogen content of approximately 21%, which could result in a high theoretical capacity (1218 mA h g^{-1}) from the conversion reaction in Na-ion batteries.



In recent years, chromium nitride has been studied by Sun *et al.*¹²⁻¹⁴ in lithium ion batteries. A capacity of 1200 mA h g^{-1} was obtained after the second reduction cycle, a value that remains relatively stable upon cycling. Das *et al.* also prepared CrN nanoparticles which can offer a stable reversible capacity of around 500 mA h g^{-1} at 60 mA g^{-1} for 160 cycles.¹¹

6.1.1 Synthesis and characterization of chromium nitride

0.008 mol (2.13 g) chromium chloride ($\text{CrCl}_3 \cdot 6\text{H}_2\text{O}$) (98%, Sigma Aldrich) was dissolved in absolute ethanol (20 ml) to obtain a concentrated solution named as Sol-A. Then, the Sol-A was added dropwise into saturated urea/ethanol solution (0.048 mole of urea ($\text{CO}(\text{NH}_2)_2$), purity, 99%, Aldrich) dissolved in 20 mL of ethanol at $60\text{-}70 \text{ }^\circ\text{C}$ with stirring, until the final salt/urea molar ratio reached 1 : 6. The obtained green precipitate of Cr–urea coordinated compound was separated by filtering and dried at $80 \text{ }^\circ\text{C}$. This preparation was followed the urea route proposed by Das *et al.*¹¹ The precursor was heated to various temperatures between 500 to $800 \text{ }^\circ\text{C}$ at $1 \text{ }^\circ\text{C min}^{-1}$ under flowing ammonia and maintained at the target temperature for 2 hours. XRD patterns of the products are shown in Figure 6.1.

It can be seen that the crystallinity of CrN increased with the heating temperature. $500 \text{ }^\circ\text{C}$ pattern showed broad CrN peaks. However, the background difference between 500 and

600 °C probably indicates some amorphous contents due to the uncompleted decomposition of the precursor. At 600 °C, a pure phase CrN with broad patterns was obtained, and the peaks became sharper with increasing the temperature.

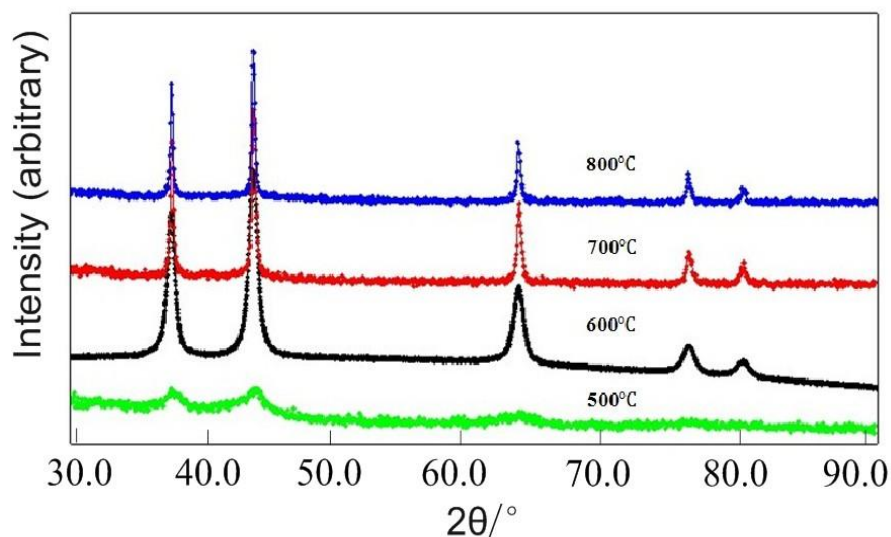


Figure 6.1 XRD patterns of CrN derived from ammonolysis of $\text{Cr}[\text{OC}(\text{NH}_2)_2]_6\text{Cl}_3$ at different temperatures.

The fitted XRD pattern of CrN synthesized at 600 °C is shown in Figure 6.2. The refined parameters are $a=4.14782(19)$ Å, cell volume is 71.361(6), which are in agreement of the value of $a=4.151(2)$ Å given by Das *et al.*¹¹ Crystallite size was determined to be 15.26(3) nm from the Lorentzian components of the profile fit.¹⁵

The TEM graphs shows the main morphology of CrN derived from urea precursor is nanoparticles with approximately 15 nm in diameter. Heavy aggregation can be observed in several regions of the images, suggesting the inaccessible surface of this sample.

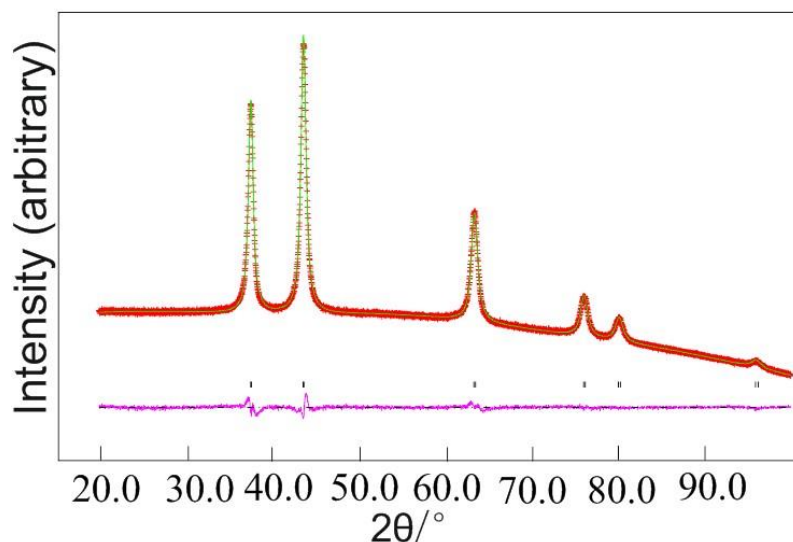


Figure 6.2 Rietveld fit ($R_{wp} = 1.3\%$, $R_p = 1\%$) to the PXD data for CrN produced from ammonolysis of $\text{Cr}[\text{OC}(\text{NH}_2)_2]_6\text{Cl}_3$ at 600°C . Crosses mark the data points, the upper continuous line the fit and the lower continuous line the difference. Tick marks show the allowed positions of reflections for CrN with space group Fm-3m.¹⁶

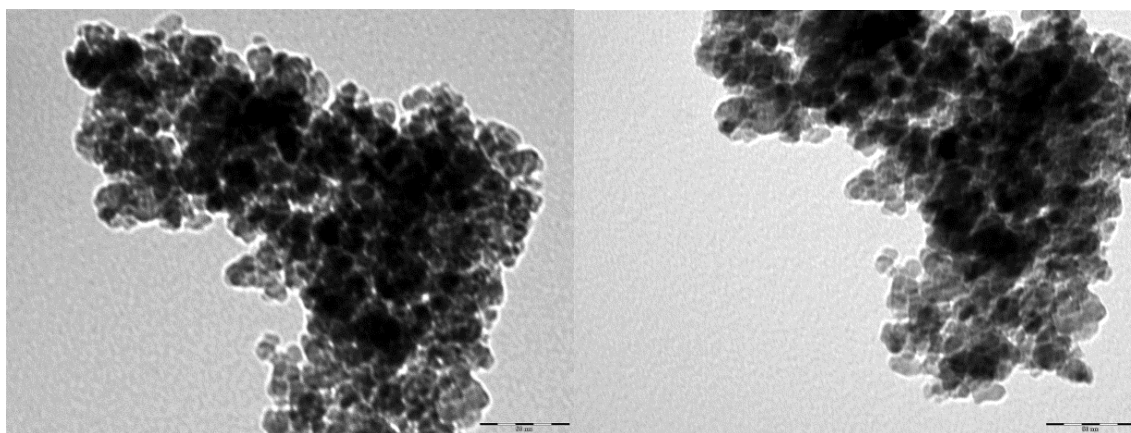


Figure 6.3 TEM pictures of chromium nitride obtained at 600°C with 100 nm (left) or 50 nm (right) scale bar.

A typical IR spectrum is shown in Figure 6.4. The peak at around 500 cm^{-1} corresponds to the metal-nitrogen bond.¹⁷ The presence of amine and amide groups in the form of absorptions at 3150 cm^{-1} ($\nu(\text{NH})$),¹⁰ and 1599 cm^{-1} ($\delta(\text{NH}_2)$).^{10, 17} was found in the

spectra and the peaks at 2800 cm^{-1} and 1400 cm^{-1} are matched with the adsorptions of alkyl groups,¹⁷ which could be due to residual urea precursor left in the sample. Hydroxyl group at 3400 cm^{-1} was found in the spectra, which could be attributed to the minor moisture at sample surface. Although CHN elemental analysis shows around 19% nitrogen (theoretically, 21.2% N calculated from CrN formula) with untraceable carbon and hydrogen was found in the product, the weak metal nitrogen bond and the alkyl or amide groups were observed in its IR spectrum. This could be due to the fact that it is difficult to be very concentrated to see the metal nitrogen bond when prepared the IR disk using minor CrN sample.

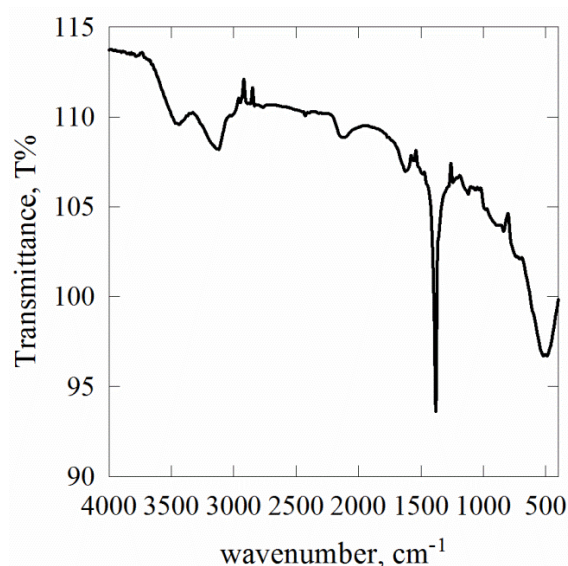


Figure 6.4 Infrared spectra of CrN obtained from urea route at $600\text{ }^{\circ}\text{C}$

6.12 Chromium nitride as the negative electrode material for Li-ion batteries

Cyclic voltammetry of CrN in lithium ion batteries was measured between 1 mV to 3 V against Li metal foil at 1 mV s^{-1} for 30 cycles. During the first cathodic scan (negative scan), there is a large irreversible reduction peak near to 0 V. This large irreversible

reduction process was attributed to side reactions by Das *et al.*¹¹ However, differing from the results of Das *et al.*, two irreversible peaks at 0.42 V and 0.65 V were not found. After the first cycle, the storage charge slightly increased with the cycle number, which could be due to the surface electrolyte interface (SEI) formation.

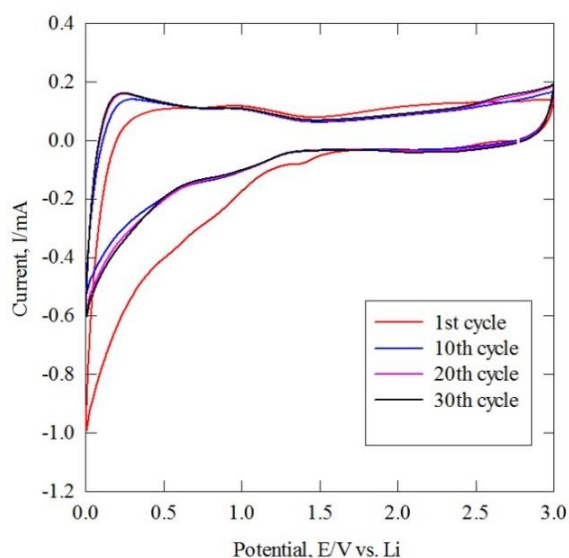


Figure 6.5 Cyclic voltammetry of CrN derived from urea route at 1st, 10th, 20th and 30th cycle.

Scan rate is 1 mV s^{-1} . The counter electrode and reference electrode is lithium metal foil and the electrolyte is 1 M LiPF_6 in EC:DMC (1:1).

The galvanostatic testing was conducted at two different current rates. CrN derived from the urea route shows similar voltage profiles to other nitride materials in lithium ion batteries in which large voltage hysteresis was observed during cycling, which could be due to the intrinsic defect of the conversion reaction.¹⁸ There is a large irreversible reduction specific capacity observed in the first cycle of 269 mA h g^{-1} (1 C) and 345 mA h g^{-1} (0.5 C). As a result, the initial Coulombic efficiency is low at 48% and 50%, respectively. With the formation of SEI layer, the Coulombic efficiency increased to approximately 100% during the rest of the cycles. The reduction specific capacity

dropped to 114 mA h g^{-1} (1 C) and 139 mA h g^{-1} (0.5 C) after 50 cycles. Comparing to other nitride materials in lithium ion batteries, CrN derived from urea route showed a relatively stable cycling performance. In terms of at 0.5 C current rate, the reduction specific capacity is 149 mA h g^{-1} in 10th cycle while 139 mA h g^{-1} in 50th cycle, around 7% capacity loss.

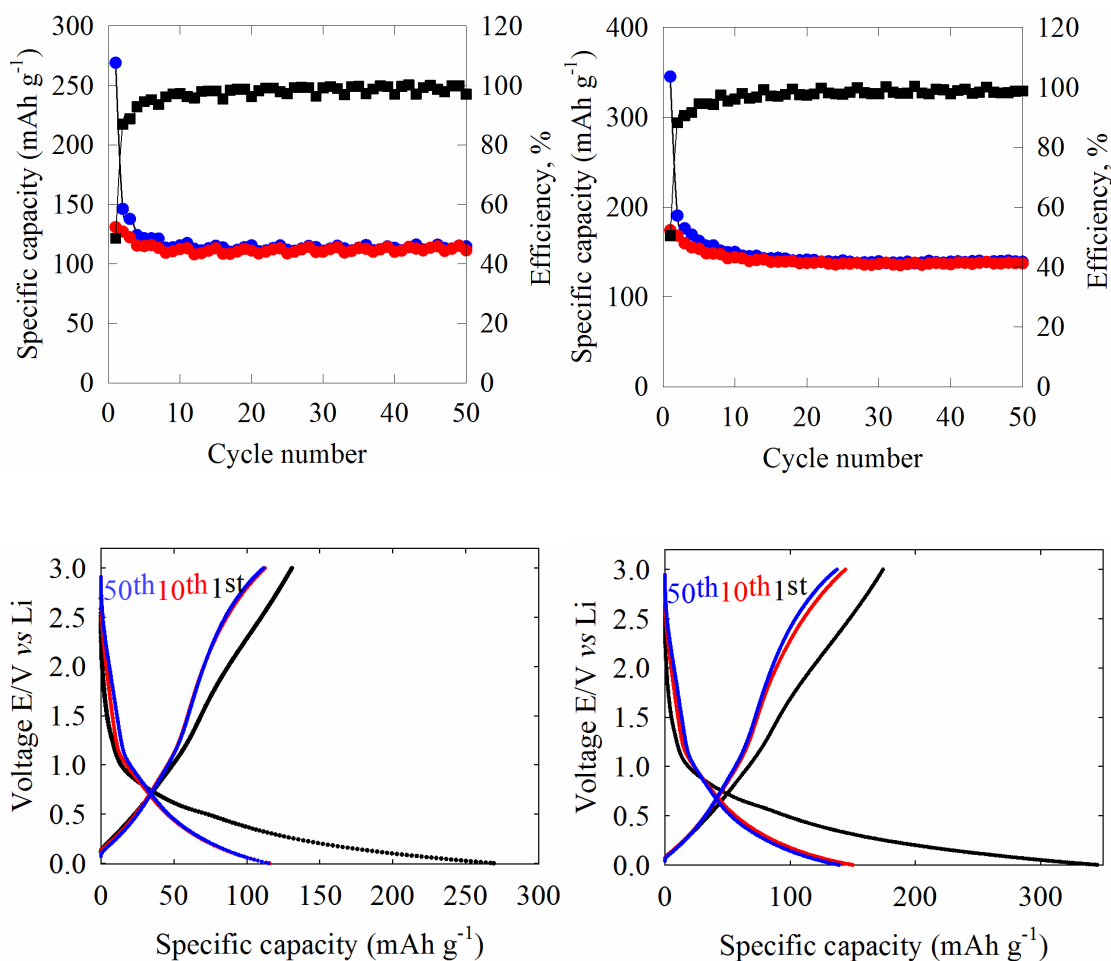


Figure 6.6 Voltage profile against specific cycles (bottom) and specific capacity versus cycle number profile (top) of CrN-lithium half cells cycled between 1 mV and 3 V for 50 cycles at 1 C (1218 mA g^{-1} , left), 0.5 C (600 mA g^{-1} , right). In the specific capacity vs cycle number plots red circles show specific reduction capacity, blue circles show specific oxidation capacity and black ones depict Coulombic efficiency.

The differential capacity plot of CrN derived from urea route at different current rates in lithium cells is presented in Figure 6.7. A sharp reduction peak at around 0 V and a minor peak at around 0.65 V against Li was observed in the first cycle, which is described as several electrochemical processes of CrN with lithium by Das *et al.*¹¹ However, these reduction peaks rapidly diminished in the second cycle, suggesting the large irreversible capacity due to the electrochemical process observed in the first cycle. It is interesting to see that the reduction peak had a minor shift from 0.65 V at 0.5 C to 0.6 V at 1 C, which could be attributed to the larger charge loss from the internal resistance at higher current rate. The electrochemical performance of CrN derived from urea route at 600 °C in lithium-ion batteries was similar to that of the literature published by Das *et al.*¹¹

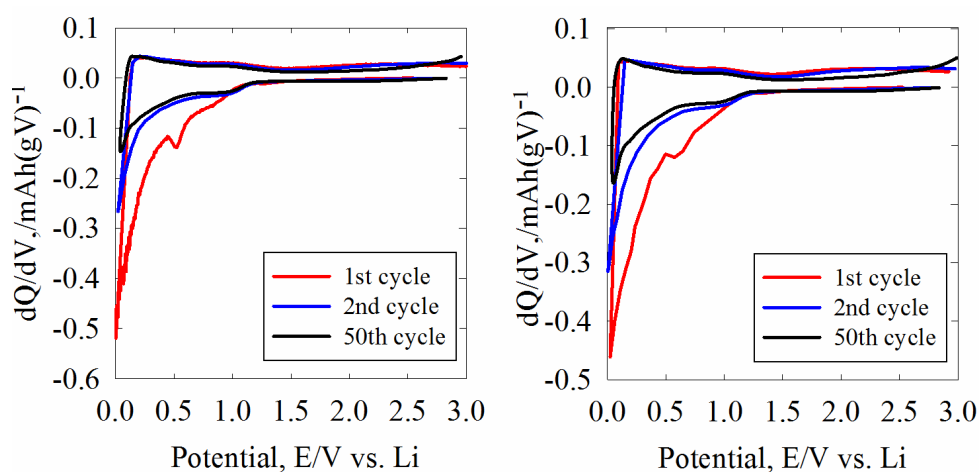


Figure 6.7 Differential capacity vs voltage of CrN derived from urea route in lithium half cells between 1 mV and 3 V at 1 C (1200 mA g⁻¹, left), 0.5 C (600 mA g⁻¹, right). The counter electrode is lithium metal foil and the electrolyte is 1M LiPF₆ in EC:DMC (1:1).

6.1.3 Chromium nitride as the negative electrode material for Na-ion batteries

Cyclic voltammetry of CrN in sodium ion batteries was measured between 1 mV to 3 V against Na metal foil at 10 mV s^{-1} for 30 cycles. As with lithium cells, a large irreversible reduction peak near to 0.3 V and several minor peaks near to 2.5 V were observed in the first negative scan. These peaks could correspond to the reaction of CrN with Na and the side reactions to form the SEI layer. In the subsequent cycles, the shoulder reduction/oxidation peak couple at around 0.8 V and a sharp redox couple at around 0.1 V were found in the CV graph, which could be the main charge storage at the as formed SEI layer. The CVs of 10th, 20th and 30th cycle are similar and the curves are overlapped with each other, suggesting a good cycle stability after the initial cycles.

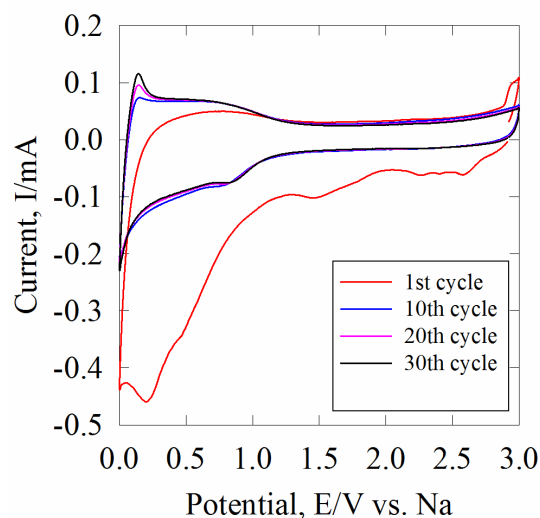


Figure 6.8 Cyclic voltammetry of CrN derived from urea route at 1st, 10th, 20th and 30th cycle.

Scan rate is 10 mV s^{-1} . The counter electrode and reference electrode is sodium metal foil and the electrolyte is 1M NaPF_6 in EC:DEC (1:1).

As with lithium-ion batteries, CrN as the negative electrode material in Na-ion cells shows similar cycling performance and voltage profiles. There is a large irreversible reduction specific capacity observed in the first cycle, 236 mA h g⁻¹ (600 mA g⁻¹) and 406 mA h g⁻¹ (100 mA g⁻¹). Worse than that in Li-ion cells, the initial Coulombic efficiencies in Na-ion cells are only 20% and 17%, which could be due to the slower kinetic of the sodium ions than lithium ions. With the stabilization of the SEI layer, the Coulombic efficiency increased to approximately 97% during the rest of the cycles. After 50 cycles, the reduction specific capacity dropped to 40 mA h g⁻¹ (at 600 mA g⁻¹) and 62 mA h g⁻¹ (at 100 mA g⁻¹), respectively. The cycle stability was reasonably good, around 92% capacity retention from 10th cycle to 50th cycle at 100 mA g⁻¹ was maintained. And the voltage profile graphs show most of the charge was stored below 2 V. However, after 50 cycles, only less than 5% theoretical specific capacity (1218 mA h g⁻¹) based on the reaction of CrN with Na (Equation 6.1) was remained. The massive difference between the real capacity and the theoretical capacity indicated most of the active electrode material might not be used to store the charge due to the passivation of the SEI layer.

The differential capacity plot of CrN in sodium cells is presented in Figure 6.10. Unlike that in lithium cells, more reduction peaks were found in the first reduction cycle, suggesting the complexity of the reaction of CrN with sodium. These multiple electrochemical processes corresponding to the reduction peaks could be attributed to the processes of CrN reacted with sodium and the formation of the SEI layer. However, the specific processes were not clear. At the rate of 600 mA g⁻¹, the shoulder redox peak couple can be found near to 0.6 V with minor voltage hysteresis in the sodium half-cell

while the ones in the lithium half-cell was observed around 0.9 V, which presumably indicated the same electrochemical process as the naturally standard potential of sodium is around 0.3 V lower than that of lithium. Thus, it can be extrapolated that the charge storage mechanism of as-prepared CrN in sodium cells and lithium cells could be similar at the surface interphase mixed with CrN, carbon black and electrolyte

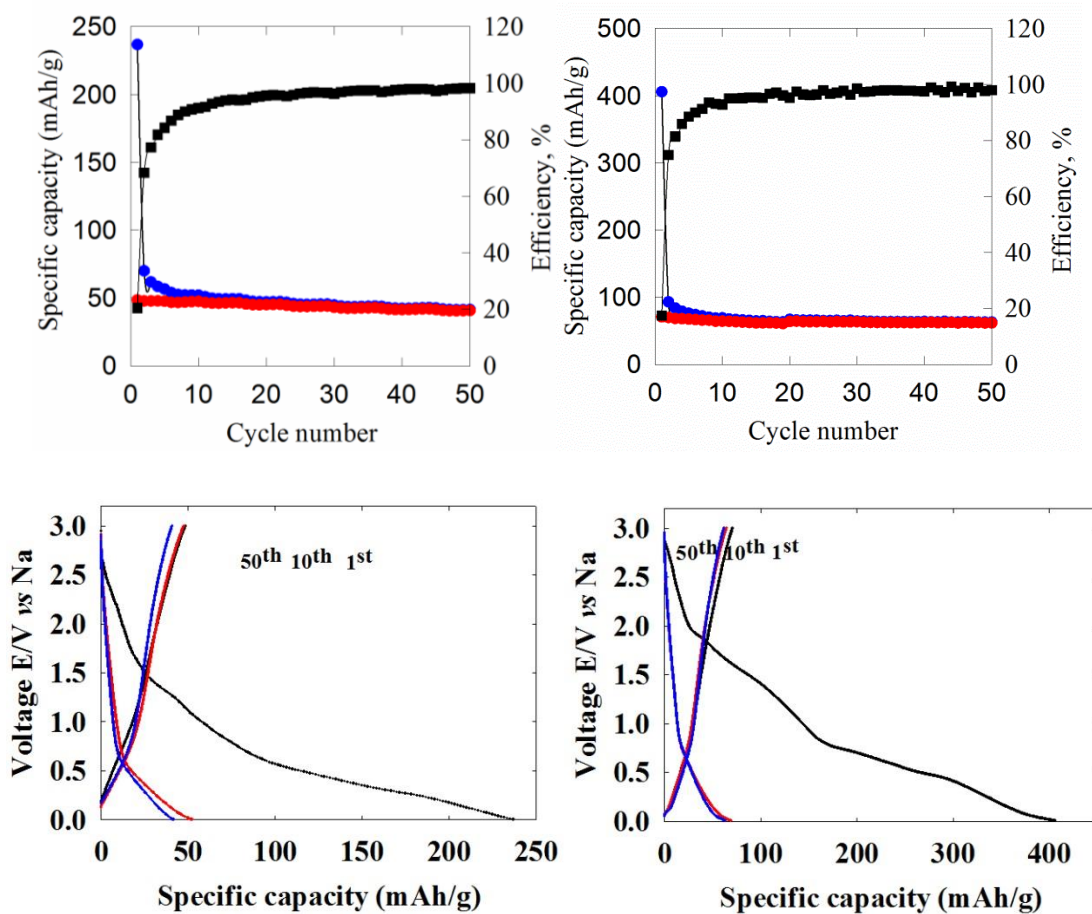


Figure 6.9 Voltage profile against specific cycles (bottom) and specific capacity versus cycle number profile (top) of CrN-sodium half cells cycled between 1 mV and 3 V for 50 cycles at 600 mA g⁻¹ (left), 100 mA g⁻¹ (right). In the specific capacity vs cycle number plots red circles show specific reduction capacity, blue circles show specific oxidation capacity and black ones depict Coulombic efficiency.

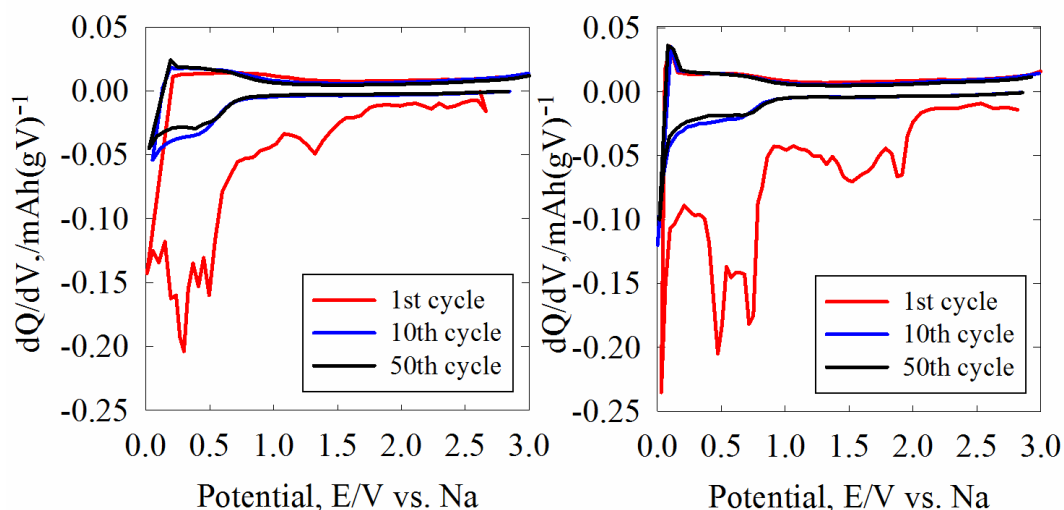


Figure 6.10 Differential capacity vs voltage of CrN derived from urea route in sodium half cells between 1 mV and 3 V at 600 mA g⁻¹ (left) and 100 mA g⁻¹ (right). The counter electrode is sodium metal foil and the electrolyte is 1M NaPF₆ in EC:DEC (1:1).

6.2 Vanadium nitride

Vanadium nitride (VN) material exhibited advantages of corrosion resistance, high temperature and chemical stability.¹⁹ Vanadium nitride showed promising potential in the anode for supercapacitor due to its large specific capacitance (1340 F g⁻¹), high conductivity ($1.67 \times 10^6 \Omega^{-1} \text{m}^{-1}$) and suitable voltage window.²⁰⁻²² It was reported that VN thin film showed a high first reduction capacity of 1500 mA h g⁻¹ as the negative electrode material for lithium ion batteries and the capacity of VN was found stable over 800 mA h g⁻¹ after 50 cycles.¹² This material also exhibited reasonably good rate capability (1000 mA g⁻¹) in Li-ion batteries.²³

Cyclic voltammetry of VN in sodium ion batteries showed several irreversible reduction peaks at around 1 V, 1.5 V, 0 V and above 2 V in the first reduction cycle. However, the corresponding oxidation peaks were not found in the subsequent cycles, which indicates

a large irreversible capacity and poor Coulombic efficiency in the initial cycles. This relatively poor performance was also observed in its galvanostatic cycling test in Na-ion cells.

Similar to CrN, VN has a large theoretical specific capacity, over 1000 mA h g⁻¹ in Na-ion cells based on the conversion reaction (Figure 6.2).



Equation 6.2

However, from its CV result, it can be seen that most of the capacity cannot be retrieved after the first cycle. Thus, in this work, low current rates (200 mA g⁻¹ and 100 mA g⁻¹) were used for its galvanostatic cycling test in Na-ion cells to minimise the impact from the internal resistance (IR) drop in the cell. For both of current rates, the cycling performances were similar (Figure 6.12).

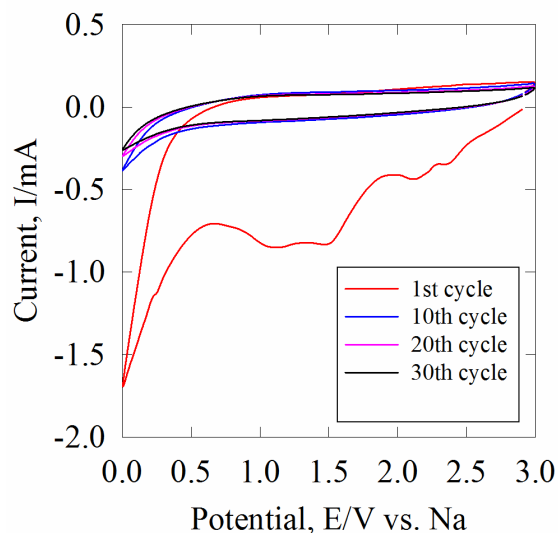


Figure 6.11 Cyclic voltammetry of VN at 1st, 10th, 20th and 30th cycle. Scan rate is 10 mV s⁻¹. The counter electrode and reference electrode is sodium metal foil and the electrolyte is 1M NaPF₆ in EC:DEC (1:1).

In the galvanostatic test, 217 mA h g⁻¹ capacity at 200 mA g⁻¹ and a capacity of 336 mA h g⁻¹ at 100 mA g⁻¹ were observed in the first reduction cycle. But minor portion of these were recovered in the first oxidation cycle (27 mA h g⁻¹ at 100 mA g⁻¹ and 41 mA h g⁻¹ at 100 mA g⁻¹), resulting in around 12% Coulombic efficiency for both cases. During the first reduction cycle, there are two voltage slopes (around 1.8 V and 0.5 V) observed from the voltage profile graphs (Figure 6.12 bottom,).

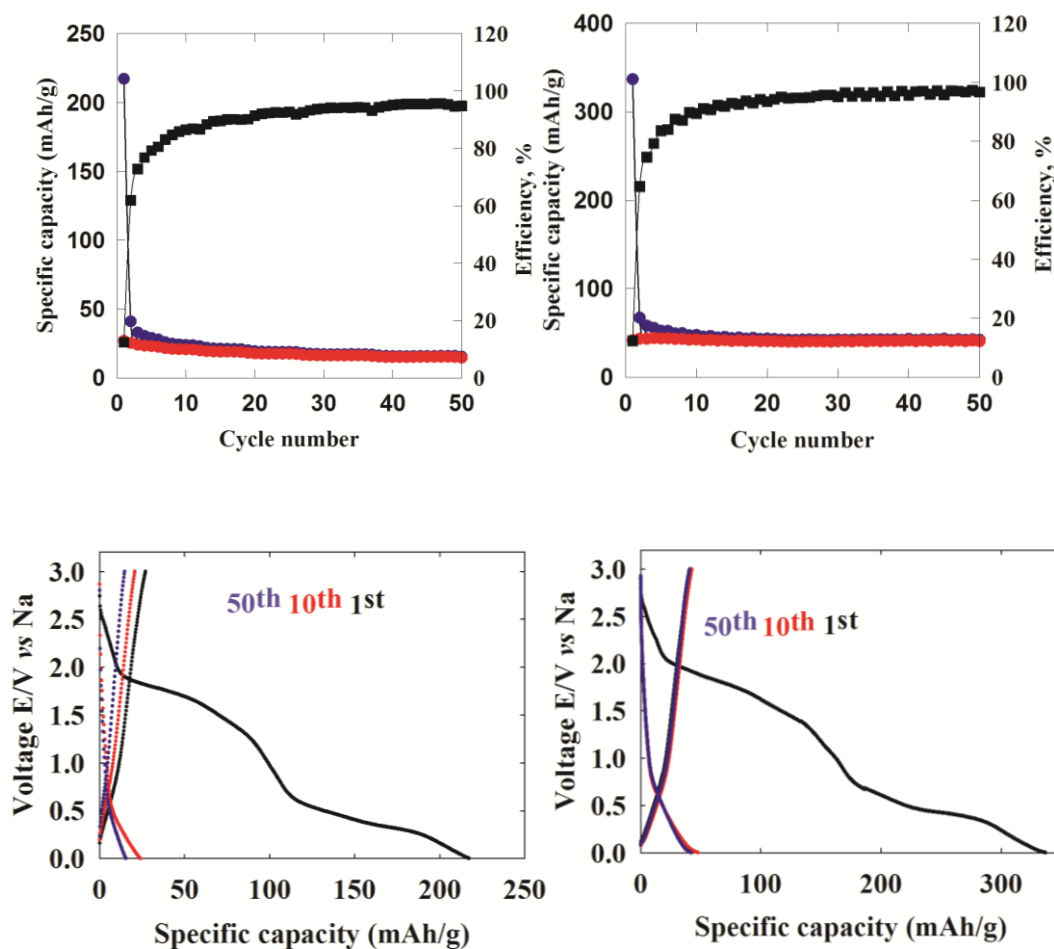


Figure 6.12 Voltage profile against specific cycles (bottom) and specific capacity versus cycle number profile (top) of VN-sodium half cells cycled between 1 mV and 3 V for 50 cycles at 200 mA g⁻¹ (left), 100 mA g⁻¹ (right).

From the derived differential capacity plots (Figure 6.13), it can be seen sharp reduction peaks in the first reduction cycle around 1.8 V and 0.5 V for both cases, which are corresponding to the voltage slopes. Consistent with the CV graph, these peaks were diminished in the subsequent cycles, suggesting these electrochemical processes could be attributed to the side reactions to form the SEI layer. The electrochemical performance of VN in sodium half cells is similar to that of CrN, large irreversible capacity in the first cycle decayed rapidly in the second cycle, though the cycling stability was good. The poor electrochemical behaviours could not be competitive to other negative electrode materials for Na-ion batteries.

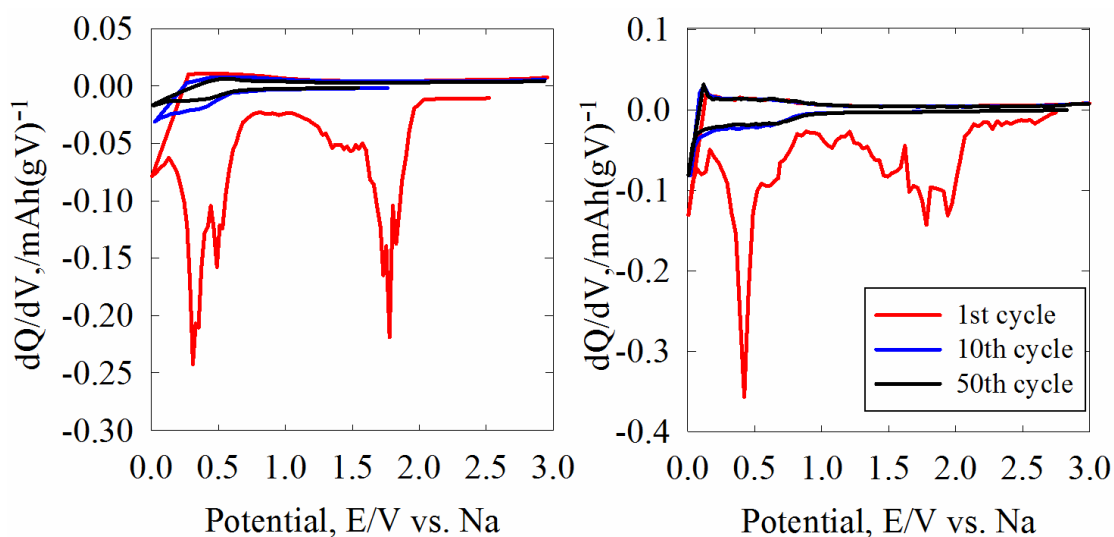


Figure 6.13 Differential capacity vs voltage of VN in sodium half cells between 1 mV and 3 V at 200 mA g⁻¹, (left) and 100 mA g⁻¹, (right). The counter electrode is sodium metal foil and the electrolyte is 1M NaPF₆ in EC:DEC (1:1).

6.3 Molybdenum nitride

Molybdenum nitride thin film has comprehensively studied by Nandi *et al* as the negative electrode material for lithium ion batteries.²⁴ The mechanism of charge storage

was investigated, the lithium ions firstly inserted into the lattice of molybdenum nitride then conversion reaction occurred. A stable capacity of 700 mA h g^{-1} was achieved after 100 cycles at a current density of $100 \mu\text{A cm}^{-2}$. High surface area molybdenum nitride derived from an imide precursor route showed good electrochemical performance in redox supercapacitors.²⁵ The hybrid molybdenum nitride/nitrogen-doped graphene nanosheets (MoN/NGS) exhibited a promising electrochemical performance in Li-O₂ system with 3.1 V discharge voltage and around 1100 mA h g^{-1} capacity. Molybdenum nitride presented a Pt-like electrocatalytic performance in fuel cells²⁶ and dye-sensitized solar cell,²⁷ and this has led to attract extensive attention on nitrides in electrocatalysis in recent years.

The cyclic voltammogram shows a large irreversible reduction peak in the first negative scan close to 0 V and a minor reduction/oxidation peak couple at around 2.1 V in the first cycle. After that, the oxidation peak at around 2.1 V gradually moved to lower potential region and diminished, which have not been observed in other nitride materials in sodium-ion batteries. In the meantime, the reduction peak close to 0 V had a gradual intensity loss with cycle number increase, which could result in a charge loss during the cycling.

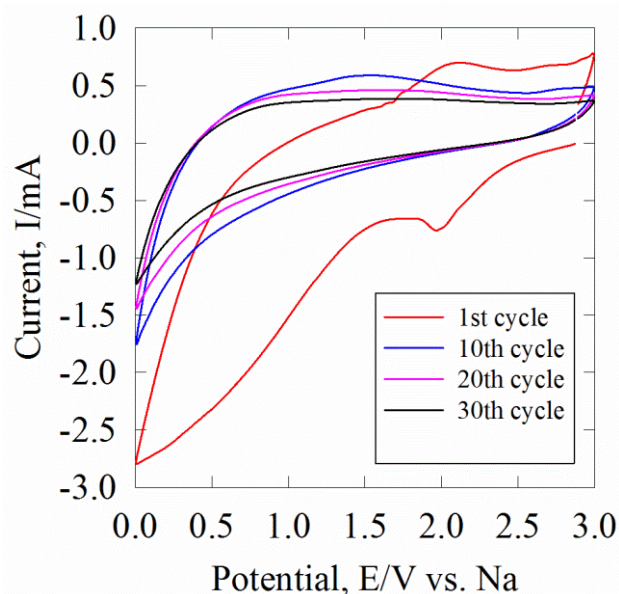


Figure 6.14 Cyclic voltammetry of MoN at 1st, 10th, 20th and 30th cycle. Scan rate is 10mV s^{-1} . The counter electrode and reference electrode is sodium metal foil and the electrolyte is 1M NaPF_6 in EC:DEC (1:1).

Molybdenum nitride shows a good electrochemical performance in Na-ion cells compared with CrN and VN. A capacity of 603 mA h g^{-1} was passed in the first reduction process and 213 mA h g^{-1} capacity was recovered at 100 mA g^{-1} . Unlike VN and CrN, the reduction capacity dropped gradually, rather rate rapidly diminished, in the subsequent cycles. The Coulombic efficiency quickly stabilized from 35% in the first cycle to 94% in the 10th cycle. Although the cycle stability is not as good as CrN or VN, it retained around 100 mA h g^{-1} capacity in the 30th cycle. Still, it can be found that the IR drop in the cells is significant, which could be the SEI layer formation during cycling. The capacity retained at low current rate (100 mA g^{-1}) was approximately as twice as that at high current rate (200 mA g^{-1}). The variations of Coulombic efficiencies observed at 200 mA g^{-1} could be attributed to noises from the instrument, as these were not found in the case at 100 mA g^{-1} . The short shoulder plateau at around 1.5 V in the first

reduction cannot be found in the subsequent cycles, which is similar to other nitride materials used in Na-ion cells.

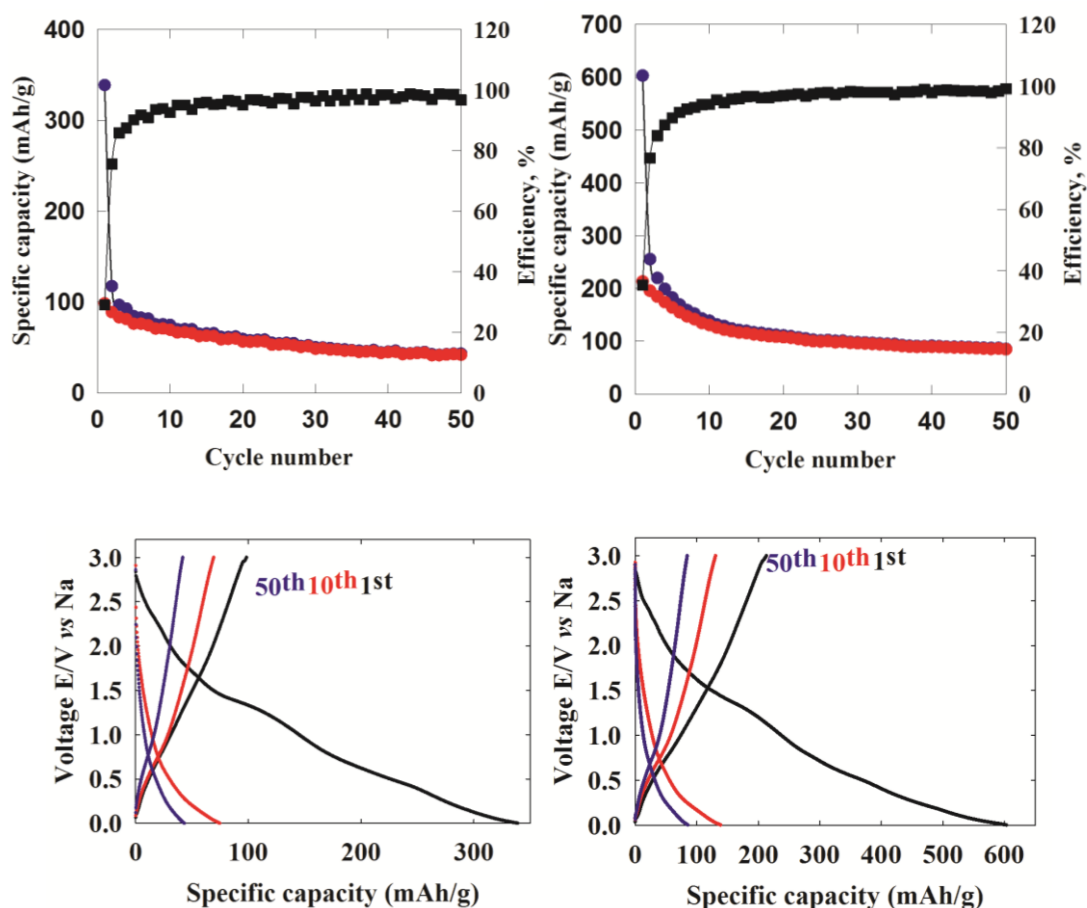


Figure 6.15 Voltage profile against specific cycles (bottom) and specific capacity versus cycle number profile (top) of MoN-sodium half cells cycled between 1 mV and 3 V for 50 cycles at 200 mA g⁻¹ (left), 100 mA g⁻¹ (right). In the specific capacity vs cycle number plots blue circles show specific reduction capacity, red circles show specific oxidation capacity and black ones depict Coulombic efficiency.

Differential capacity plots of MoN at different current rates in sodium half cells are shown in Figure 6.16. As with the case of VN in sodium cells, multiple reduction peaks were found in the first reduction cycle. Three distinct reduction peaks at around, 0 V,

0.4 V and 1.5 V, might be corresponding to the reaction of the MoN with sodium (0.4 V) and the formation of the SEI layer. In the oxidation cycle, most of the peaks were disappeared and two broad peaks were observed at around 0.7 V and 1.7 V, respectively. Unlike VN-sodium cells a broad redox peak couple was found at around 0.6 V (200 mA g⁻¹) in the subsequent cycles. The charge stored due to this redox peak couple could be the extra capacity of MoN against VN-sodium cells.

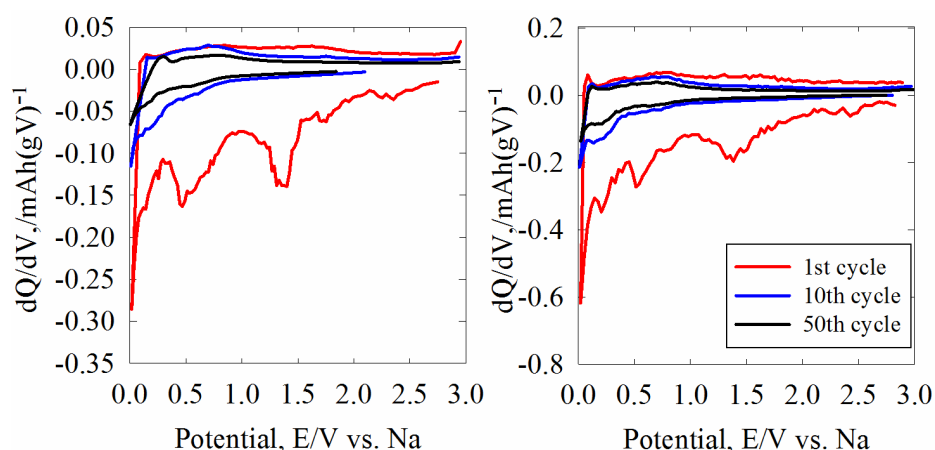


Figure 6.16 Differential capacity vs voltage of MoN in sodium half cells between 1 mV and 3 V at 200 mA g⁻¹, (left) and 100 mA g⁻¹, (right). The counter electrode is sodium metal foil and the electrolyte is 1M NaPF₆ in EC:DEC (1:1).

6.4 Manganese nitride

Thin film manganese nitride prepared from magnetron sputtering has been studied as the negative electrode in lithium ion cells.²⁸ It exhibited capacities of up to 579 mA h g⁻¹ in lithium half cells, and retained 463 mA h g⁻¹ of this capacity in the 110th cycle. Stable cycle performance and low polarization performance of manganese nitride thin film in Li-ion batteries suggested the significant possibility of its suitability in Na-ion cells. Since only thin film based manganese nitride has been studied in lithium-ion batteries, in

this work, screening of electrochemical performance of bulk manganese nitride was also investigated in lithium-ion batteries.

6.4.1 Manganese nitride as the negative electrode material for Li-ion cells

The cyclic voltammetry of Mn_3N_2 in the lithium half-cell was conducted at 10 mV s^{-1} between 1 mV and 3 V for 30 cycles. A sharp reduction peak at $\sim 0 \text{ V}$ and a shoulder peak at 0.7 V were observed in the first cycle (Figure 6.12). The one at 0.7 V moved to 0.9 V and faded in the subsequent cycles while the sharp peak near to 0 V gradually lost its intensity, which showed slightly different potentials from the thin film case.²⁸ Two featured oxidation peaks were found at around 0.5 V and 1.3 V . The one at 1.3 V moved to 1.5 V in subsequent cycles, which indicates the reversibility of the corresponding electrochemical process.

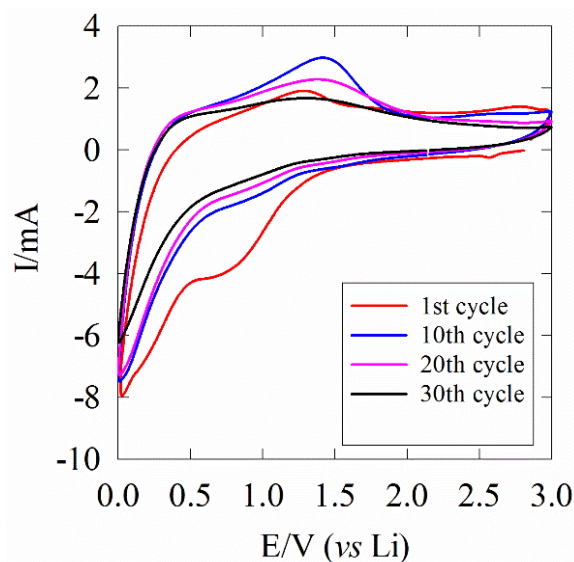


Figure 6.17 Cyclic voltammetry of Mn_3N_2 prepared at $350 \text{ }^\circ\text{C}$ route at 1st, 10th, 20th and 30th cycle.

Scan rate is 10 mV s^{-1} .

Galvanostatic cycling at 200 mA g^{-1} (equivalent to 0.24 C based on reduction to Mn and Li_3N with a theoretical capacity of 833 mA h g^{-1}) showed a larger than theoretical capacity in the first reduction cycle, suggesting other processes including solid electrolyte interface (SEI) formation during this step. Similar multiple features in the first reduction cycle were observed in thin film sample with a voltage plateau at 0.3 V.²⁸ The capacity was retained over 600 mA h g^{-1} after the first reduction cycle and gradually reduced to 340 mA h g^{-1} in the 50th cycle. During reduction almost all charge is passed in the potential region below 2 V, but during oxidation (which is the discharge process in the full lithium-ion cell), around 57% capacity in the region below 2 V during the first oxidation, improving to 97% in the 50th cycle. This could be due to the Li_3N decomposed above 2 V.¹⁸ In the voltage profile graph, the plateau at 0.3 V in the first cycle, moved up to around 0.5 V in the 10th cycle, and this plateau changed to short with the cycle number increase. This indicates the main charge storage is due to the electrochemical process corresponding to this voltage plateau, as the capacity decay was also observed with the cycle number.

In Figure 6.19, a sharp reduction peak at around 0.3 V and a minor peak at around 0.7 V were observed in the first cycle, which could correspond to the conversion reaction of Mn_3N_2 with lithium and the formation of SEI layer, respectively. In the second cycle, the redox couple peaks were observed at around 0.6 V in the reduction cycle and a broad peak at around 1.3 V was found in the corresponding oxidation process. The intensity of this redox peak couple reduced with cycle number increase.

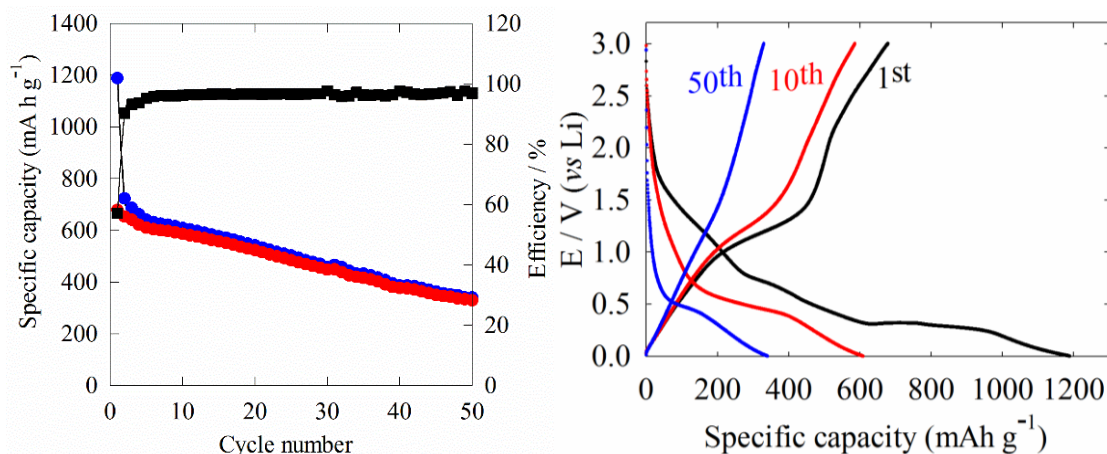


Figure 6.18 Voltage profile against specific cycles (right) and specific capacity versus cycle number profile (left) of Mn_3N_2 -lithium half cells cycled between 1 mV and 3 V for 50 cycles at 200 mA g^{-1} . In the specific capacity vs cycle number plots blue circles show specific reduction capacity, red circles show specific oxidation capacity and black ones depict Coulombic efficiency.

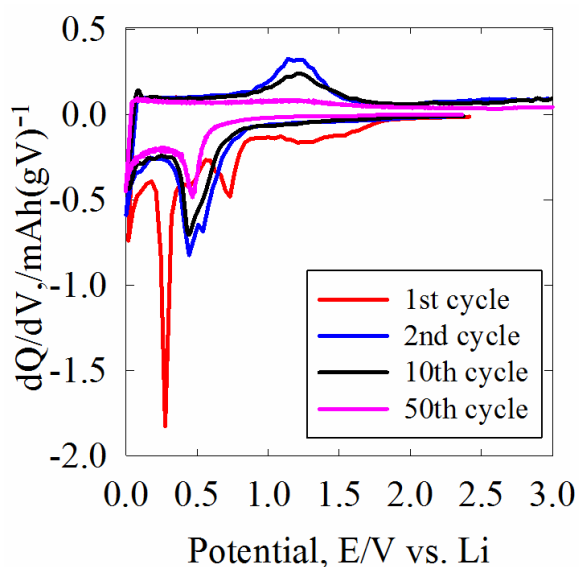


Figure 6.19 Differential capacity vs voltage plot of Mn_3N_2 in lithium half-cell between 1 mV and 3 V at 200 mA g^{-1} for 50 cycles. The counter electrode is lithium metal foil and the electrolyte is 1M LiPF_6 in EC:DMC (1:1).

6.4.2 Manganese nitride as the negative electrode material for Na-ion cells

Unlike that in lithium-ion cells, the CV graph of manganese nitride in sodium-ion cells showed multiple irreversible reduction peaks in the first negative scan, which could include the formation of solid electrolyte interphase (SEI) layer. In the subsequent cycles, a minor shoulder redox peak couple was found at 0.5 V, suggesting the different electrochemical process from that in lithium-ion cells. The minor hump around 3 V was found, but the corresponding electrochemical process is not understood.

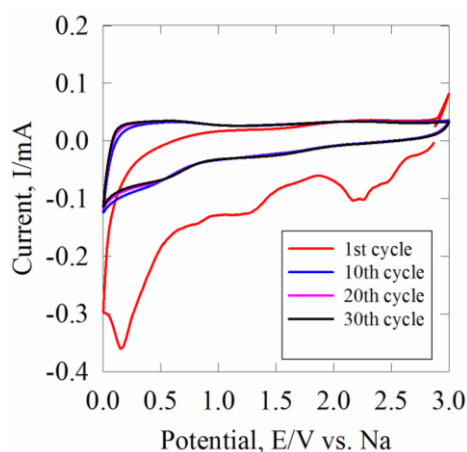


Figure 6.20 Cyclic voltammetry of Mn_3N_2 at 1st, 10th, 20th and 30th cycle. Scan rate is 10 mV s^{-1} .

The counter electrode and reference electrode is sodium metal foil and the electrolyte is 1M NaPF_6 in EC:DEC (1:1)

Galvanostatic test was conducted in sodium-ion cells at two low current rates. (200 mA g^{-1} and 50 mA g^{-1}). When at low current rate (50 mA g^{-1}), this manganese nitride showed a higher specific reduction capacity and better cycle stability than that of molybdenum nitride in sodium-ion cells, but lower than that in lithium-ion cells. In the first reduction, 623 mA h g^{-1} capacity was passed and around 150 mA h g^{-1} was recovered. This low Coulombic efficiency is consistent to its CV result, which could be due to the

formation of SEI layer. However, in the 10th cycle, there was 142 mA h g⁻¹ capacity remained and even in the 50th cycle, over 127 mA h g⁻¹ capacity was retained. Only around 10% capacity loss occurred from the 10th cycle to the 50th cycle, which showed good cycle stability as chromium nitride, but a higher specific capacity. Most of the charge was virtually passed in the region below 2V. Although the capacity was not as high as that with lithium-ion cells, the good cycle stability and the reversible capacity (127 mA h g⁻¹ in the 50th cycle at 50 mA g⁻¹) make manganese nitride a competitive negative electrode material in sodium-ion batteries.

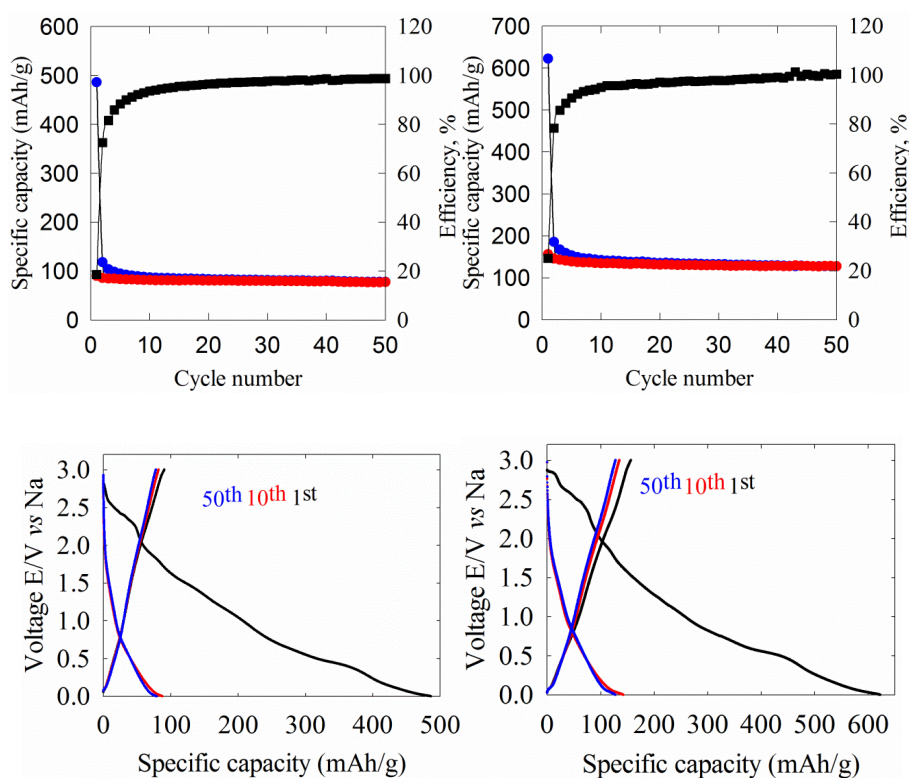


Figure 6.21 Voltage profile against specific cycles (bottom) and specific capacity versus cycle number profile (top) of Mn₃N₂-sodium half cells cycled between 1 mV and 3 V for 50 cycles at 200 mA g⁻¹ (left), 50 mA g⁻¹ (right). In the specific capacity vs cycle number plots red circles show specific reduction capacity, blue circles show specific oxidation capacity and black ones depict Coulombic efficiency.

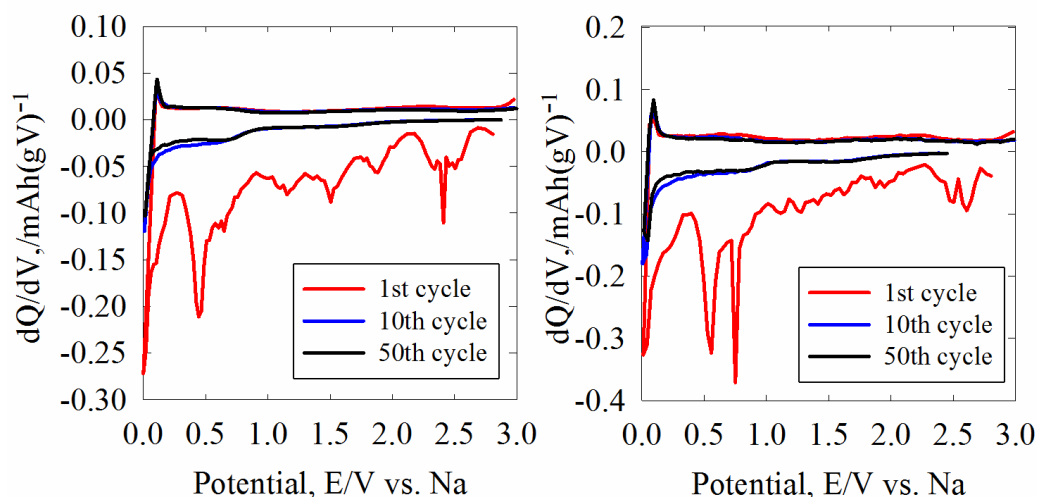
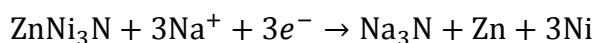


Figure 6.22 Differential capacity vs voltage of Mn_3N_2 in sodium half cells between 1 mV and 3 V at 200 mA g^{-1} , (left) and 50 mA g^{-1} , (right). The counter electrode is sodium metal foil and the electrolyte is 1 M NaPF_6 in EC:DEC (1:1).

6.5 Zinc nickel nitride

The CV result of this ternary nitride was similar to that of other binary nitrides in Na-ion cells. In the first reduction, there are several irreversible reduction peaks and a sharp peak at around 0.2 V. And the main charge stored below 0.5 V might be due to the formation of the SEI layer. Although the cycle stability is acceptable, the charge transferred in the sequent cycles is not large enough.

The theoretical capacity is 316 mA h g^{-1} calculated from the conversion reaction (Equation 6.3) and in this case, 158 mA g^{-1} (0.5 C) was selected as current rate to conduct galvanostatic test.



Equation 6.3

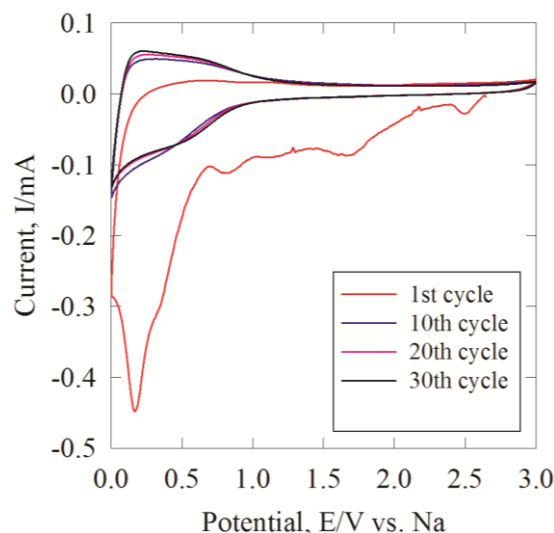


Figure 6.23 Cyclic voltammetry of ZnNi₃N in the 1st, 10th, 20th and 30th cycle. Scan rate is 10 mV s⁻¹. The counter electrode and reference electrode is sodium metal foil and the electrolyte is 1M NaPF₆ in EC:DEC (1:1).

Consistent with its CV result, the cycling performance of this ternary nitride on Na-ion cells showed a relatively large specific capacity in the first reduction which was proven to be mostly irreversible capacity. Also, from the voltage profile, during the first reduction, there are several minor plateaus and a relatively long plateau at around 0.4 V observed. However, after the first reduction, the capacity faded quickly and stabilized at around 40 mA h g⁻¹ in the subsequent cycles, which could be due to the poor electrochemical SEI layer formation blocking the electrode surface.

Similar to the *ex situ* XRD result of nickel nitride, the expected phase change during charge/discharge - was not observed. The main pattern peaks were still zinc nickel nitride, and no zinc or nickel metal peaks were found. This could be due to the conversion reaction only occurred on the electrode surface and formed a thin amorphous layer which cannot be observed in the *ex situ* XRD graph. There is no evidence that sodium ions

inserted into the lattice of zinc nickel nitride. In all, combining the poor galvanostatic performance of zinc nickel nitride in Na-ion cells, it can be extrapolated that the low real capacity achieved could be presumably due to the unsuccessful conversion reaction in the sodium ion cells.

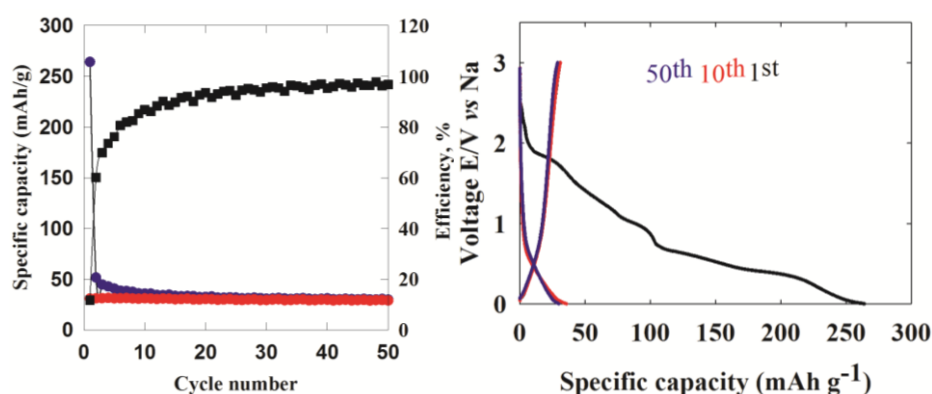


Figure 6.24 Voltage profile against specific cycles (right) and specific capacity versus cycle number profile (left) of ZnNi_3N -sodium half cells cycled between 1 mV and 3 V for 50 cycles at 158 mA g^{-1} (0.5C). In the specific capacity vs cycle number plots, blue circles show specific reduction capacity, red circles show specific oxidation capacity and black ones depict Coulombic efficiency.

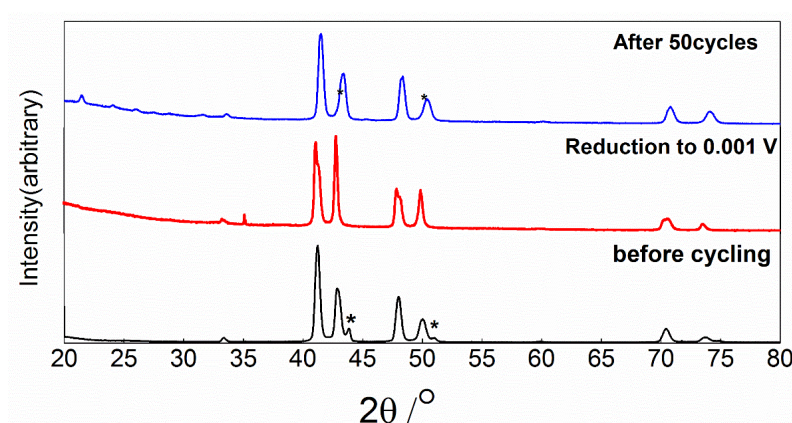


Figure 6.25 *Ex situ* XRD patterns of ZnNi_3N cycled in sodium ion batteries. Asterisks denote the peaks from the copper current collector.¹⁶

6.6 Nickel phosphide

Phosphides and nitrides are in the same reactive group, as they have similar chemical structures and properties. The nickel phosphide analogue, nickel nitride, has shown a promising electrochemical performance in Li-ion and Na-ion batteries,^{29, 30} thus, it is expected that nickel phosphide has great potential to be a good candidate in battery applications.

Nickel phosphide has been synthesized from several different routes. NiP₂ was obtained from high temperature synthesis of nickel metal and red phosphorous³¹ or from high pressure synthesis³² or room temperature ball milling.³³ Ni₂P and Ni₁₂P₅ nanoparticles was prepared from solution phase synthesis with capping agents, but this route involved high temperature decomposition of a phosphine which may generate highly corrosive and flammable phosphorous.³⁴ Also, Ni₁₂P₅ was obtained from hydrothermal synthesis at low temperature (180 °C) with relatively safe conditions.³⁵

Nickel phosphide has been exhibited promising electrochemical performance in dye-sensitized solar cell³⁵, electrocatalysts for hydrogen evolution³⁶ and in lithium secondary batteries.^{18, 37, 38} In lithium ion batteries, NiP₂ can deliver over 1000 mA h g⁻¹ capacity in the first cycle and reversibly reacted with 5 Li per unit formula at low current rate (C/20), but only 10 cycles were shown in its galvanostatic test.¹⁸ Thin film Ni₃P prepared from electrodeposition exhibited a similar performance but the capacity decayed rapidly to 100 mA h g⁻¹ after 10 cycles.³⁸ Ni₃P-Ni film showed a large irreversible capacity in the first cycle and the cycling stability was reasonably good which remained 340 mA h g⁻¹ capacity over 40 cycles.³⁷

In this work, nickel phosphide (Ni_{12}P_5) was obtained from hydrothermal synthesis and its electrochemical performance as the negative electrode material was investigated in Li-ion and Na-ion batteries.

6.6.1 Synthesis and characterization of nickel phosphide

Synthesis of Ni_{12}P_5 was followed a hydrothermal route proposed by Dou *et al*³⁵. Red phosphorus (Aldrich, 390 mg, 0.0126 mol) was added into a stirred solution of nickel chloride hexahydrate (Aldrich, 892.5 mg, 0.00375 mol) in a mixture of ethylene glycol and water (50 ml, ratio 9:16). The brick red cloudy reaction mixture was stirred for 30 minutes, ultra sonicated for 30 minutes and the stirred for 1 hour after it was sealed in a Teflon-lined steel autoclave for hydrothermal treatment at 180 °C for 12 hrs. The dark grey Ni_{12}P_5 was collected by centrifugation (3500 rpm, 10 min), washed with distilled water and ethanol and finally dried in the oven at around 80 °C for overnight.

The fitted XRD pattern is shown in Figure 6.26. The refined lattice parameters of Ni_{12}P_5 are $a=8.6546(7)$ and $c=5.0779(4)$ Å, cell volume is 380.35(5), which are close the reported value, $a=8.646$ and $c=5.07$ Å.³⁹ A minor Ni_2P impurity was found in the product. Crystallite size of Ni_{12}P_5 was determined to be around 25.2(1) nm from the Lorentzian components of the profile fit.¹⁵

The SEM images (Figure 6.27) show a heavy aggregation of the particles at low magnification. The large cluster of crystallites (around 0.5 μm) can be observed at high magnification. The heavy aggregation could result in a low accessible surface area.

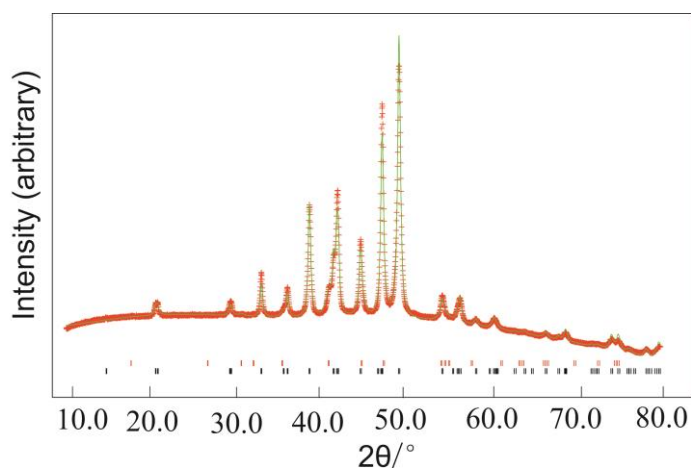


Figure 6.26 Rietveld fit ($R_{wp} = 2.3\%$, $R_p = 1.6\%$) to the PXD data for $Ni_{12}P_5$ produced from hydrothermal synthesis at $180\text{ }^\circ\text{C}$. Crosses mark the data points, the upper continuous line the fit and the lower continuous line the difference. Tick marks show the allowed positions of reflections for $Ni_{12}P_5$ with space group $I\ 4/M$ and the upper tick marks those of Ni_2P .¹⁶

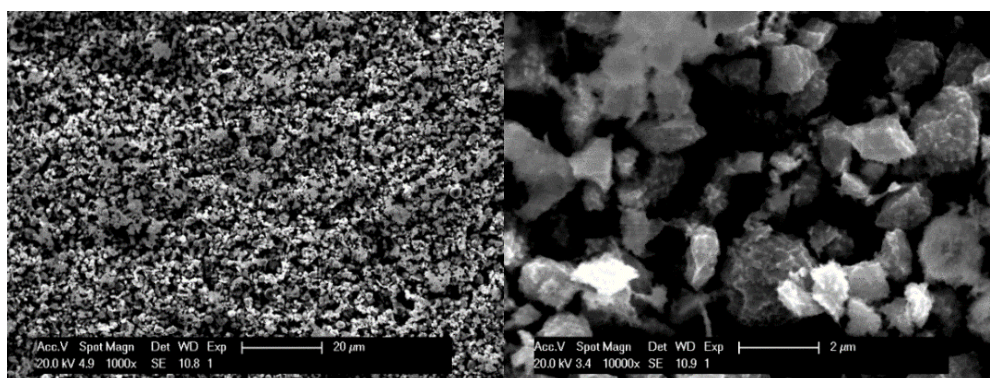


Figure 6.27 SEM images of $Ni_{12}P_5$ obtained from hydrothermal synthesis. The scale bar is $20\ \mu\text{m}$ on the left and $2\ \mu\text{m}$ on the right.

6.6.2 Nickel phosphide as the negative electrode material for Li-ion batteries

The working electrode consisted of a powdered mixture of 75% active material with 20% of acetylene black (Shawinigan, Chevron Phillips Chemical Co. LP) and 5% PTFE rolled into a $90\ \mu\text{m}$ thick sheet and then cut into a 10 mm diameter pellet. working electrodes

were also made of a powder mixture of 75% active material with 20% of acetylene black and 5% PVdF binder dissolving into cyclopentanone to form the ink, then dropping the ink onto 50 μm copper foil as disk electrode.

The cyclic voltammetry test was conducted at 2 mV s^{-1} for 20 cycles in the lithium half-cell. It can be seen in Figure 6.28 that large multiple reduction peaks were found between 0.5 V to 2 V in the first negative scan and one broad peak observed at around 1.3 V in the corresponding anodic scan, suggesting a large irreversible capacity in the first cycle. This irreversible capacity could be attributed to the formation of the SEI layer. The broad oxidation peak was found at around 1.2 V in the initial cycles and reduced after 20 cycles, which indicated the capacity decay during the cycling.

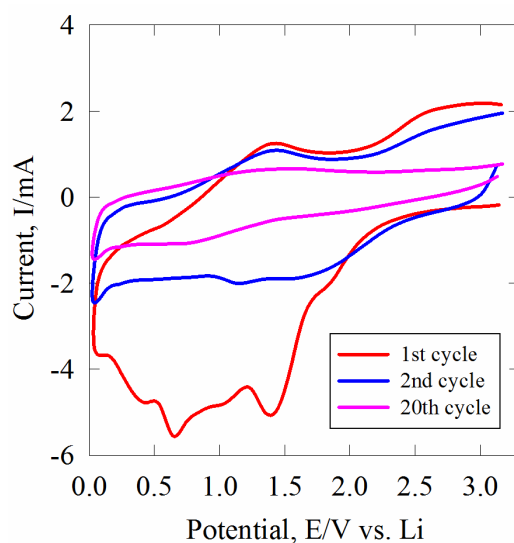
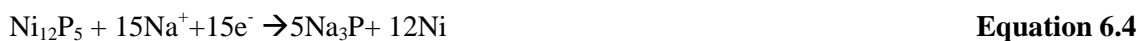


Figure 6.28 Cyclic voltammetry of Ni_{12}P_5 obtained at $180 \text{ }^\circ\text{C}$ from hydrothermal synthesis in the 1st, 2nd and 20th cycle at 2 mV s^{-1} for 20 cycles in lithium half cells. The counter electrode is lithium metal foil and the electrolyte is 1M LiPF_6 in EC:DMC (1:1).

The galvanostatic result of Ni_{12}P_5 pellet electrode is shown in Figure 6.29. Due to the large formula mass of Ni_{12}P_5 , the theoretical capacity (465 mA h g^{-1} calculated from Equation 6.4) was not as high as the suggested by the number of electrons transferred (15 electrons).



Pellet electrodes containing Ni_{12}P_5 showed the poor electrochemical performance of pellet Ni_{12}P_5 in lithium cells at 0.5 C. Less than 20 mA h g^{-1} capacity was obtained in the first cycle and this capacity quickly diminished to around 5 mA h g^{-1} in the subsequent cycles. This poor performance could be due to the large mass loading of the pellet electrode which cannot be fully used in the measurement, resulting in a real current that is far higher than 0.5 C. The high current may lead to a large internal resistance loss, thus the poor electrochemical performance can be explained.

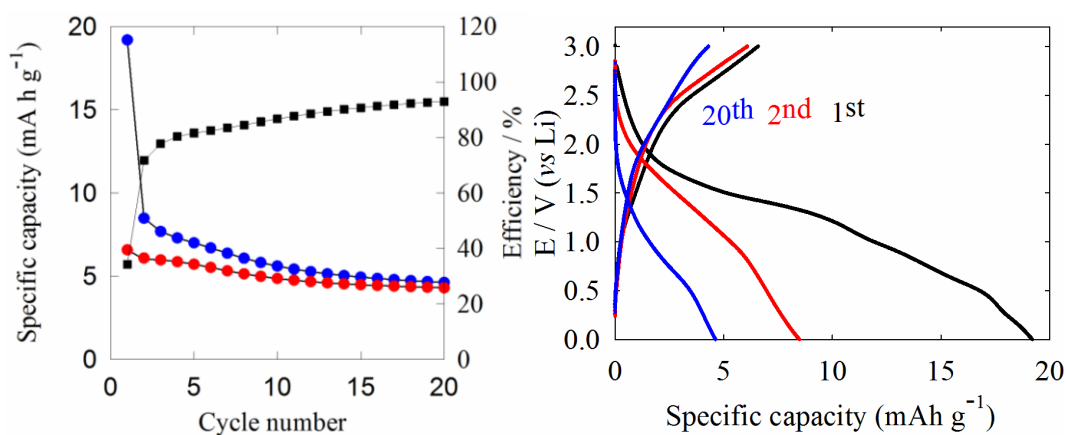


Figure 6.29 Voltage profile against specific cycles (right) and specific capacity versus cycle number profile (left) of Ni_{12}P_5 pellet electrodes in lithium half cells cycled between 1 mV and 3 V for 20 cycles at 0.5 C (237 mA h g^{-1}). In the specific capacity vs cycle number plots blue circles show specific reduction capacity, red circles show specific oxidation capacity and black ones depict Coulombic efficiency.

The galvanostatic result of a Ni_{12}P_5 inked disk electrode is shown in Figure 6.30. With less mass loading of the electrode, it can be seen that the galvanostatic performance has been improved. Around 160 mA h g^{-1} capacity was achieved in the first cycle and as with the pellet electrode, the capacity rapidly reduced to 50 mA h g^{-1} in the second cycle. The different performance between pellet electrode and disk electrode suggests that a small portion of the active electrode material was used to store the charge which could be the surface layer of the electrode. Though the bulk Ni_{12}P_5 showed lower capacity than NiP_2 ¹⁸ or Ni_3P ³⁷, the potential to improve the electrochemical performance, e.g. reducing the particle size to enhance the kinetics in the cell, and the good cycle stability can make Ni_{12}P_5 competitive to other nickel phosphides in lithium cells.

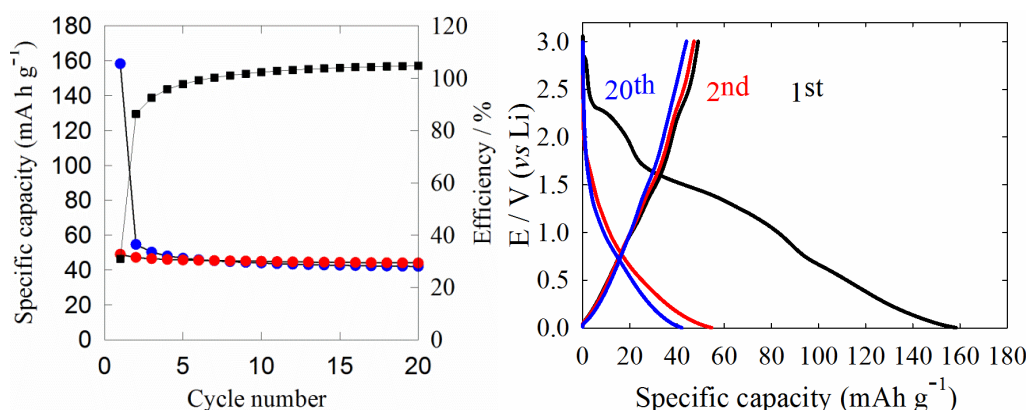


Figure 6.30 Voltage profile against specific cycles (right) and specific capacity versus cycle number profile (left) of Ni_{12}P_5 disk electrodes in lithium half cells cycled between 1 mV and 3 V for 20 cycles at 0.5 C (237 mA g^{-1}).

6.6.3 Nickel phosphide as the negative electrode material for Na-ion batteries

The cyclic voltammetry of Ni_{12}P_5 at 1 mV s^{-1} for 20 cycles in sodium half cells is shown in Figure 6.31. As with that in lithium cells, large irreversible charge due to the peaks at around 0.9 V and 0.4 V were observed in the first reduction cycle, which could be

attributed to the formation of the SEI layer. The voltage hysteresis (approximately 0.6 V) was observed at around 0.8 V in the second reduction cycle and 1.4 V in the corresponding oxidation process. The voltage polarization increased during cycling, which could be due to the increase of the internal resistance.

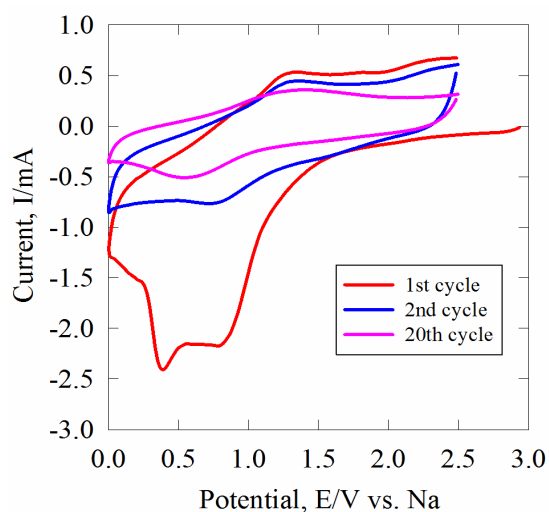


Figure 6.31 Cyclic voltammetry of Ni₁₂P₅ obtained at 180 °C from hydrothermal synthesis in the 1st, 2nd and 20th cycle at 1 mV s⁻¹ for 20 cycles in lithium half cells. The counter electrode is sodium metal foil and the electrolyte is 1M NaPF₆ in EC:DEC (1:1).

The galvanostatic performance of Ni₁₂P₅ pellet electrode in sodium half cells is shown in Figure 6.32. As with lithium, the performance in sodium cells was poor. Only around 20 mA h g⁻¹ capacity was obtained in the first cycle, and rapidly decayed in the 20 cycles. This could be due to the large internal resistance loss resulted from large current used and the electrochemical process occurred at the electrode surface.

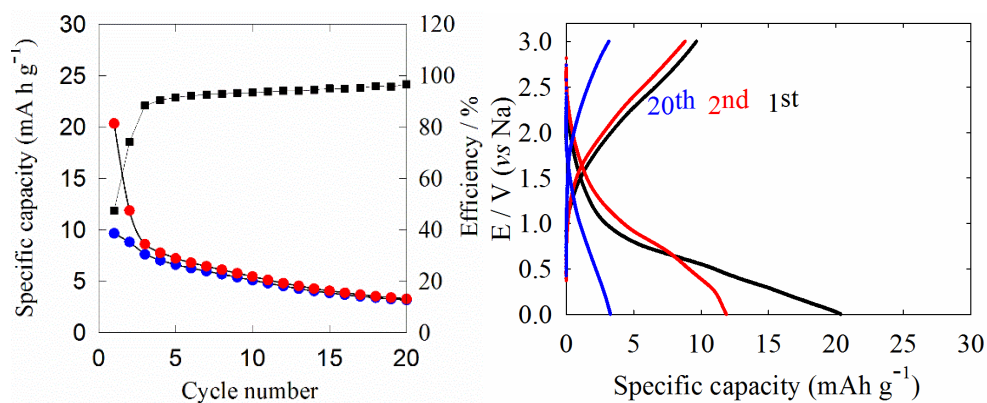


Figure 6.32 Voltage profile against specific cycles (right) and specific capacity (left) versus cycle number profile of Ni_{12}P_5 pellet electrodes in sodium half cells cycled between 1 mV and 3 V for 20 cycles at 0.5 C (237 mA g^{-1}).

The galvanostatic testing of Ni_{12}P_5 inked disk electrode is presented in Figure 6.33.

Comparing to the pellet electrode, the electrochemical performance in specific capacity and cycle stability was enhanced using disk electrodes, which was also observed in lithium cells. 57 mA h g^{-1} capacity was obtained in the first cycle and 23 mA h g^{-1} capacity (40%) was retrieved in the oxidation cycle. Around 20 mA h g^{-1} capacity was remained after 20 cycles, 85% capacity retention. It can be found in its voltage profile that a reduction slop at around 0.9 V in the first cycle and a short oxidation voltage plateau at 1.7 V. Around 0.8 V voltage polarization was observed and it increased during the cycling, which could be due to the increase of the internal resistance with the formation SEI layer. Though the capacity was not as high as other nitride materials, it was expected a better performance with lower current rate (less internal resistance loss) and smaller particle size (shorter electron pathway).

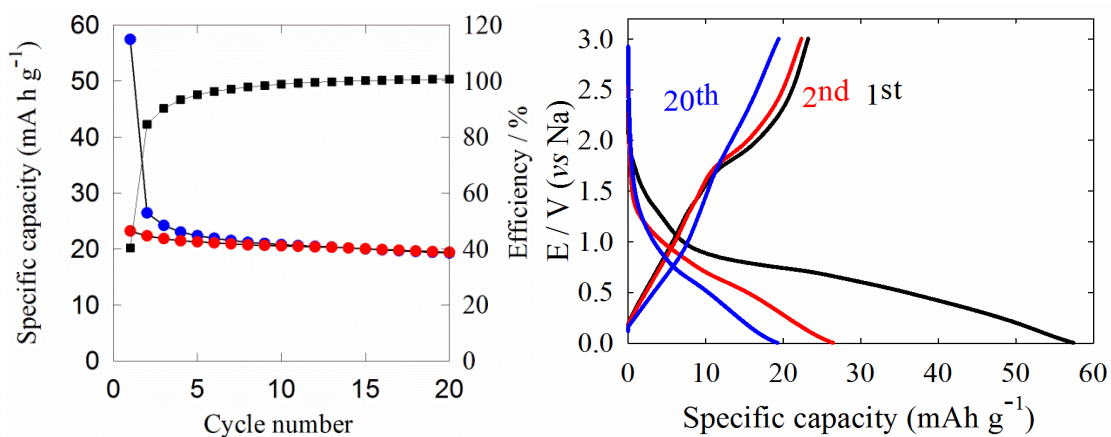


Figure 6.33 Voltage profile against specific cycles (right) and specific capacity (left) versus cycle number profile of Ni_{12}P_5 disk electrodes in sodium half cells cycled between 1 mV and 3 V for 20 cycles at 0.5 C (237 mA g^{-1}).

6.7 Capacity due to the acetylene black conductivity additive

As acetylene black was added to improve the conductivity for each sample and it has shown around 100 mA h g^{-1} reversible capacity at a very low current rate without extended cycling in sodium cells,⁴⁰ the electrochemical performance of acetylene black was also investigated to verify whether the acetylene black contribute a lot to the observed capacity in the electrochemical performances conducted in this work.

The working electrode was made of the acetylene black (90%) was mixed with 10% PVdF binder,⁴⁰ dissolving into cyclopentanone to form the ink, then dropping onto $50 \mu\text{m}$ thick and 10 mm in diameter copper foil disk.

The voltammogram of acetylene black (Figure 6.34) showed a sharp reduction peak near to 0 V in the first cycle and a minor oxidation peak at around 0.7 V were observed. The cycling performance after first cycle was stable as the curves overlapped with each other.

The charge was stored mainly due to the processes correspond to the reduction peak near to 0.2 V and oxidation peak at around 0.4 V.

Galvanostatic testing of acetylene black (Figure 6.35, left) showed a stable cycling performance with around 85 mA h g^{-1} reversible capacity over 50 cycles. In this work, 20% acetylene black was added to increase conductivity and therefore purely calculated from the acetylene black capacity in the sodium half-cell, around 17 mA h g^{-1} might come from acetylene black. As a consequence, there would be minor capacities attributed from nitride materials, e.g. chromium nitride, vanadium nitride, in sodium-ion batteries. However, the good electrochemical performance of acetylene black in this case could be partly due to the stack of acetylene black (90% composition), like hard carbon in sodium cells.⁴¹ This would be maximised in a cell made from just acetylene black, and the structures would be disrupted by the majority phase in a composite electrode formulation.

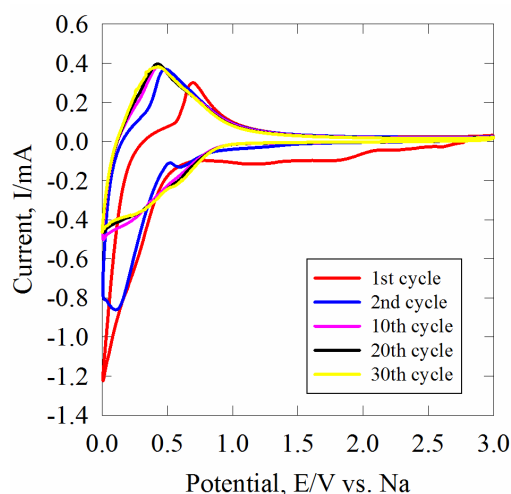


Figure 6.34 Cyclic voltammetry of acetylene black electrode in the 1st, 2nd, 10th, 20th and 30th cycle. Scan rate is 1 mV s^{-1} . The counter electrode and reference electrode is sodium metal foil and the electrolyte is 1 M NaPF_6 in EC:DEC (1:1).

The real specific capacity contribution of acetylene black was estimated by comparing the performance of stacked acetylene black with Ni_{12}P_5 case which showed a poor performance with 20% acetylene black (Figure 6.35, right). In the 20th cycle, the specific capacity of Ni_{12}P_5 was 19 mA h g^{-1} and the stack acetylene black had around 17 mA h g^{-1} (converted from the weight percent multiplied by the specific capacity of stacked acetylene black, $20\% \times 85 \text{ mA h g}^{-1}$). In the voltage profile graph of acetylene black and Ni_{12}P_5 , it can be seen that most of the capacity from acetylene black was in the region below 0.8 V in the oxidation cycle, while the region of Ni_{12}P_5 /acetylene black was mostly above 0.8 V. The ratio of the gradients of the Ni_{12}P_5 /acetylene black cell: the pure acetylene black cell was 0.46 in the oxidation curves and 0.80 in the reduction curve. Hence we can conclude that the maximum contribution of the acetylene black to the observed capacity of the Ni_{12}P_5 cells is 0.46 multiplied by the 17 mA h g^{-1} obtained with pure acetylene black as described in the previous paragraph, i.e. around 8 mA h g^{-1} . However, this is also likely to be an overestimate as the acetylene black oxidation curve has a much higher gradient above 0.8 V and this is not reflected in the oxidation curve of the Ni_{12}P_5 /acetylene black composite. Thus, it can be extrapolated that in real measurements of this work, acetylene black might contribute to some capacities, but not dominated. The main role of acetylene black is to increase the conductivity, facilitating with formation of the stable SEI layer.

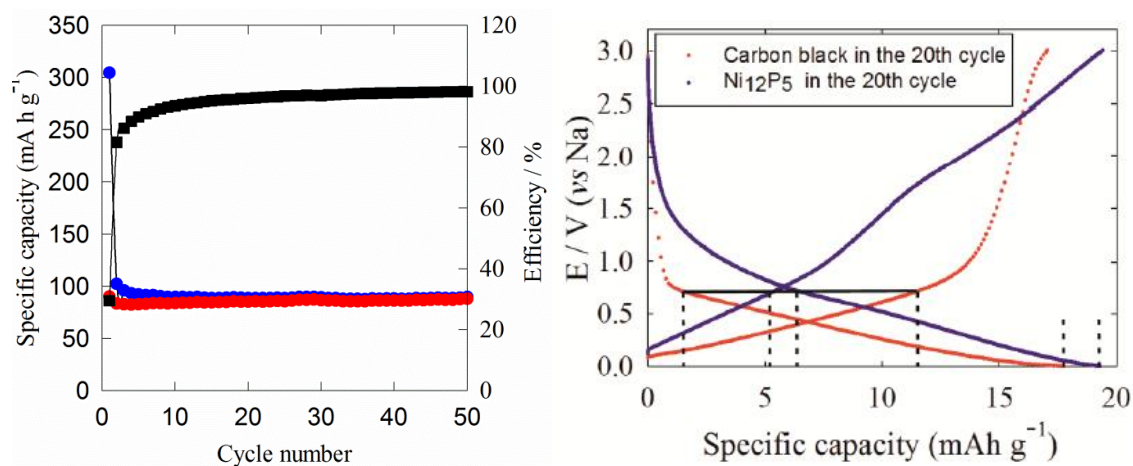


Figure 6.35 Specific capacity versus cycle number of acetylene black at 200 mA g⁻¹ (left) and voltage profile (right) of Ni₁₂P₅ at 0.5 C (237 mA g⁻¹) in the 20th cycle (blue) and acetylene black at 200 mA g⁻¹ in the 20th cycle (red) in sodium-half cells. The capacity of the acetylene black has been divided by 5 to obtain a profile equivalent to 20% carbon in the cell and hence match that in the composite electrode. The black lines are drawn as a guide to the eye to show the regions over which the gradient calculations were performed.

6.8 Conclusions

In this chapter, chromium nitride was synthesized from ammonolysis of chromium urea precursor and characterized by XRD, TEM, and IR, etc. Its electrochemical performance as the negative electrode material in Li-ion and Na-ion batteries was investigated. Although it has a large theoretical capacity (over 1200 mA h g⁻¹ based on the conversion reaction due to the large nitrogen content in its formula), most of the capacity can hardly be retrieved in real. The poor performance of chromium nitride in this case could be attributed to the as formed SEI layer could not perform very well in the charge storage.

Screening of the electrochemical performance of other nitrides, e.g. vanadium nitride, molybdenum nitride, manganese nitride, and zinc nickel nitride in battery applications, was also conducted. Vanadium nitride and zinc nickel nitride exhibited a poor electrochemical performance in Na-ion cells, which could be similar to chromium nitride that the as formed SEI layer is not good for charge storage in sodium-ion batteries. Manganese nitride shows good electrochemical performance in lithium-ion and sodium-ion cells. In lithium cells, it exhibited a 600 mA h g^{-1} reversible capacity at 200 mA g^{-1} and remained 340 mA h g^{-1} capacity in the 50th cycle, which is competitive to the thin film manganese nitride performance in lithium-ion batteries.²³ In sodium cells, manganese nitride showed a high specific capacity of 127 mA h g^{-1} at 50 mA g^{-1} over 50 cycles, which is comparable to other transition metal nitrides, e.g. nickel nitride and copper nitride. Molybdenum nitride showed a reasonably good performance in Na-ion cells with a 213 mA h g^{-1} reversible capacity at 100 mA g^{-1} . But the decay in capacity can be found during 50 cycles to around 100 mA g^{-1} .

The electrochemical performance of several metal nitrides in Na-ion batteries has been investigated. Most of the nitrides exhibited much lower capacity than their theoretical capacity, which indicates the main charge storage mechanism of nitride materials could be focused on the surface SEI layer. Hence, small particle size might be beneficial to the charge storage at electrode surface. As the main charge storage mechanism of nitride materials occurred at the surface of electrode, electrolyte optimization could improve their electrochemical performance in Na-ion cells. Additionally, other metal nitride materials, in terms of which has large nitrogen content and the metal can alloy with sodium, can be potential candidates for Na-ion batteries in the future.

Nickel phosphide (Ni_{12}P_5) was also investigated in this work with my project student, Deborah Benjamin. Nickel phosphide was obtained from hydrothermal synthesis at 180 °C. Its electrochemical performance in lithium and sodium cells was investigated. Although the result is not as good as expected, it showed a potential of phosphides as the negative electrode material for sodium-ion batteries. This could be a future direction worthy to attempt.

6.9 Reference

1. R. Riedel, *Handbook of Ceramic Hard Material, Ed.*, Wiley, 2000.
2. L. M. Corliss, N. Elliott and J. M. Hastings, *Phys. Rev.*, 1960, 117, 929.
3. J. Vetter, *Surf. Coat. Technol.*, 2005, 76, 719.
4. L. Swadzba, A. Maciejny, B. formanek, P. Liberski, P. Podolski, B. Mendala, H. Gabriel and A. Poznanska, *Surf. Coat. Technol.*, 1996, 78, 137.
5. P. Panjan, B. Navinsek, A. Cvelbar, A. Zalar and I. Milosev, *Thin Solid Films*, 1996, 282, 298.
6. U. Kopacz and R. Riedl, *Z. Metallkd.*, 1992, 83, 492.
7. Y. Claesson, M. Georgson, A. Roos and C.-G. Ribbing, *Solid Energy Mater.*, 1990, 20, 455.
8. Z. Zhang, R. Liu and Y. Qian, *Mater.Res.Bull.*, 2002, 37, 1005.
9. X. F. Qian, X. M. Zhang, C. Wang, K. B. Tang, Y. Xie and Y. T. Qian, *Mater. Res. Bull.*, 1999, 34, 433.
10. D. V. Baxter, M. H. Chisholm, G. J. Gama, V. F. DiStasi, A. L. Hector and I. P. Parkin, *Chem. Mater.*, 1996, 8, 1222.
11. B. Das, M. V. Reddy, G. V. Subba Rao and B. V. R. Chowdari, *RSC Adv.*, 2012, 2, 9022.
12. Q. Sun and Z.-W. Fu, *Electrochim. Acta*, 2008, 54, 403.

13. Q. Sun and Z.-W. Fu, *Electrochem. Solid-State Lett.*, 2008, 11, A233.
14. Q. Sun and Z.-W. Fu, *Electrochem. Solid-State Lett.*, 2007, 10, A189.
15. H. M. Rietveld, *J. Appl. Cryst.*, 1969, 2, 65.
16. Inorganic Crystal Structure Database (ICSD, Fiz Karlsruhe) accessed via the National Chemical Database Service hosted by the Royal Society of Chemistry.
17. K. Nakamoto, ed., *Infrared and Raman Spectra of Inorganic and Organic Compounds 3rd ed*, J. Wiley: New York, 1978.
18. F. Gillot, S. Boyanov, L. Dupont, M. L. Doublet, M. Morcrette, L. Monconduit and J. M. Tarascon, *Chem. Mater.*, 2005, 17, 6327.
19. K. Zhang, H. Wang, X. He, Z. Liu, L. Wang, L. Gu, H. Xu, P. Han, S. Dong, C. Zhang, J. Yao, G. Cui and L. Chen, *J. Mater. Chem.*, 2011, 21, 11916.
20. D. Choi and P. N. Kumta, *Electrochem. Solid-State Lett.*, 2005, 8, A418.
21. D. Choi, G. E. Blomgren and P. N. Kumta, *Adv. Mater.*, 2006, 18, 1178.
22. X. Lu, M. Yu, T. Zhai, G. Wang, S. Xie, T. Liu, C. Liang, Y. Tong and Y. Li, *Nano Lett.*, 2013, 13, 2628.
23. T. Tsumura, T. Kiyono, M. Toyoda and O. Tanaike, *ECS Trans.*, 2009, 16, 167.
24. D. K. Nandi, U. K. Sen, D. Choudhury, S. Mitra and S. K. Sarkar, *ACS Appl. Mater. Interf.*, 2014, 6, 6606.
25. S. I. U. Shah, A. L. Hector and J. R. Owen, *J. Power Sources*, 2014, 266, 456.
26. D. Xia, S. Liu, Z. Wang, G. Chen, L. Zhang, L. Zhang, S. Hui and J. Zhang, *J. Power Sources*, 2008, 177, 296.
27. G. R. Li, J. Song, G. L. Pan and X. P. Gao, *Energ. Environ. Sci.*, 2011, 4, 1680.
28. Q. Sun and Z.-W. Fu, *Appl. Surface Sci.*, 2012, 258, 3197.
29. X. Li, M. M. Hasan, A. L. Hector and J. R. Owen, *J. Mater. Chem. A*, 2013, 1, 6441.
30. F. Gillot, J. Oro-Sole and M. R. Palacin, *J. Mater. Chem.*, 2011, 21, 9997.
31. S. Rundqvist, *Acta Chem. Scand.*, 1961, 15, 451.

32. P. C. Donohue, T. A. Bither and H. S. Young, *Inorg. Chem.*, 1968, 7.
33. L. Takacs and S. K. Mandal, *Mater. Sci. Eng.*, 2001, 429, A304.
34. E. Muthuswamy, G. H. L. Savithra and S. L. Brock, *ACS Nano*, 2011, 5, 2402.
35. Y. Y. Dou, G. R. Li, J. Song and X. P. Gao, *Phys. Chem. Chem. Phys.*, 2012, 14, 1339.
36. E. J. Popczun, J. R. McKone, C. G. Read, A. J. Biacchi, A. M. Wiltrout, N. S. Lewis and R. E. Schaak, *J. Am. Chem. Soc.*, 2013, 135, 9267.
37. J. Y. Xiang, J. P. Tu, X. L. Wang, X. H. Huang, Y. F. Yuan, X. H. Xia and Z. Y. Zeng, *J. Power Sources*, 2008, 185, 519.
38. M. Cruz, J. Morales, L. Sánchez, J. Santos-Peña and F. Martín, *J. Power Sources*, 2007, 171, 870.
39. Q. Guan, X. Cheng, R. Li and W. Li, *J. Catal.*, 2013, 299, 1.
40. R. Alcántara, J. M. Jiménez-Mateos, P. Lavela and J. L. Tirado, *Electrochem. Commun.*, 2001, 3, 639.
41. D. A. Stevens and J. R. Dahn, *J. Electrochem. Soc.*, 2000, 147, 1271.

Chapter 7. Conclusions and future work

7.1 Conclusions

Suitability of metal nitrides, e.g. Ni_3N , Cu_3N , or Sn_3N_4 as negative electrode materials in sodium-ion batteries has been investigated in this project.

Specifically, nickel nitride was synthesized from two routes. One was the ammonolysis of nickel hexamine nitrate at 335 °C for 6 h followed by 200 °C for 8 h, the other was from heating nickel *tris*(ethylenediamine) nitrate at 360 °C for 4 h then 200 °C for 40 h under flowing ammonia. Their electrochemical performances in lithium- and sodium-ion half cells were compared. $[\text{Ni}(\text{EDA})_3](\text{NO}_3)_2$ -derived Ni_3N showed a high specific capacity and better cycle stability against the one derived from $[\text{Ni}(\text{NH}_3)_6](\text{NO}_3)_2$ in Li-ion and Na-ion half cells, which could be attributed to the small particle size obtained from the *tris*(ethylenediamine) route. In lithium-ion half-cells, $[\text{Ni}(\text{EDA})_3](\text{NO}_3)_2$ -derived Ni_3N exhibited a similar performance to amide-derived Ni_3N published by Gillot *et al.*¹ It delivered a high specific reduction capacity (more than 1200 mA h g⁻¹), which is around 3 times more than its theoretical specific capacity (423 mA h g⁻¹) in the first reduction cycle and then capacity rapidly decayed in the subsequent cycles. In sodium-ion half-cells, Ni_3N was firstly studied as the negative electrode material and it exhibited a capacity of around 460 mA h g⁻¹ at 0.5 C in the first reduction cycle and a reversible capacity of 134 mA h g⁻¹ after 20 cycles, which was competitive to the most carbon based materials by then²⁻⁴. It exceeded capacity of “Templated carbon”³ and $\text{NaTi}_2(\text{PO}_4)_3$ ⁴ which were both reported in 2011 and delivered ~120 mA h g⁻¹ over 20 cycles with a similar potential range. Better cycle stability against the carbon black which only showed limited number

of cycles with capacity decay at a low current rate ($C/75$, the current required to insert sodium into carbon electrode to form NaC_6 in 75 hours).²

Cu_3N was prepared by ammonolysis of anhydrous copper fluoride and copper(II) pivalate precursor at 300 °C and 250 °C, respectively. The samples were characterized by several measurements, e.g. PXD, TEM, and IR. Cu_3N derived from pivalate route showed a larger surface area and smaller particle size than that obtained from the copper fluoride route. Better electrochemical performance was achieved by using Cu_3N derived from copper pivalate route in sodium half cells. After an initial conditioning period the capacity was reversible and was stable over 50 cycles at rates between 1 C, 0.5 C and 0.1 C, with 89 mA h g⁻¹ observed in the 50th cycle at 0.1 C, which exhibited a better cycling stability than that of Ni_3N in sodium-ion half-cells. *Ex situ* XRD showed the formation of metallic copper in the first cycle but the reflections of metallic copper did not vanish after re-oxidizing to 3 V, which indicates the conversion reaction from Cu_3N to Cu is not a completely reversible process. Cu_3N was retained throughout and hence the reactions appear to take place mainly at the surface of the electrode.

Furthermore, Cu_3N derived from copper pivalate route offered competitive electrochemical performance in lithium-ion cells to that reported previously by Pereira *et al.*⁵ A large capacity of 1811 mA h g⁻¹ was passed in the first cycle and around 60% of which was recovered. The capacity decayed in the following cycles with 287 mA h g⁻¹ in the 50th cycle at 0.5 C, which is slightly different to the cycling performance of Cu_3N studied by Pereira *et al.*⁵ In their work, stable reduction capacities of 140-170 mA h g⁻¹ at 1.67 C with a capacity loss in the initial cycles were observed. And an unusual gradual increase in capacity when oxidized beyond 2 V vs Li, which the authors attributed to

oxide formation linked to the electrolyte degradation.

Exposure to water resulted in hydrolysis and the formation of CuO, which offered larger initial capacities in sodium cells but was less stable during cycling, with 138 mA h g⁻¹ in the 30th cycle at 0.29 C. *Ex situ* XRD revealed that CuO was reduced to Cu₂O and then to Cu metal in the first cycle, with partial re-oxidation to Cu₂O and copper metal on oxidizing back to 3 V, which is consistent with the work published by Klein *et al.*⁶

Combining conversion reaction with alloying/de-alloying mechanism could offer a high specific capacity in sodium-ion batteries, e.g. Sb₂S₃: 946 mA h g⁻¹,⁷ or Sn₄P₃: 1132 mA h g⁻¹,^{8,9}. Tin nitride (Sn₃N₄) can provide similar charge storage mechanism which tin nitride was firstly reduced to tin metal via conversion reaction and then sodium alloyed/de-alloyed with tin metal to store the charge. Bulk tin nitride was synthesized from ammonolysis of polymeric amide-derived precursor which derived from the reaction of Sn(NEt₂)₄ with ammonia. After washing with 3M HCl, pure phase Sn₃N₄ was obtained. Samples obtained at 350 °C were observed to exhibit small particle size with the highest specific surface area among all samples.

As tin nitride is stable in deionized water, two water based binders were selected for the electrochemical tests in sodium-ion cells. In both cases, the cycling stability is good. In contrast with the cells using CMC binder, alginate binder employed cells showed higher specific capacity and similar cycling stability from the direct comparison of their cycling performances (Figure 5.8). The cell with alginate binder had a capacity of 175 mA h g⁻¹ in the 2nd cycle and 155 mA h g⁻¹ in the 50th cycle (89% capacity retention) at 200 mA g⁻¹ while the one with CMC binder showed a capacity of 144 mA h g⁻¹ in the 2nd cycle and 113 mA h g⁻¹ in the 50th cycle (79% capacity retention) at the same current rate. The effect

of FEC additives was also investigated in this work. With the help of FEC additives, Sn_3N_4 cells with alginate binder showed a capacity of 680 mA h g^{-1} in the first cycle at 50 mA g^{-1} in the sodium-ion cells with the FEC additive and approximately 47% of which (320 mA h g^{-1}) was retained in the second cycle and the stable cycle performance around 85% capacity (compared with the second cycle) retention over 50 cycles. A significant capacity rise ($\sim 35\%$) against the cell without FEC additives was observed. The electrochemical behaviour of Sn_3N_4 is the best electrochemical performance of transition metal nitrides as negative electrode materials in Na-ion cells and it can be comparable with other negative electrode materials in sodium cells, e.g. hard carbon¹⁰, which showed $\sim 220 \text{ mA h g}^{-1}$ reversible capacity over 100 cycles. In the *ex situ* XRD measurement, the main reflections during the first reduction/oxidation cycle are still tin nitride pattern. The amorphous background and the weakened intensity suggest the surface reaction occurred in the cells. Hence, the performance can be further improved by reducing the particle size thereby increasing the active electrochemical surface area or increasing the conductivity with carbon coatings to reduce the internal resistance.

Furthermore, bulk tin nitride was firstly investigated as negative electrode materials in Li-ion batteries. Comparing to the electrochemical performance of tin nitride thin films¹¹,¹², bulk samples showed a similar voltage profile and higher capacity in the first cycles (1600 mA h g^{-1} reversible capacity at 100 mA g^{-1}). However, the capacity decayed rapidly in the subsequent cycles. The *ex situ* XRD measurements revealed that Sn_3N_4 was firstly reduced to amorphous Sn via the conversion reaction and the reduced Sn was alloyed with sodium to store the charge. During the oxidation cycle, crystalline Sn was formed without Sn_3N_4 detected in the sample, which indicates that the conversion reaction of

Sn_3N_4 to Sn is not a completely reversible process and the main charge storage mechanism of Sn_3N_4 in lithium-ion batteries is alloying/de-alloying process. The large volume change due to the sodium alloyed/de-alloyed with tin resulted in the poor cycling stability. Herein, with the FEC additive help, the stability was largely improved and remained 370 mA h g^{-1} capacity over 50 cycles at 200 mA h g^{-1} .

Screening the electrochemistry of other transition metal nitrides, e.g. chromium nitride, molybdenum nitride, or manganese nitride in battery applications was conducted. It is noted that molybdenum nitride and manganese nitride showed decent specific capacity and cycle stability in sodium cells. Manganese nitride showed a high specific capacity of 127 mA h g^{-1} at 50 mA g^{-1} over 50 cycles, which is comparable to other transition metal nitrides, e.g. nickel nitride and copper nitride. In lithium half-cells, it exhibited a 600 mA h g^{-1} reversible capacity at 200 mA g^{-1} and retained 340 mA h g^{-1} capacity in the 50th cycle, which is competitive to the manganese nitride thin film performance in lithium-ion batteries.¹³ Molybdenum nitride showed a reasonably good performance in Na-ion cells with a 213 mA h g^{-1} reversible capacity at 100 mA g^{-1} , a decay in its capacity can be found during 50 cycles to around 100 mA h g^{-1} . However, most of the nitrides exhibited much lower capacity than their theoretical capacity, which indicates the main charge storage mechanism of nitride materials could be focused on the surface SEI layer.

The nickel nitride analogue, nickel phosphide (Ni_{12}P_5) was obtained from hydrothermal synthesis at $180 \text{ }^\circ\text{C}$. Its preliminary electrochemical performance in lithium and sodium half-cells was investigated. Similarly to nitride materials, nickel phosphide showed a charge storage mechanism at the electrode surface. Its electrochemical performance was not as good as expected.

In all, electrochemical performance of several transition metal nitrides have been evaluated by galvanostatic and cyclic voltammetry tests. Their charge storage mechanisms were studied by *ex situ* XRD. The results exhibited promising electrochemical performance of these nitrides as negative electrode materials in sodium-ion batteries. With further optimization, e.g. reducing the particle size or improving the SEI layer, a better electrochemical performance might be achievable.

7.2 Future work

In this work, the electrochemical performance of metal nitrides in Na-ion cells indicated that the main charge storage mechanism could be at the surface interphase layer, as there is no distinct reflections change of nitrides observed in the *ex situ* XRD measurements. Hence, smaller particle would be beneficial to the larger capacity. Hence, binary or ternary nitrides with small particle sizes thereby high specific surface areas or special morphologies, e.g. nanowire or nanotube arrays, could largely improve the electrochemical performance as negative electrode materials in Na-ion cells.

Enhancement of binders or additives could stabilize the SEI layer, thereby enhancing the cycle stability and rate capability of transition metal nitrides in Na-ion cells. The electrolyte is another key parameter that could be further optimised for metal nitrides in sodium cells, as the decomposed electrolyte resulted in the formation of the SEI layer.

More electrochemical characterization focusing on the SEI layer, such as, electrochemical impedance spectroscopy, or *ex situ* TEM, can be beneficial to identify the charge storage mechanism at the surface interphase. Characterization of the surface layer

could also provide information on the charge storage mechanism of nitride materials, thereby providing further options to optimize their electrochemical performance.

From the material aspects, other metal nitrides, such as antimony nitride¹⁴, which has shown the mechanism combining conversion reaction and alloy process in lithium cells, can be the potential candidates in Na-ion cells in the future. In addition, the nitride analogues like phosphides could be also suitable for sodium-ion batteries.

7.3 Reference

1. F. Gillot, J. Oro-Sole and M. R. Palacin, *J. Mater. Chem.*, 2011, 21, 9997.
2. R. Alcántara, J. M. Jiménez-Mateos, P. Lavela and J. L. Tirado, *Electrochem. Commun.*, 2001, 3, 639.
3. S. Wenzel, T. Hara, J. Janek and P. Adelhelm, *Energy Environ. Sci.*, 2011, 4, 3342.
4. S. I. Park, I. Gocheva, S. Okada and J.-i. Yamaki, *J. Electrochem. Soc.*, 2011, 158, A1067.
5. N. Pereira, L. Dupont, J. M. Tarascon, L. C. Klein and G. G. Amatucci, *J. Electrochem. Soc.*, 2003, 150, A1273.
6. F. Klein, B. Jache, A. Bhide and P. Adelhelm, *Phys. Chem. Chem. Phys.*, 2013, 15, 15876.
7. D. Y. W. Yu, P. V. Prikhodchenko, C. W. Mason, S. K. Batabyal, J. Gun, S. Sladkevich, A. G. Medvedev and O. Lev, *Nat. Commun.*, 2013, 4, 2922.
8. Y. Kim, Y. Kim, A. Choi, S. Woo, D. Mok, N.-S. Choi, Y. S. Jung, J. H. Ryu, S. M. Oh and K. T. Lee, *Adv. Mater.*, 2014, 26, 4139.
9. J. Qian, Y. Xiong, Y. Cao, X. Ai and H. Yang, *Nano Lett.*, 2014, 14, 1865.
10. S. Komaba, W. Murata, T. Ishikawa, N. Yabuuchi, T. Ozeki, T. Nakayama, A. Ogata, K. Gotoh and K. Fujiwara, *Adv. Funct. Mater.*, 2011, 21, 3859.
11. K. S. Park, Y. J. Park, M. K. Kim, J. T. Son, H. G. Kim and S. J. Kim, *J. Power*

Sources, 2001, 103, 67.

12. L. Baggetto, N. A. M. Verhaegh, R. A. H. Niessen, F. Roozeboom, J.-C. Jumas and P. H. L. Notten, *J. Electrochem. Soc.*, 2010, 157, A340.
13. D. K. Nandi, U. K. Sen, D. Choudhury, S. Mitra and S. K. Sarkar, *ACS Appl. Mater. Interf.*, 2014, 6, 6606.
14. Q. Sun, W.-J. Li and Z.-W. Fu, *Solid State Sci.*, 2010, 12, 397.